

AD-A044 238 TEXAS A AND M UNIV COLLEGE STATION CENTER FOR TECTON--ETC F/6 8/7  
STUDY, EVALUATE, MEASURE, AND CALCULATE THE THERMAL CRACKING OF--ETC(U)  
MAY 77 J HANDIN, M FRIEDMAN, C B JOHNSON F19628-76-C-0122

UNCLASSIFIED

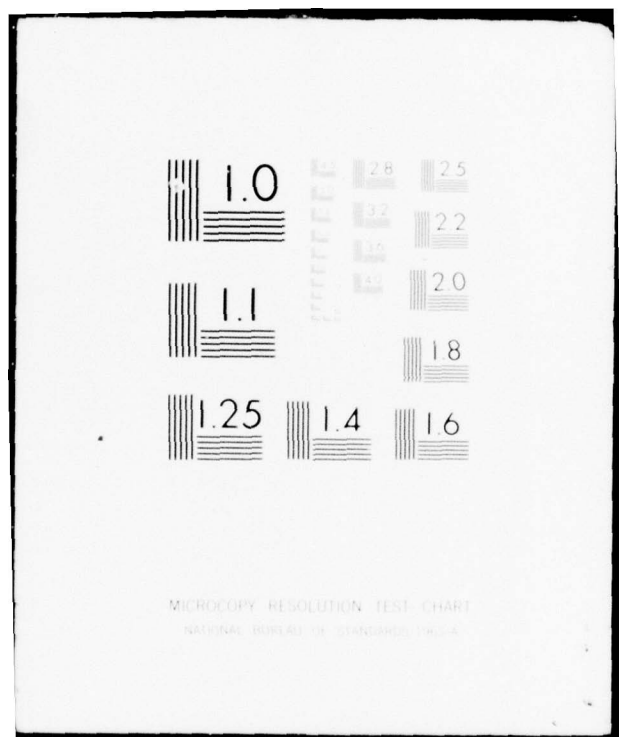
AFGL-TR-77-0122

NL

| OF |  
AD  
A044238



END  
DATE  
FILMED  
10-77  
DDC



AD A044238

AFGL-TR-77-0122

12

STUDY, EVALUATE, MEASURE, AND CALCULATE THE THERMAL CRACKING OF ROCKS

by

John Handin, Melvin Friedman, and C. Branning Johnson

Center for Tectonophysics  
Texas A&M University  
College Station, Texas 77843

FINAL REPORT

25 February 1976 - 15 March 1977

May 1977

Approved for public release, distribution unlimited

AD No.                     
DDC FILE COPY

AIR FORCE GEOPHYSICS LABORATORY  
AIR FORCE SYSTEMS COMMAND  
UNITED STATES AIR FORCE  
Hanscom AFB, Massachusetts 01731

D D C  
RECEIVED  
SEP 19 1977  
REF ID: B  
LST

**Qualified requestors may obtain additional copies from the Defense Documentation Center. All others should apply to the National Technical Information Service.**

Unclassified

SECURITY CLASSIFICATION OF THIS PAGE (When Data Entered)

REPORT DOCUMENTATION PAGE		READ INSTRUCTIONS BEFORE COMPLETING FORM
1. REPORT NUMBER 18 AFGL-TR-77-0122	2. GOVT ACCESSION NO.	3. RECIPIENT'S CATALOG NUMBER 9
4. TITLE (and Subtitle) Study, Evaluate, Measure, and Calculate the Thermal Cracking of Rocks.		
5. AUTHOR/MA John Handin, Melvin Friedman C. Branning Johnson	6. PERIOD OF REPORT & PERIOD COVERED Final Report, for Period 25 Feb 76 - 15 Mar 77	
7. AUTHOR/MA John Handin, Melvin Friedman C. Branning Johnson	8. CONTRACT OR GRANT NUMBER(S) F19628-76-C-0122	
9. PERFORMING ORGANIZATION NAME AND ADDRESS Center for Tectonophysics Texas A&M University College Station, TX 77843	10. PROGRAM ELEMENT, PROJECT, TASK AREA & WORK UNIT NUMBERS 61102F 76390502	
11. CONTROLLING OFFICE NAME AND ADDRESS Air Force Geophysics Laboratory Hanscom AFB, Mass 01731	12. REPORT DATE 11 May 1977	
13. MONITORING AGENCY NAME & ADDRESS (if different from Controlling Office)	14. NUMBER OF PAGES 12 80 p.	
15. SECURITY CLASS. (of this report) Unclassified		
16. DECLASSIFICATION/DOWNGRADING SCHEDULE		
17. DISTRIBUTION STATEMENT (of this Report) Approved for public release, distribution unlimited.		
18. SUPPLEMENTARY NOTES none		
19. KEY WORDS (Continue on reverse side if necessary and identify by block number) thermal cracking, thermal stress, slow thermal cycling, acoustic emission, irreversible velocity changes, Q changes, thermal expansion anisotropy, polymorphic transformation, quartz, quartzite, microstructure.		
20. ABSTRACT (Continue on reverse side if necessary and identify by block number) Changes of longitudinal-wave velocity ( $V_L$ ), porosity, and Q, together with optical and scanning electron microscopic observations, demonstrate unequivocally that appreciable thermal cracking occurs during slow thermal cycling of Sioux Quartzite. Thermally-induced cracks develop primarily along grain boundaries and secondarily as intragranular cracks. Intragranular cracks are		

DD FORM 1 JAN 73 1473 EDITION OF 1 NOV 55 IS OBSOLETE

Unclassified

SECURITY CLASSIFICATION OF THIS PAGE (When Data Entered)

404922

Done

ALPHA - BETA

Unclassified

SECURITY CLASSIFICATION OF THIS PAGE (When Data Entered)

preferentially oriented and appear to be influenced by the pre-heating residual strain state locked-in the rock.

Acoustic emission reveals that thermal cracking occurs only upon exceeding a threshold temperature, which for the Sioux Quartzite ranges between 200°C and 250°C. Thermal cracking increases progressively with increasing temperature, with the largest fraction of cracking occurring prior to the  $\alpha$ - $\beta$  transition of quartz (573°C). In the temperature interval 200-573°C,  $V_L$  decreases 40% and porosity increases 130%; new porosity is associated with low aspect-ratio cracks. Fracture intensifies during the  $\alpha$ - $\beta$  transition as reflected by an abrupt decrease in  $V_L$ , a rapid porosity increase and intense acoustic emission. Above 573°C, thermal cracking continues but at a reduced rate. Porosity continues to increase but is associated primarily with high aspect-ratio cracks. Cooling induces little additional structural damage.

Subtle microstructure differences measurably affect the threshold temperature of thermal cracking and the degree of thermal cracking occurring during a thermal cycle. Grain-size differences appear to be responsible.

Acoustic emission has proven to be a valuable source of information. Most significantly, acoustic emission activity is observed to be very similar amongst Sioux Quartzite samples subjected to the same thermal conditions. In general, upon exceeding the threshold temperature, emission increases progressively, attains a maximum (between 280°C and 400°C) and then decreases, commonly abruptly; a second larger maximum occurs between 570°C and 590°C, coincident with the  $\alpha$ - $\beta$  transition.

Thermal cracking of Sioux Quartzite is directly attributable to the marked thermal-expansion anisotropy of quartz, but also important is the temperature dependence of its elastic moduli, especially at and above the  $\alpha$ - $\beta$  transition. A first order calculation indicates that intergranular thermal stresses increase with increasing temperature, with an abrupt, large increase at the  $\alpha$ - $\beta$ .

$Q$  has not proven to be a sensitive indicator of microstructure changes, especially for room-dry samples in which the effect of small amounts of water overshadows that due to small microstructure changes.  $Q$  of a fully-saturated sample does, however, display a systematic decrease with increasing thermal cycle temperature and appears to be in accord with Biot's mechanism of attenuation in a fluid-saturated, porous elastic solid. Change of  $Q$  of room-dry, thermally-cycled samples is less systematic, but notably,  $Q$  increases for samples heated above 550°C.  $V_L$  is a sensitive indicator of microstructure changes, especially of new low aspect-ratio cracks; however, it is sensitive also to the degree of saturation of the sample.

SECURITY CLASSIFICATION OF THIS PAGE (When Data Entered)

## INTRODUCTION

Thermal cracking of rock results from the combined effects of temperature changes and temperature gradients. Temperature gradients give rise to thermal stresses because differing thermal expansions or contractions of the various parts of the rock body generally cannot proceed freely without creating incompatible strains within the rock. In a similar manner, a temperature change results in thermal stresses but as a consequence of the rock's inhomogeneity at the grain-size scale. In this case, highly inhomogeneous and discontinuous, intergranular stresses arise due to constraint of differing thermal expansions or contractions of neighboring mineral grains. The tendency for differing expansions and contractions results primarily from differences in the thermal expansion coefficients of adjacent mineral grains or anisotropy of the coefficients, but volume changes related to polymorphic transformations (e.g.,  $\alpha$ -quartz to  $\beta$ -quartz) or mineral alterations (e.g., dehydration and dissociation) also can make important contributions.

A number of experimental studies entailing the uniform heating of rock (Ide, 1937; Somerton and others, 1964; Barbish and Gardner, 1969; Perami, 1971; Wang and others, 1971; Todd and others, 1972; Richter and Simmons, 1974; Simmons and Cooper, in press) have demonstrated convincingly that intergranular thermal stresses can locally exceed the fracture strength of rock. These same studies further show that the resulting microcracks, which are usually of grain-size dimensions or smaller, irreversibly alter the physical properties of the rock; most notably, elastic moduli and fracture strength decrease and porosity and permeability

Section	<input checked="" type="checkbox"/>
Section	<input type="checkbox"/>
Section	<input type="checkbox"/>
BY	
DISTRIBUTION/AVAILABILITY CODES	
Dist.	AVAIL and/or SPECIAL
A	

increase. In addition, fracture toughness and thermal expansion and diffusivity coefficients appear to change. Consequently, when attempts are made to analyze the development of thermal cracking during non-uniform heating or cooling of rock, it is imperative that the effects of temperature-gradient thermal stresses and intergranular thermal stresses be incorporated. As implied by Hasselman (1969) the effects of the intergranular stresses and the resulting microcracks need not be small and may, in a number of ways, significantly affect the propagation of macrocracks induced by the temperature-gradient thermal stresses. Nevertheless, it is not surprising that such an incorporation is not often attempted. The analysis becomes more complicated, but probably more importantly our quantitative understanding of thermal crack generation during a uniform temperature change is still in its developmental stage.

It is our opinion that the first phase of a systematic study of the thermal cracking of rock should address the problem of microcrack formation in a uniform temperature field. Therefore, our investigation has concentrated on studying experimentally and observationally the development of microcracks in rock subjected to slow, uniform temperature changes and evaluating how the thermally-induced microcracks affect the physical properties of the rock. It should be emphasized that these first studies are essential if we are to distinguish the relative roles of absolute temperature and temperature gradients upon the thermal cracking of rock under conditions of non-uniform heating or cooling.

In our experiments, a cylindrical specimen of Sioux Quartzite is slowly heated ( $\leq 2^{\circ}\text{C}/\text{min}$ ) unconfined to a specified temperature between 20-900°C and then slowly cooled ( $\leq 2^{\circ}\text{C}/\text{min}$ ) to room temperature. During

the thermal cycle, acoustic emissions are monitored continuously as a means of providing a record of microcracking activity as a function of temperature. In order to obtain quantitative measures of microstructural changes induced in the rock, the longitudinal-wave velocity ( $V_L$ ) and the quality factor,  $Q$  (the inverse of wave attenuation), are measured prior to and after a thermal cycle. The longitudinal-wave velocity has been shown to be an especially sensitive indicator of microcracks (provided the rock is dry), and thus provides a means of detecting subtle microstructure changes (Thill and others, 1969; Nur and Simmons, 1969; Tourenq and others, 1971).  $Q$  has proved useful as an indicator of microstructure changes in other studies (Gordon and Davis, 1968; Kuszyk and Bradt, 1973; Coppola and Bradt, 1973), but our studies and others (Barbish and Gardner, 1969; Warren, 1973) indicate that  $Q$  is more sensitive to small changes in the water content of the sample than to small microstructure changes. Nevertheless  $Q$  does provide a measure of microstructure changes, but its sensitivity to changes is less than originally anticipated. Changes in  $V_L$  and  $Q$  provide indirect, but quantitative measures of microcrack development as a function of the maximum thermal-cycle temperature, which can then be compared to petrofabric observations and measurements made on thin and polished sections studied by optical and scanning electron microscopy. Ultimately the specimens will be tested to determine how compressive and tensile strengths, permeability and fracture energy vary with changes in the microstructure of the rock.

Several other aspects of thermal cracking are explored in a preliminary fashion. For comparison with unconfined thermal cycling, several specimens have been subjected to 50 MPa confining pressure and thermally

cycled to 400°C. In addition, a series of thermal-shock experiments are performed for the purpose of comparing microcrack development under transient thermal conditions with that occurring during slow heating and cooling.

Our experimental program is similar to previous studies, yet differs both in manner of execution and philosophy in several significant ways. Although we too are studying how a uniform temperature change affects the physical properties of rock, our immediate purpose is to better understand how thermally-induced microcracks develop and determine what parameters affect their development. Ultimately we hope our experimental studies will let us develop a theoretical model of the fracture process. From this viewpoint, we make use of changes of certain physical properties as an aid to infer the changes in the microstructure of the rock. The monitoring of acoustic emissions has only been used in one previous study and in that instance 300°C was the maximum temperature attained (see Richter and Simmons, 1974). The acoustic emission data provides a different and more direct indication of microcrack development and promises to play a key role in improving our understanding of thermal cracking.

#### Materials and Procedures

##### Description of Rock

The Sioux Quartzite is one of the eight rock types in the U.S. Bureau of Mines standard rock suite for rapid excavation. Specimens utilized in this study are taken from the same block of Sioux Quartzite used by Friedman and Bur (1974) in their investigation of the relations among residual strain, fabric, fracture, and ultrasonic attenuation and velocity (see reprint Appendix A). Physical properties of Sioux Quartzite

as published by Krech and others (1974) and summarized in Table 1, are representative of those of our study block. The X, Y, Z coordinate system utilized in the previous study has been maintained in the present study, and all samples (19 mm in diameter by 40-70 mm long) are cored parallel to Y, i.e., the core axes are parallel to bedding, the XY plane.

The Sioux Quartzite (known commercially as Jasper quartzite) is a low porosity (0.2 - 0.4%), fine-grained (ca. 0.5 mm) sedimentary rock composed predominantly (> 99%) of tightly-packed, subrounded to rounded quartz sand grains cemented by quartz overgrowths. Petrofabric studies (Friedman and Bur, 1974) indicate that: (1) the long axes of elongate grains (long/short > 2.0) are essentially parallel to the long grain boundaries and are oriented statistically parallel to the bedding (XY) and YZ planes, (2) the c-axes of individual grains are randomly oriented, (3) intragranular, healed microfractures are essentially randomly oriented, and (4) quartz deformation lamellae are preferentially oriented so that they tend to lie at angles less than 30° to the bedding plane. Details of grain-boundary cracks are discussed in a subsequent section. X-ray diffraction measurements indicate the samples contain a residual-strain state which is characterized by the greatest elongation ( $100 \times 10^{-6}$ ) oriented subparallel to X, the intermediate principal axis ( $5 \times 10^{-6}$ ) subparallel to Y, and the least elongation ( $-85 \times 10^{-6}$ , a compressive strain), subparallel to Z.

The Sioux Quartzite is mechanically homogeneous but displays a measurable degree of anisotropy. Measurements of the bar velocity of samples cored (all parallel to Y-axis) from various parts of the block average 4.84 km/sec with a standard deviation of 2.7%, and a significant fraction

Table 1. Physical Properties of Sioux Quartzite

Property	Krech and others (1974) <sup>1</sup> mean	cv <sup>3</sup>	Current study <sup>2</sup>
Porosity . . . . . %	0.14	37.9	0.20 - 0.36
Permeability . . . . . $\mu$ m/sec	$<1 \times 10^{-4}$	--	---
Density . . . . . $10^3 \text{ kg/m}^3$	2.64	0.1	$2.634 \pm 0.008$
Shore hardness . . . . .	101	2.4	---
Compressive strength . . . . . MPa	505	8.7	---
Compressive Young's modulus . . GPa	56.4	8.2	---
Tensile strength . . . . . MPa	10.8	18.1	---
Tensile Young's modulus . . . GPa	27.9	23.7	---
Bar velocity. . . . . km/sec	4.63	3.5	$4.84 \pm 0.13$
Torsional velocity . . . . . km/sec	3.43	2.1	---
Dynamic Young's modulus <sup>4</sup> . . . GPa	56.8	6.0	69.9 - 55.0
Dynamic shear modulus <sup>4</sup> . . . GPa	31.1	4.3	---
Poisson's ratio <sup>4</sup> . . . . .	0.138	23.3	---

1. specimen axis parallel to Z-axis
2. specimen axis parallel to Y-axis
3. coefficient of variation, percent
4. calculation is based on the assumption of isotropy

of the deviation appears to result from very small differences in the water content of the samples. Measurements of compressional-wave velocities in various directions in a neighboring block (Krech and others, 1974) reveal that the rock has an orthorhombic elastic symmetry with the minimum velocity (4.9 - 5.0 km/sec) parallel to Z, the intermediate velocity (~ 5.35 km/sec) 20 - 30° clockwise from Y in the XY plane and the axis of maximum velocity (> 5.4 km/sec) 20 - 30° clockwise from X. This 10% velocity anisotropy is interpreted to be related to the preferred orientation of elongate grains and grain-boundary cracks.

#### Velocity and Attenuation Measurements

The velocity ( $V_L$ ) and attenuation ( $Q^{-1}$ ) of longitudinal waves in cylindrical specimens are determined using a forced resonance technique. The measurement system, shown schematically in Figure 1, is similar to resonance systems used elsewhere (cf. Spinner and Tefft, 1961; Davis, 1968). In contrast to most other systems, the driver and pickup consist of electrically-shielded, cork-backed, PZT piezoelectric transducers that are pressed lightly against the ends of the specimen; a thin film of grease between the transducer and sample is used to maximize mechanical coupling. By varying the frequency of a sinusoidal voltage applied to one transducer, the specimen is forced into a longitudinal mode of resonance. By sweeping from low to high frequencies and plotting output vs frequency, as shown in Figure 2. the first and subsequent harmonics of longitudinal resonance can be identified, and the longitudinal-wave velocity calculated from the expression:

$$V_L = 2\pi f_n, \quad (1)$$

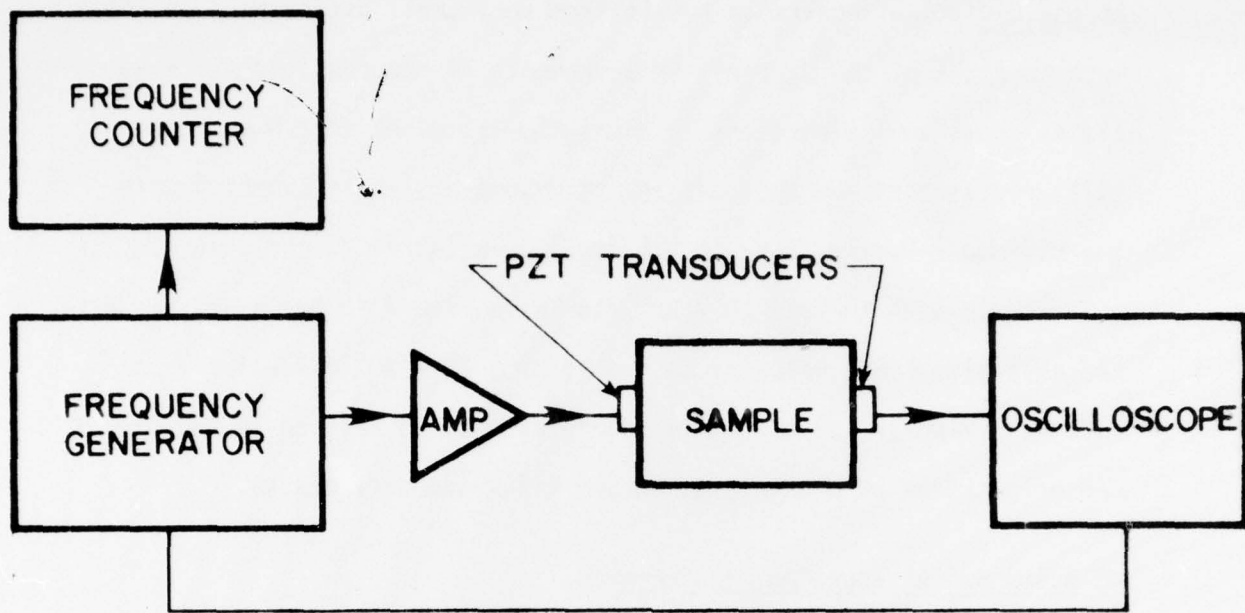


Figure 1. Block diagram of velocity measuring system.

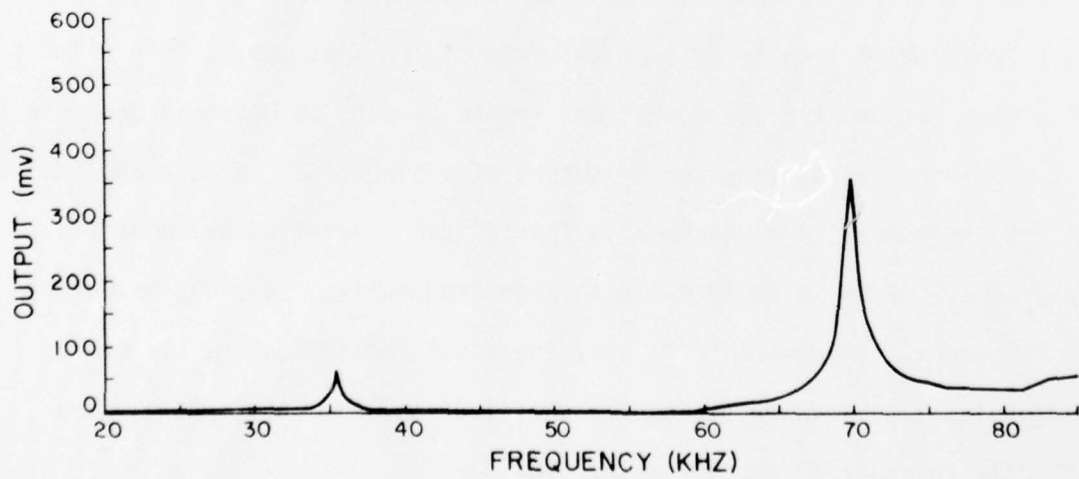


Figure 2. Output versus frequency for forced longitudinal excitation of circular cylinder of Sioux Quartzite.

where  $l$  = length of the specimen,

$n = 1, 2, 3, \dots$  = order of vibration, and

$f_n$  = resonance frequency of the  $n$ th mode of vibration.

In specimens of finite dimensions  $V_L$  is frequency dependent and is related to the bar velocity,  $V_0$ , ( $V_0 = \sqrt{E/\rho}$ ) by,

$$V_L = KV_0, \quad (2)$$

where  $K$  is a correction term dependent upon the specimen diameter-to-length ratio ( $d/l$ ), frequency, and Poisson's ratio,  $\nu$  (Bancroft, 1941).

In the present study where  $d/l = 0.1 - 0.25$  and  $\nu = 0.15$ , the correction term  $K$  ranges from 0.998 to 0.999 for velocities calculated from the first resonance peak, thus the longitudinal-wave velocity can be interchanged directly for the bar velocity with little error (~ 0.1%).

Resonance methods permit precise velocity determinations and thus should allow, in principle, detection of small velocity changes resulting from subtle changes in the microstructure of a rock. Repeated measurement of an aluminum rod indicated that our measurement system displays long-term stability and has an attainable precision of better than 0.1%. Repeated velocity measurements on samples of Sioux Quartzite also indicate a precision of 0.1%, provided the elapsed time between measurements is short (< 1 day). For longer time intervals, samples maintained at ambient laboratory conditions commonly display velocity variations greater than 0.1%, with day-to-day variations as large as 0.5% (Figure 3). For time spans on the order of tens of days the velocity variations can be on the order of 1 - 3% or greater (Figure 3).

Water appears to play a dominant role in these velocity variations,

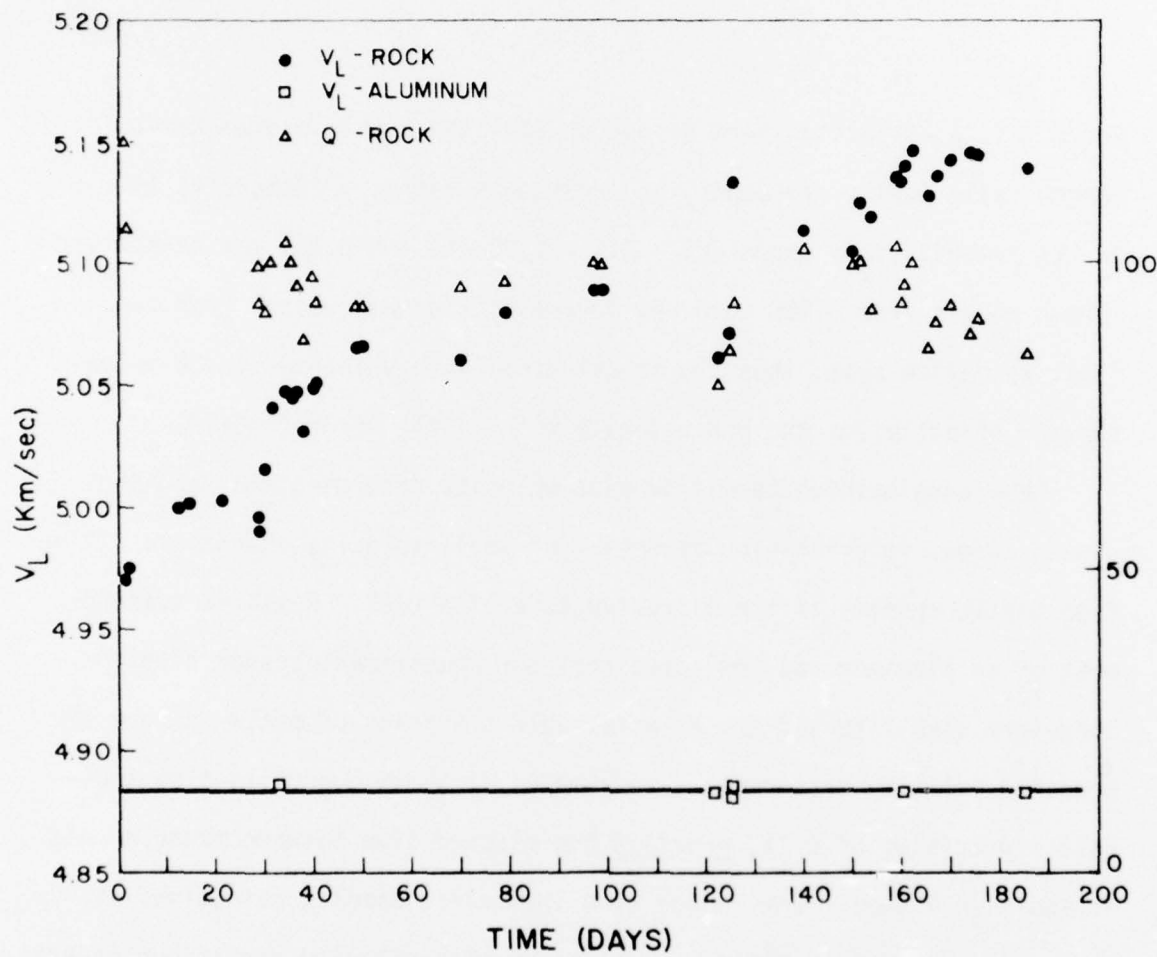


Figure 3. Longitudinal-wave velocity and Q determinations made over an extended time period on samples of Sioux Quartzite and aluminum maintained at ambient laboratory conditions.

but our studies indicate that the exact manner in which water affects the velocity in low porosity rocks (< 1 - 2%) is more complicated than indicated by the results of other workers (e.g., Nur and Simmons, 1969; Thill et al., 1973). In general terms, the lower the degree of saturation, the lower the velocity; especially noteworthy is that a small change in the water content of a nearly dry rock can result in a significant change in the velocity (up to several percent). In principle, to minimize the velocity variations, the water content should be maintained constant from measurement to measurement; yet in practice unless the most stringent steps are taken, the desired constancy of water content is difficult to achieve.

The bulk of the specimens reported on in this report were maintained at ambient laboratory conditions, consequently the actual precision of most velocity measurements is only about 1-2% as a result of humidity changes in the laboratory. More recently, however, we have changed to a procedure which more closely controls the water content, and the precision of velocity measurements over extended time intervals appears to be about 0.25 to 0.5%.

$Q$  is measured in terms of the sharpness of resonance. If  $f_1$  and  $f_2$  are the frequencies on either side of resonance at which the amplitude of vibration of the sample falls to  $1/\sqrt{2}$  times the amplitude of the resonant frequency,  $f_r$ , the quality factor,  $Q$ , is given by the relation

$$Q = \frac{f_r}{f_1 - f_2} . \quad (3)$$

It is estimated that transducer and support losses affect  $Q$  determinations by less than 10% and that the precision of measurements is 5%.

In agreement with previous studies (Barbish and Gardner, 1969; Kissell, 1972; Tittmann and others, 1973; Warren and others, 1974), our measurements (frequencies 15-45 kHz) indicate that  $Q$  displays a marked sensitivity to the presence of water, with  $Q$  varying inversely with the degree of saturation. Typically,  $Q$  of a fully dry rock is greater by a factor of 10 to 30 than  $Q$  of a fully saturated rock.  $Q$  of a "fully dry" rock is significantly affected by small changes in water content as illustrated in Figure 4, which shows the variation of  $Q$  with time after thermal cycling a sample to 455°C. The systematic decrease in  $Q$  during the

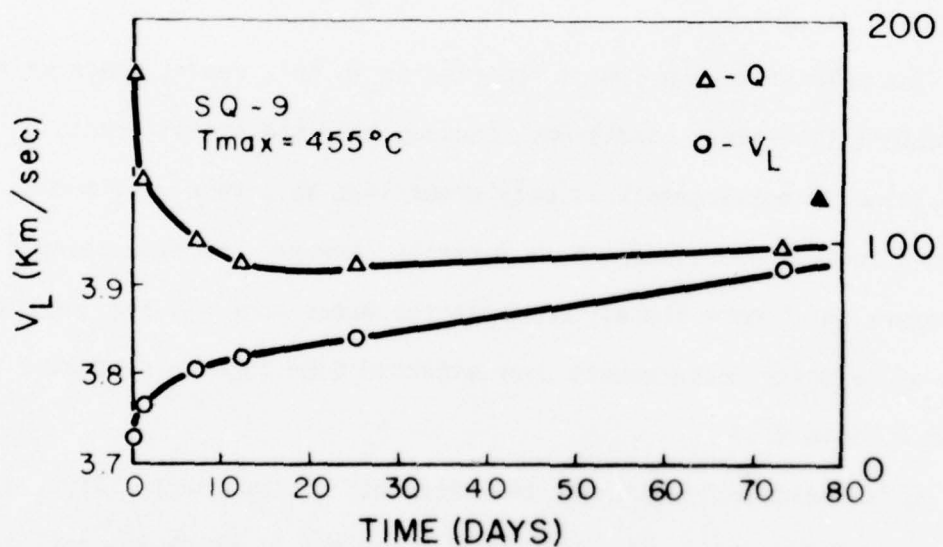


Figure 4. Variation of longitudinal-wave velocity ( $V_L$ ) and quality factor ( $Q$ ) during equilibration of an initially "fully dry" rock with laboratory humidity conditions. Solid triangle represents  $Q$  prior to heating.

first 20 days (sample maintained at ambient laboratory conditions) is interpreted to result from progressive uptake of small amounts of water from the atmosphere as the sample equilibrates from its initial "fully dry" state to laboratory humidity conditions. Consequently, if  $Q$  and changes in  $Q$  ( $\Delta Q$ ) are to be used as indices of rock microstructure and

microstructure changes, the water content of the sample must be known and comparisons of  $Q$  made at the same water content. In this regard, either a fully saturated or fully dry state are the two preferred conditions; the latter, however, is less easily achieved.

Measurements on Sioux Quartzite further indicate the  $Q$  and  $V_o$  are inter-related, but the functional relationship varies with the degree of saturation. At high and very low degrees of saturation,  $Q$  varies inversely with  $V_o$ ; Figure 4 shows the relationship for the case of a low degree of saturation. In contrast, other of our experiments reveal at intermediate degrees of saturation,  $Q$  varies directly with  $V_o$ .

#### Acoustic Emission Measurements

Acoustic emission is a transient elastic wave generated by rapid release of energy within a material. In rock, crack propagation has been shown to be a significant source of acoustic emission (cf. Hardy, 1972). Thus, monitoring acoustic emission during a thermal cycle provides a measure of fracture activity.

A schematic block diagram of the acoustic-emission monitoring system is shown in Figure 5. The acoustic-emission sensor is an electrically-shielded, PZT transducer. The signal from the sensor is preamplified and filtered before passing to the detector and counting circuitry (designed by Dr. A. F. Gangi, Texas A&M University). In contrast to other systems, the acoustic-emission signal is electronically-processed so that each acoustic-emission event that exceeds a pre-set threshold level

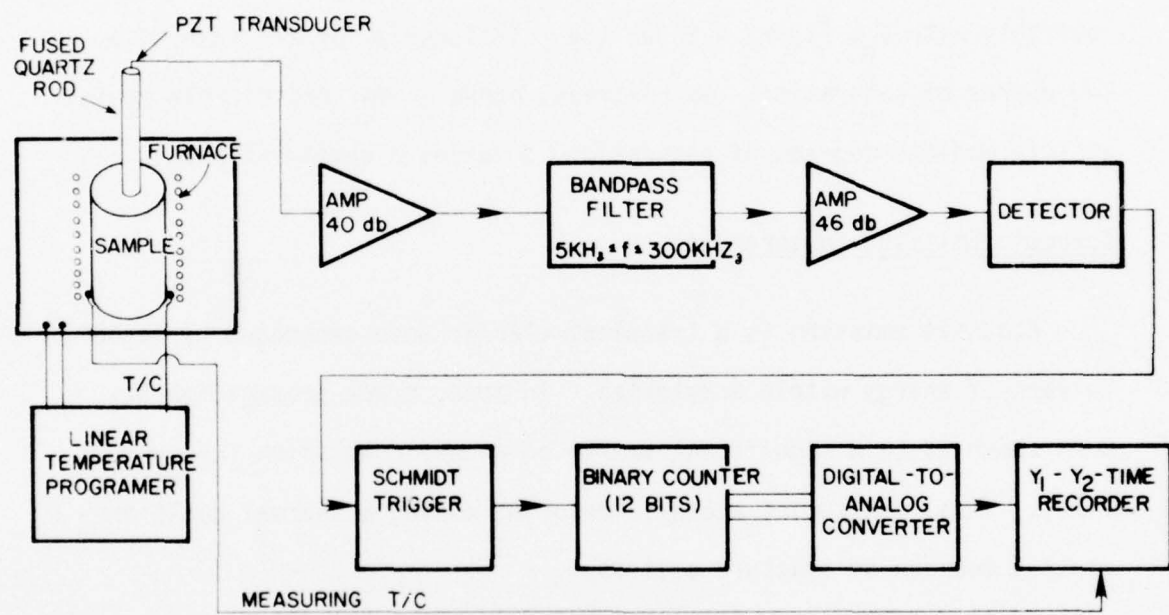


Figure 5. Schematic block diagram of the acoustic emission monitoring system.

is counted only once. The resultant DC voltage output of the counter is directly proportional to the cumulative number of acoustic-emission counts and is plotted on a strip chart along with the temperature of the specimen. The counter automatically resets to zero every 4096 counts. An overall system gain of 86 db and bandpass of 5-300 kHz is utilized. The sensor can detect a surface displacement as small as  $2 \times 10^{-7}$  mm.

The PZT transducer is not bonded directly to the specimen because temperatures attained upon heating are greater than its curie-point. Instead, the sensor is coupled to a fused-quartz rod that in turn is bonded to the sample with a strong, high-temperature resistant cement (Sauereisen cement no. 1). The fused-quartz is used as a wave guide because of its high melting point, high Q and low thermal conductivity. Unfortunately, its low thermal expansion coefficient gives rise to problems during the cooling phase of a thermal cycle.

Acoustic emission during the heating phase comes only from the sample, but during the cooling phase the acoustic emission record is dominated by emissions generated at the fused quartz-cement bond. By replacing the rock specimens with a material that does not give rise to acoustic emission upon heating (e.g., brass), it was observed that the furnace, glass rod, and bonding cement do not give rise to acoustic emission. Such is not the case upon cooling. Experiments late in our present study finally demonstrated that the anomalous acoustic emission records observed upon cooling are the result of microcracking of the fused-quartz rod at the cement bond. Thus, we lack meaningful acoustic emission data with respect to the rock's behavior during the cooling phase. Fortunately,

as later discussions show, there appears to be little microcracking activity upon cooling.

#### Petrofabric Observations

The purpose of the petrographic and petrofabric study is to (1) characterize the composition, texture, and fabric of the starting material, (2) recognize thermal fractures induced experimentally, (3) describe their orientation, location, and abundance relative to experimental parameters, and (4) correlate the above with experimental parameters and theoretical considerations in order to gain a better understanding of thermal fracture in rock. Observational studies to date have been made on discs of Sioux Quartzite cut from three specimens thermally cycled ( $\leq 2^{\circ}\text{C}/\text{min}$ ) to maximum temperatures of  $385^{\circ}$ ,  $560^{\circ}$ , and  $685^{\circ}\text{C}$  and on cylindrical discs of quartzite (19 mm diameter by 3 mm thick) that have been thermally shocked by ice-water quenching from  $400^{\circ}\text{C}$ .

Microfracture index. The abundance of intragranular microcracks is expressed as a microfracture index, FI, which is based on fracturing in 400 grains as follows: percent unfractured grains  $X_1$ , plus the percent of grains with 1-3 fractures  $X_2$ , plus percent with 4-6 fractures  $X_3$ , plus the percent of those with 6-10 fractures  $X_4$ , plus the percent of those with  $> 10$  fractures per grain  $X_5$ , all  $\times 100$  (Friedman, 1963, p. 18, Table 1). The index may vary from 100 to 500. Indices determined here are reproducible to  $\pm 2\%$  and are used to compare relative amounts of fracturing among specimens.

Staining technique. It is essential to be able to recognize thermally-induced fractures, distinguish them from microfractures relict from some previous natural deformation, and from fractures that might arise

from relaxation of residual stresses upon thin section preparation. Distinction between thermal cracks and relict natural ones is achieved readily in that the former are fresh and unhealed whereas by far most of the latter are healed, i.e., there has been a rebonding of the silica across the fracture and the fracture surface is invariably decorated with natural impurities. Both thermal cracks and those that might arise from thin section preparation (relaxation of residual stress) are unhealed, however, and impregnation prior to sectioning with a suitable stain is necessary to distinguish between the two. Staining methods that involve heating the specimen (e.g., Baldridge and Simmons, 1971; and Simmons and others, 1975) need to be avoided as the specimens here are to be subjected to a specific thermal treatment. A room-temperature staining technique was sought, and the one suggested by Mr. D. A. Parker, National Petrographic Service Co., Houston, Texas, was found to work satisfactorily. Before sectioning, the disc-shaped specimen is impregnated under vacuum with a blue-stained, thinned epoxy which is allowed to harden at room temperature. First, Shell Chemical Epoxy, R-815 Resin (Ring Chemical Co., Houston, Tx.) is thinned up to 30% by volume with BGE reactant diluent (I.W. Industries, Houston, Tx.). The mixture is then stained a dark blue with Kriegrosol blue supra concentrated powder (7-K Color Corp., Hollywood, Ca.). A hardener, Geramid 2000 (Ring Chemical Co., Houston, Tx.) is then added up to 50% by volume. This mixture has a low viscosity liquid-life of about an hour. The chip is immersed in a cup of the mixture and evacuated for 30 minutes. Then it is removed from the epoxy bath and allowed to harden at room temperature for 12 to 25 hours before a thin section is prepared. In thin section, the blue-stained

epoxy is sky-blue in color and fills the finest of cracks and grain boundary openings. It appears to fill its container completely, i.e., no shrinkage upon hardening. Expansion upon hardening cannot be ruled out, but it does not appear to be a serious problem.

The specimens cycled at about  $2^{\circ}\text{C}/\text{min}$  are studied in polished section with optical and SEM. Surfaces are polished with abrasives down to  $3.0 \mu\text{m}$ , impregnated with epoxy, and then further polished with  $0.3 \mu\text{m}$  alumina. The epoxy fills parted grain boundaries and cracks and simplifies their study optically. For SEM work an attempt was made to remove the epoxy prior to coating the surface with the standard  $200 \text{ \AA}$ -thick layer of gold-palladium by treating the surface with a solution of 5% bromine and 95% ethanol for 12 hours. Epoxy remains in some of the parted grain boundaries but is dissolved completely from others. Reflected light microscopy through the gold-palladium coating enhances best of all the visibility of parted grain boundaries and intragranular microfractures.

## RESULTS

### Velocity Changes

The irreversible effect of slow heating and cooling upon the longitudinal-wave velocity is shown in Figures 6 and 7. Figure 6 shows the ratio of the post-heating velocity ( $V^p$ ) to the pre-heating velocity ( $V^i$ ) as a function of the maximum temperature ( $T_{\max}$ ) attained during a thermal cycle. Whereas, Figure 7 shows the absolute velocity as a function of  $T_{\max}$ ; in this case, except for the initial room temperature data, the velocity is measured immediately after removal of the sample from the

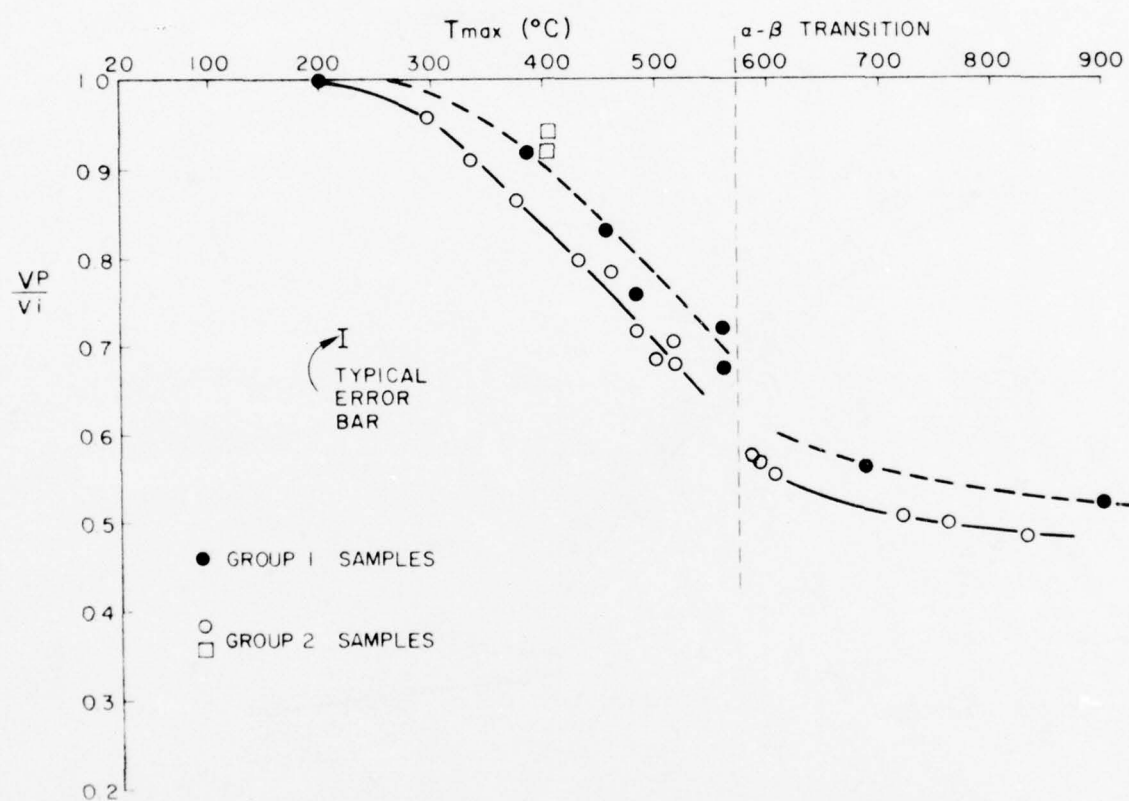


Figure 6. Variation of normalized, post-heating velocity with maximum temperature attained during a thermal cycle.  $V_P$  and  $V_i$  are post-heating and pre-heating longitudinal-wave velocities, respectively and are measured "room dry". Group I samples (solid symbol) and Group II samples (open symbol) are cored from two different parts of the source block of Sioux Quartzite. All samples were thermally cycled at atmospheric pressure, except for two samples (open squares) which were thermally cycled under 50 MPa confining pressure.

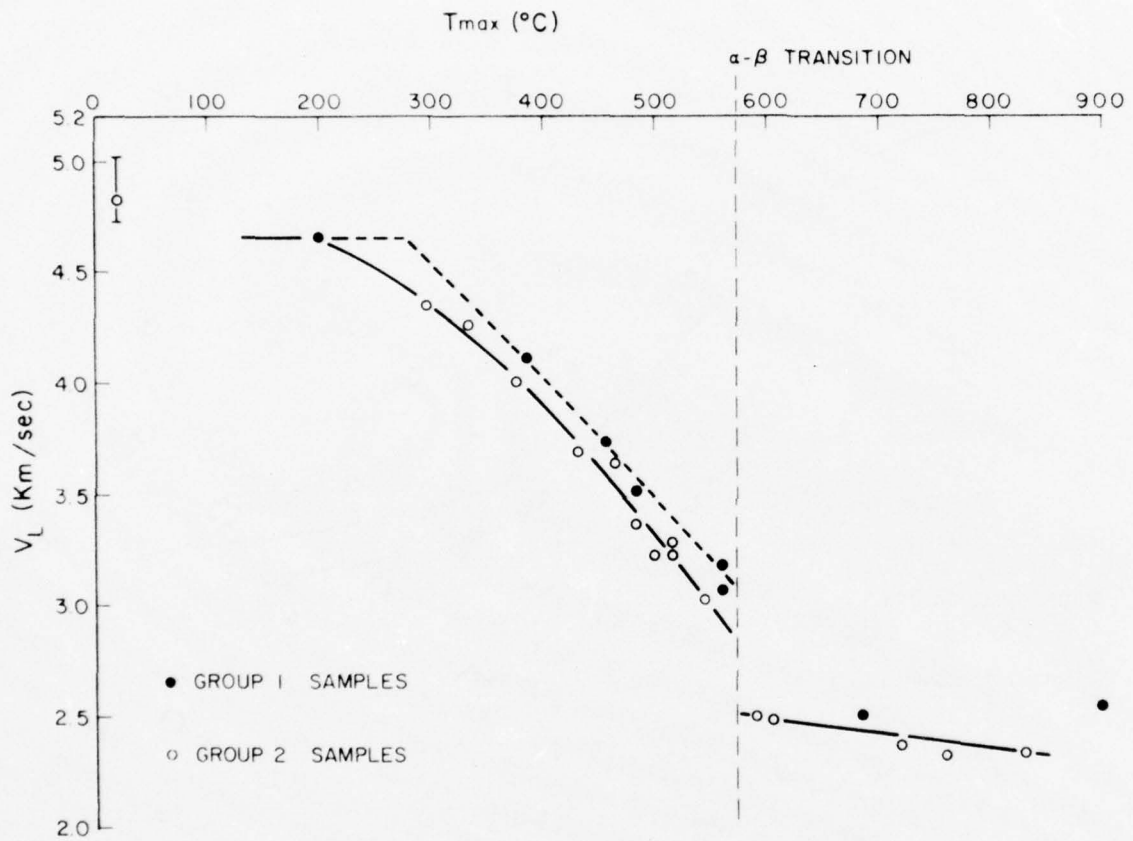


Figure 7. Variation of longitudinal-wave velocity with the maximum temperature attained during thermal cycling. All measurements are for fully dry samples, except for the initial room temperature measurements. The data is differentiated (open vs solid symbols) according to the location of the sample in the source block of Sioux Quartzite.

furnace and corresponds to that of a "fully dry" specimen. In Figure 6, the post-heating velocity,  $V^P$ , corresponds to the velocity measured after the sample has re-equilibrated to laboratory humidity conditions. Because the pre-heating velocity,  $V^i$ , is measured at ambient laboratory conditions, the re-equilibration is essential if the velocity ratio,  $V^P/V^i$ , is to reflect only the effects of thermally-induced microcracks and not additional effects due to differing water contents. The importance of achieving re-equilibration is underscored by the observation that the "fully dry" velocity is lower by up to 6% (see Figure 4). Nevertheless, laboratory humidity changes with time, hence it is not possible in every case to be sure the effect of differing water contents has been completely eliminated. This results in a potential source of error.

Interpretation of the velocity data is dependent in part upon understanding the scatter in the data points. Part of this scatter possibly can be attributed to error associated with differing water content, as mentioned above. The maximum error introduced from this source, however, is only about 2 to 3%. A more significant component of the scatter appears to be associated with subtle microstructure differences from sample to sample. When the original location of the sample in the study block is taken into account, these differences appear to be systematic. This is demonstrated by distinguishing the data points in Figures 6 and 7 according to which of two distinct beds in the study block the samples are taken. As can be seen, one group (the solid circles, Group I) falls consistently above the other (the open circles, Group II). Such a distinct difference, especially in Figure 6, is impressive considering the small difference in initial velocities for these two groups; Group I

samples have a pre-heating average velocity of 4.78 km/sec, whereas Group II samples have a pre-heating average velocity of 4.84 km/sec. We are currently attempting to determine the initial microstructure differences of these two groups, but tentatively it appears that Group I has a slightly smaller average grain size than Group II. Segregation of the data into two distinct groupings simplifies interpretation of the velocity data.

Examination of the data indicates that upon exceeding a threshold temperature between 200°C and 300°C, the velocity (for both data groups) decreases approximately 10% for each 100°C increase in  $T_{max}$ , up to the  $\alpha$ -quartz to  $\beta$ -quartz transformation (573°C). At the  $\alpha$ - $\beta$  transition, there is evidence of an abrupt velocity decrease of approximately 10%. From 573°C to 900°C, the velocity continues to decrease, but at a significantly lower rate (ca. 3%/100°C). A concerted effort is not made to determine precisely the threshold temperature on the basis of velocity changes, because the acoustic emission data (as shown subsequently) is a more sensitive indicator. On the basis of the velocity data, however, it might be anticipated that the threshold temperature is different for the two sample groups.

A 50 MPa confining pressure reduces but does not completely suppress the thermal cracking of Sioux Quartzite. Two exploratory thermal cycling experiments to 400°C (the open squares, Figure 6) show the velocity decrease (measured at atmospheric pressure) is less than 50% of that resulting at unconfined conditions (Group II samples).

#### Quality factor changes

There is little doubt that cracks play a role in determining the Q of a low porosity rock. The exact role, however, is not fully understood. A commonly proposed model relates dissipation of elastic strain

energy during passage of a stress wave in dry rock to frictional sliding of contacting crack faces (e.g., Walsh, 1966; Gordon and Davis, 1968). On the basis of this model an increase in the number of cracks might be expected to result in a decrease in  $Q$ , because there is likely to be a greater number of potential sites for sliding contacts to develop. When water is present,  $Q$  is significantly affected. There is a change in the relationship between  $Q$  and the microstructure of the rock. This is particularly apparent in our measurements of  $Q$  before and after a thermal cycle for room dry and water-saturated rock.

Initial values of  $Q$  for "room dry" Sioux Quartzite range from 60 to 250, with 100 being a typical value. The cause for the wide spread of values is uncertain, but it appears primarily to reflect slightly differing degrees of saturation amongst the samples, although microstructural differences cannot be completely ruled out. The pronounced effect of water on  $Q$  of a "room dry" rock poses a problem when attempting to assess microstructure changes on the basis of changes in  $Q$ . The influence of water on  $Q$  may in some cases overshadow the effects of small changes of microstructure. In other instances, the problem is to differentiate whether an observed change in  $Q$  after a thermal cycle is the result of microstructure changes or small differences in water content or a combination of the two. The problem is well illustrated in Figure 8, which shows the ratio of the post-heating  $Q$  ( $Q^P$ ) to the pre-heating  $Q$  ( $Q^I$ ) (both measured "room dry") as a function of the maximum temperature of the thermal cycle. The only definitive statement permitted by the data is that between 200°C and 550°C,  $Q$  is unchanged or decreases,

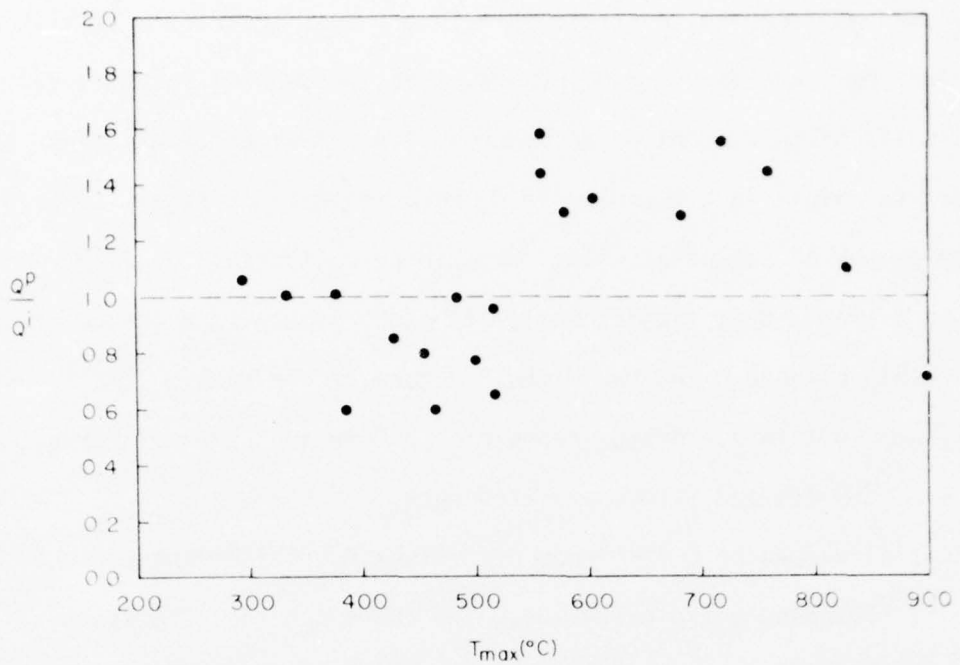


Figure 8. Effect of thermal cycling on the Q of "room dry" Sioux Quartzite. The post-heating value,  $Q^p$ , is normalized with respect to the pre-heating value,  $Q^i$ .

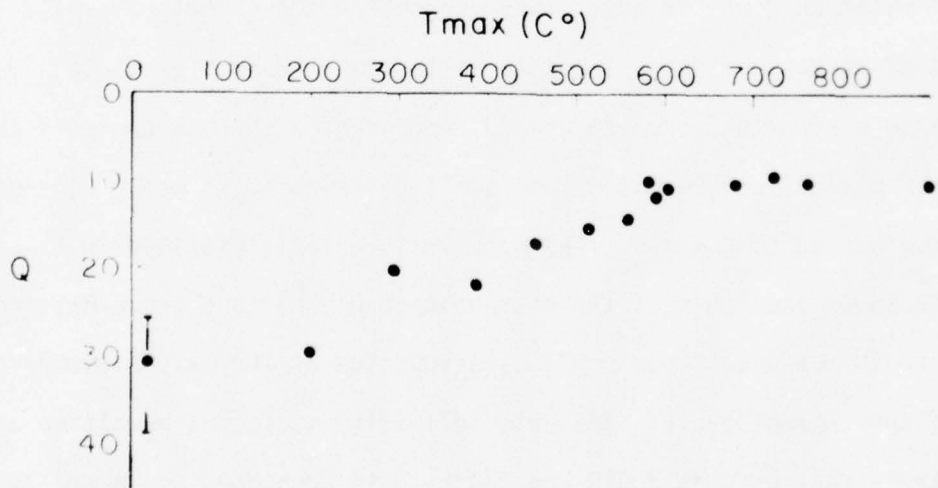


Figure 9. Effect of thermal cycling on the Q of water-saturated Sioux Quartzite.

whereas between 550°C and 800°C, Q increases. The scatter in the data is interpreted to result primarily from the effects of slightly differing water contents from one measurement to the next and from sample to sample.

In contrast to a "room dry" state, Q of a fully saturated rock displays a systematic variation with increasing thermal cycling temperature. Figure 9 shows that from initial Q's of 25 to 40, Q progressively decreases with increasing maximum temperature of heating, up to the  $\alpha$ - $\beta$  transition. Above the transformation temperature, Q remains essentially constant at a value of 10. The Q of a saturated rock thus appears to provide an indication of microstructure changes occurring during the thermal cycle. It is not necessarily the same microstructure changes, however, that a change in Q of a fully dry rock might reflect, because attenuation is dominated by differing mechanisms in each of these cases. Attenuation in the saturated rock is thought to be in accordance with a mechanism proposed by Biot (1956). In this case, energy dissipation results from relative motions between the pore fluid and solid framework, primarily as a result of stress-induced flow of water in the interconnected pore space. As the permeability increases, Q decreases.

#### Porosity Changes

Figure 10 shows the increase of apparent total porosity with increasing temperature of the thermal cycle. Initial porosity ranges from 0.2 - 0.4%, but increases to 1% upon heating to 900°C. Although not evident on Figure 10, detectable increases in porosity occur at 300°C. The porosity increases progressively with increasing temperature, marked by a rapid increase at the  $\alpha$ -quartz to  $\beta$ -quartz transformation temperature. There

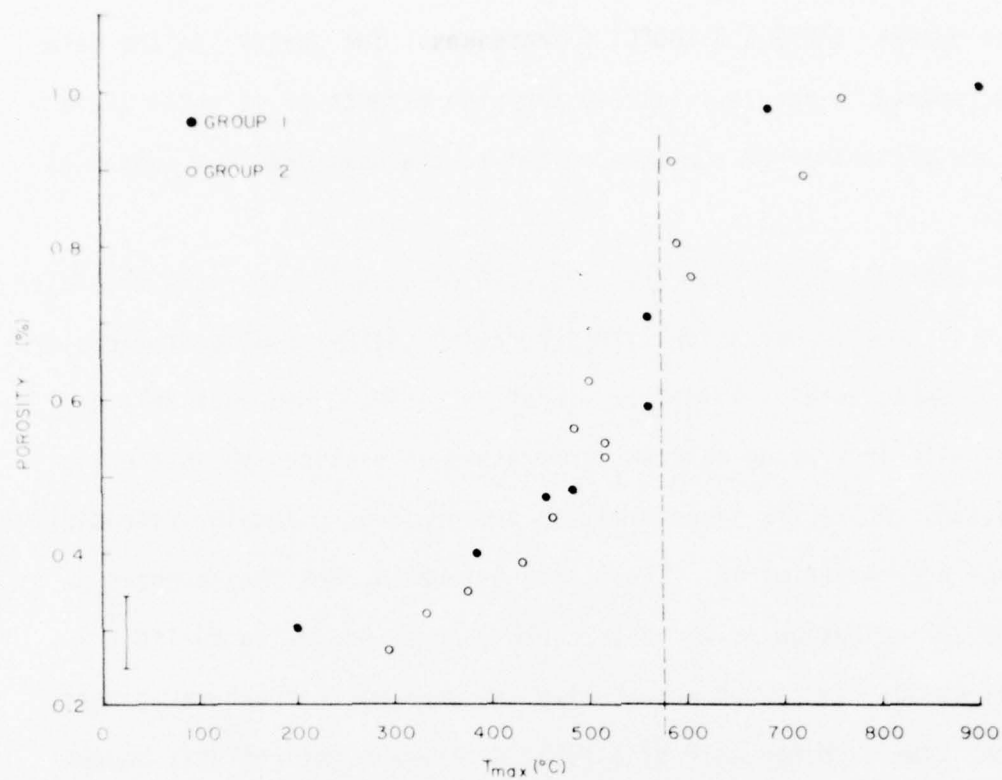


Figure 10. Variation of the porosity of Sioux Quartzite with the maximum temperature attained during slow thermal cycling.

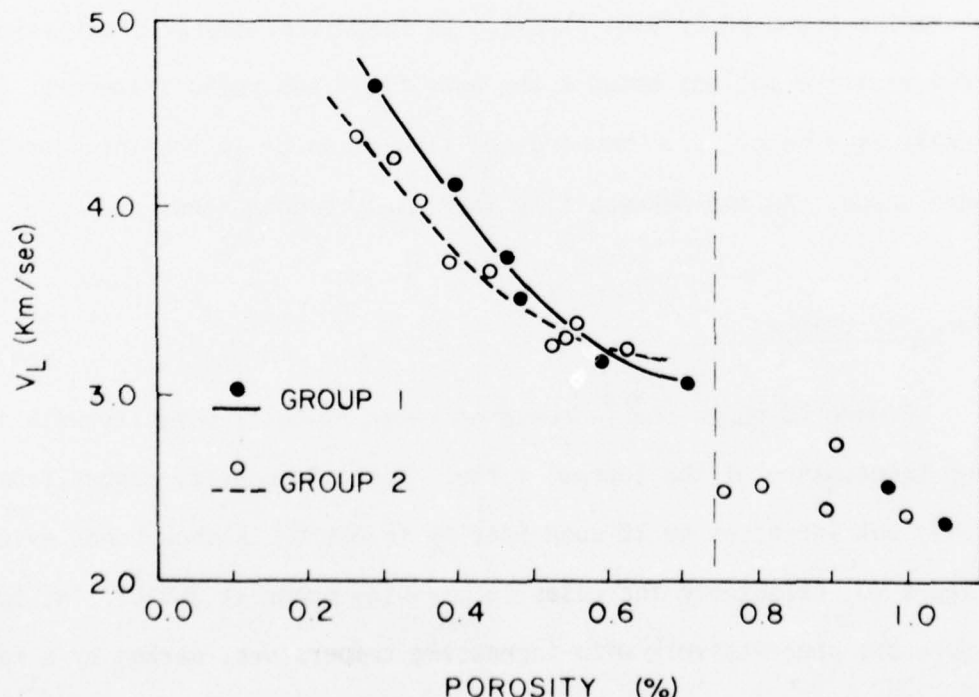


Figure 11. Relation between the longitudinal-wave velocity and porosity of thermally cycled Sioux Quartzite. The data points to the left of the dashed vertical line correspond to samples heated to temperatures below the  $\alpha$ - $\beta$  transition of quartz.

is some indication that the rate of porosity change decreases above 700°C.

The relationship between longitudinal-wave velocity and total porosity for thermally-cycled samples, is shown in Figure 11. The prominent inverse relationship between velocity and porosity for samples heated to temperatures less than 573°C indicates that a significant component of the new porosity is associated with low aspect-ratio cracks (Nur and Simmons, 1969; 1970). For samples heated above 573°C, however, the velocity appears to be little affected by additional porosity increases, even though the absolute porosity is still small (~ 1%). This lack of sensitivity is an indication that the additional porosity (above that developed at 573°C) is associated predominantly with high aspect-ratio cracks or pores.

#### Acoustic Emission

Technical difficulties prevented us from obtaining meaningful acoustic-emission data until the latter part of the present study. Consequently, we have data only for a limited number of tests, and of these, all but one are Group II samples.

Representative plots of cumulative emission and emission rate versus temperature are presented in Figure 12 and Figures 13 and 14, respectively. Of particular significance is the marked similarity of acoustic emission activity from test to test. In general, upon exceeding a threshold temperature, emission increases progressively, attains a maximum (between 280°C and 400°C) and then decreases, commonly abruptly; a second larger maximum occurs between 570°C and 590°C, coincident with the  $\alpha$ - $\beta$  transition

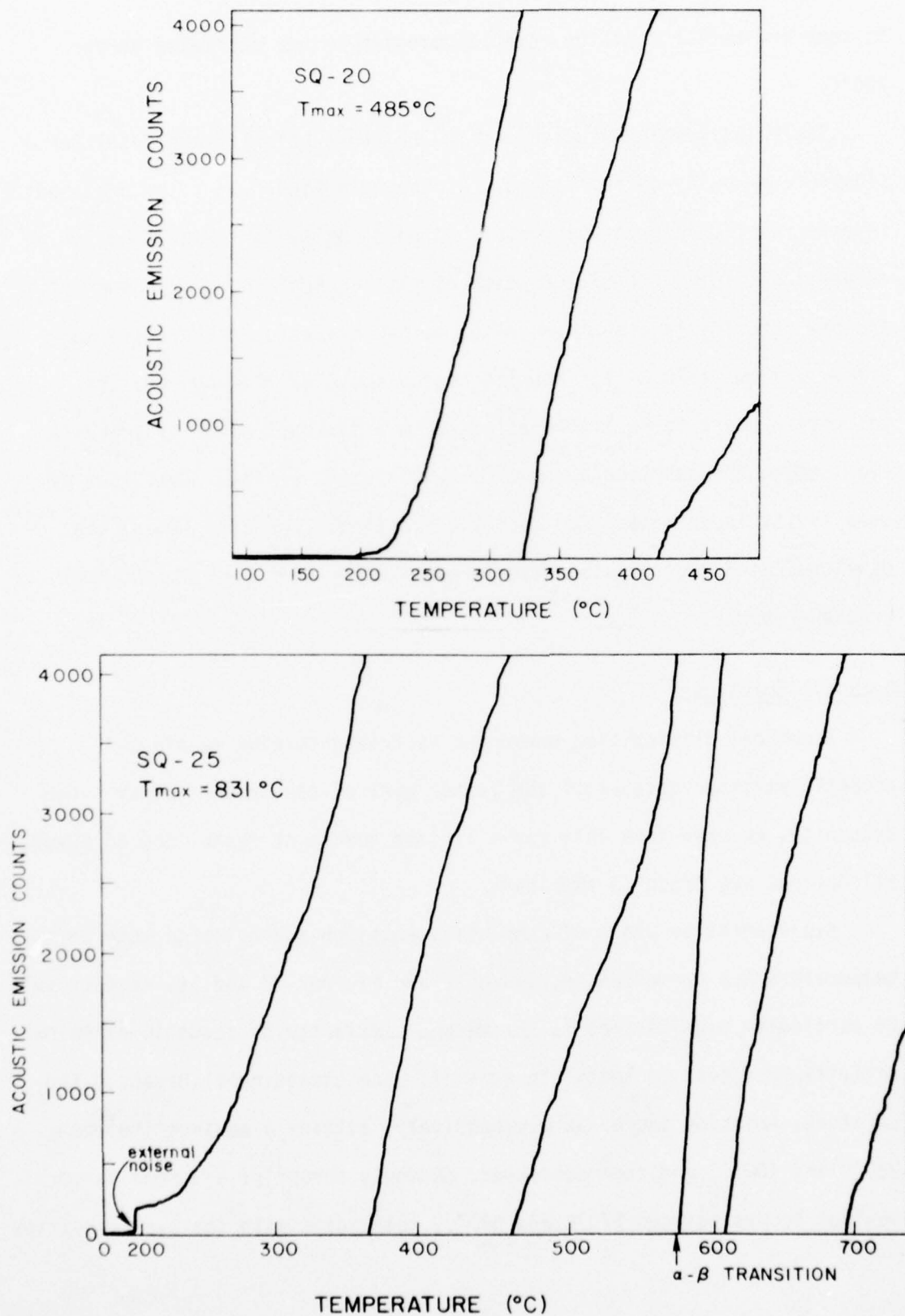


Figure 12. Representative records of cumulative acoustic emmission versus temperature for slow heating of Sioux Quartzite.

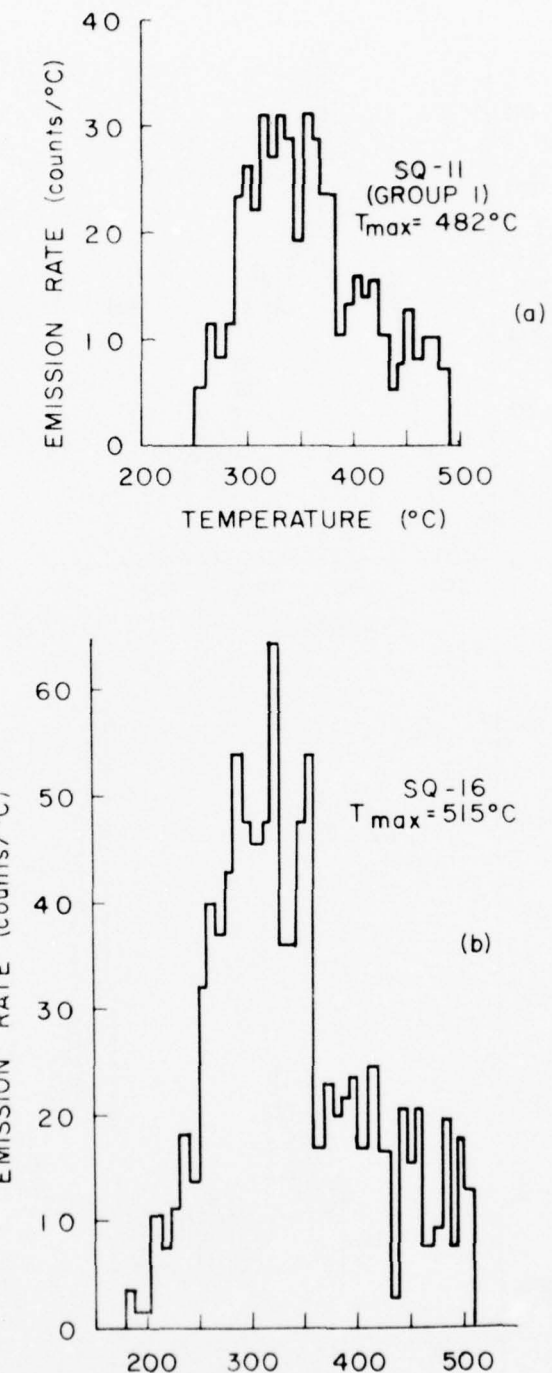


Figure 13. Representative plots of acoustic emission rate versus temperature for slow heating of Sioux Quartzite. a) Group I sample; b) Group II sample. The emission rate is averaged over a temperature interval of 8 °C.

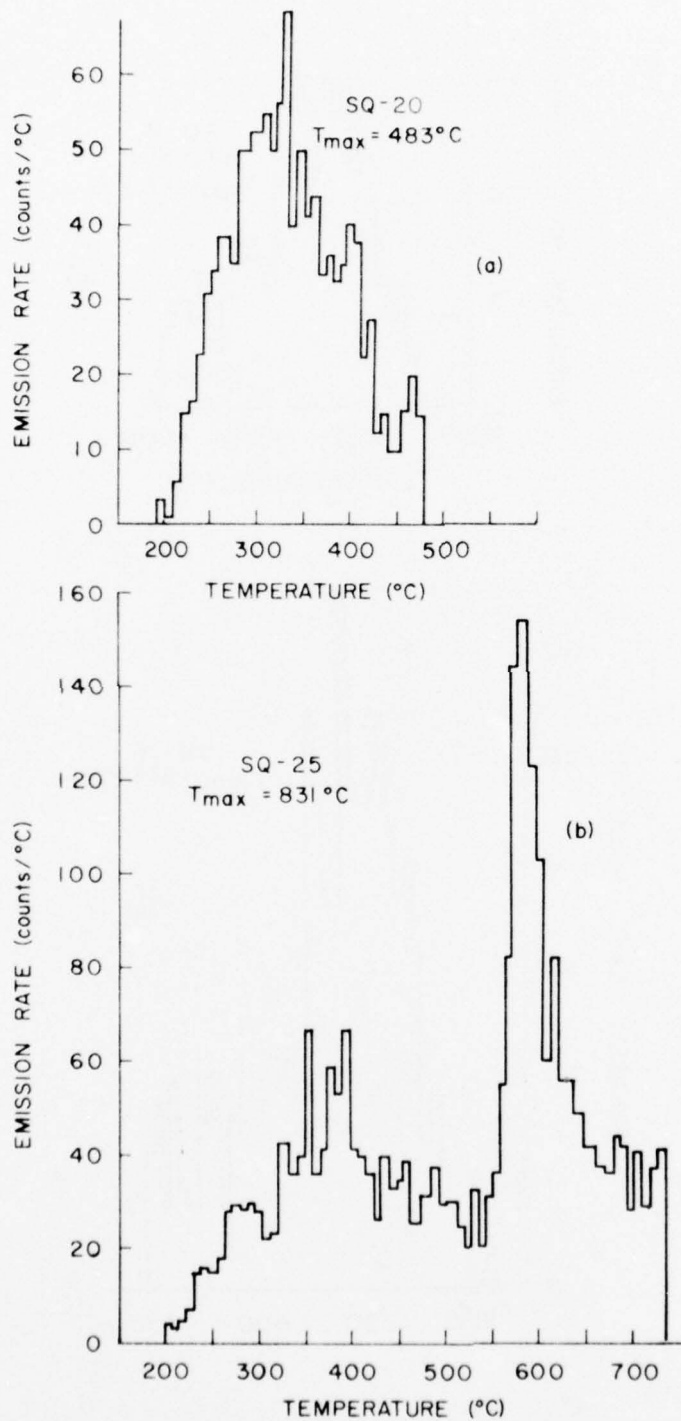


Figure 14. Representative plots of acoustic emission rate versus temperature for slow heating of Sioux Quartzite. The emission rate is averaged over a temperature interval of 8 °C.

(Figure 14b). The onset of acoustic emission occurs at  $206 \pm 10^\circ\text{C}$  for Group II samples (8 experiments) and at  $250^\circ\text{C}$  for the Group I sample. The greater threshold temperature for the Group I sample is consistent with the velocity data (Figure 6). Note also (Figure 13) that aside from the higher threshold temperature, the general character of acoustic emission versus temperature for the Group I sample is very similar to that of Group II samples.

Upon termination of heating and maintenance of a constant temperature, acoustic emission decreases abruptly to a very low rate, with complete termination usually following within minutes thereafter. Upon slow cooling no emissions are recorded during the first 100 to 150 degrees, after which intense emission activity initiates and continues until cooling is complete. The preponderance of these emissions do not appear to be coming from within the sample, but instead result from fracturing of the fused-quartz rod/cement bond.

#### Petrofabric Observations

Slowly cycled specimens. Polished surfaces of specimens 8, 10, and 4 (cycled once at about  $2^\circ\text{C}/\text{min}$  to maximum temperatures of  $385^\circ$ ,  $560^\circ$ , and  $685^\circ\text{C}$ , respectively) and of the starting material are studied to characterize development of thermally-induced cracks. The following facts are apparent in both reflected-optical and scanning-electron microscopy:

1) parting of grain boundaries progressively increases with increasing maximum temperature (Figure 15);

2) microfracture indices also progressively increase from 107 in the starting material to 122, 138, and 141 in specimens 8 (385°C maximum temperature), 10 (560°C) and 4 (685°C), respectively. That is, the abundance of intragranular microfractures (Figures 16b, 17c, d) also increases with increasing maximum temperature; and

3) traces of intragranular microfractures on the polished surfaces are strongly oriented subparallel to the ZY plane (Figures 18 and 17c, d). This fabric is documented only in specimen 4 where clear distinction between grain boundary and intragranular microfracture is possible.

The progressive increases in grain-boundary parting (cracking) is conspicuous in photomicrographs (Figure 15) and is not quantified further. Note in the starting material (Figure 15a) that the boundaries are indistinct and incomplete. They are somewhat more conspicuous and continuous in specimen 8, but reach maximum development in specimen 4 (Figures 15d and 17c, d) where every grain boundary is conspicuously parted. At higher magnification the morphology of parted boundaries in the thermally treated specimens is not conspicuously different from that in the starting material (Figure 16a, b). Although the fracturing along the boundaries is complex and small dislodged fragments are apparent (Figures 16, 17b) there is no compelling reason to suspect shear displacements along these boundaries.

Intragranular microfractures often intersect the grain boundaries at high angles and die out into the grain (Figures 16, 17c, d). They also are developed within the grain and, at least in two-dimensions,

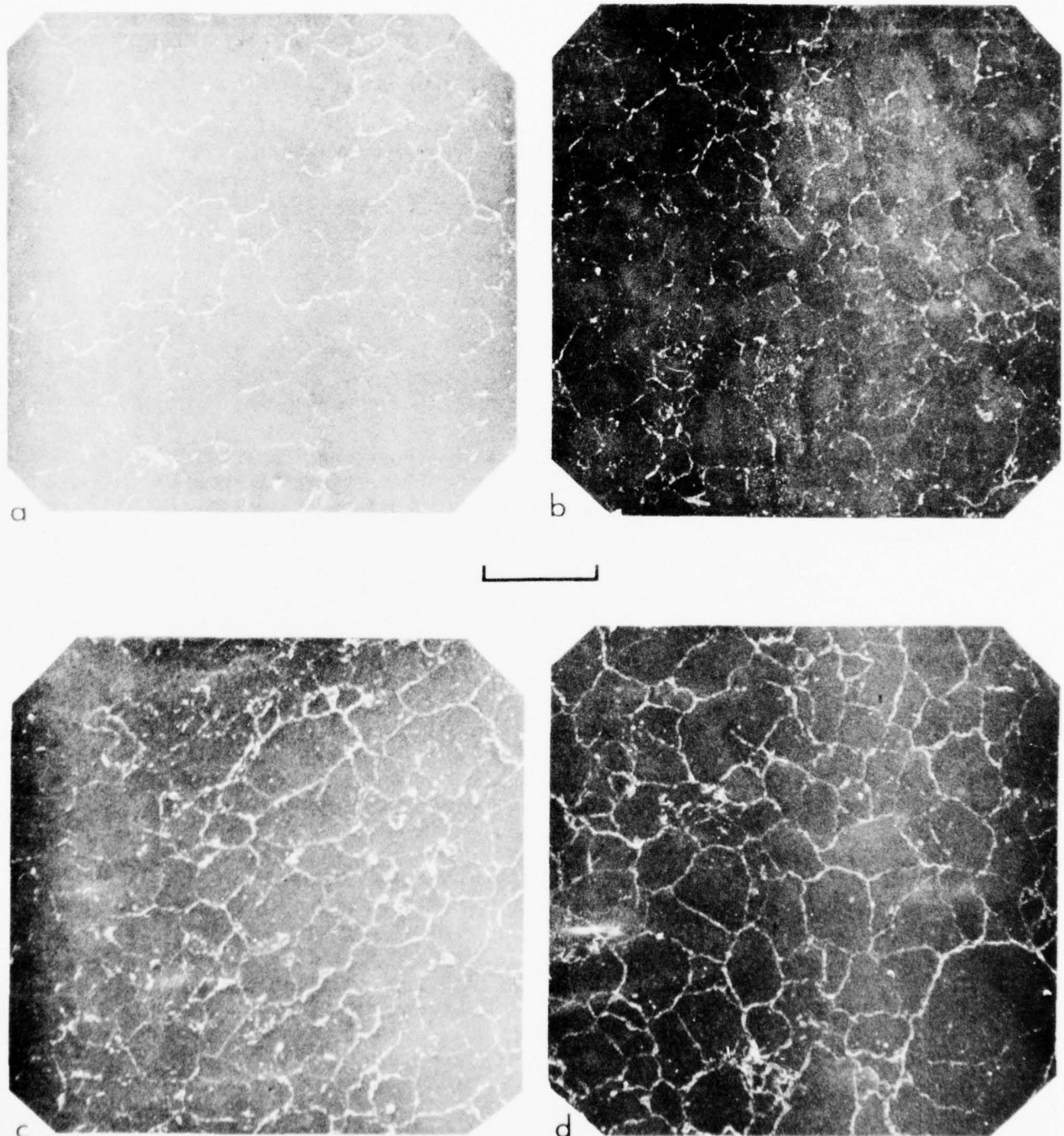
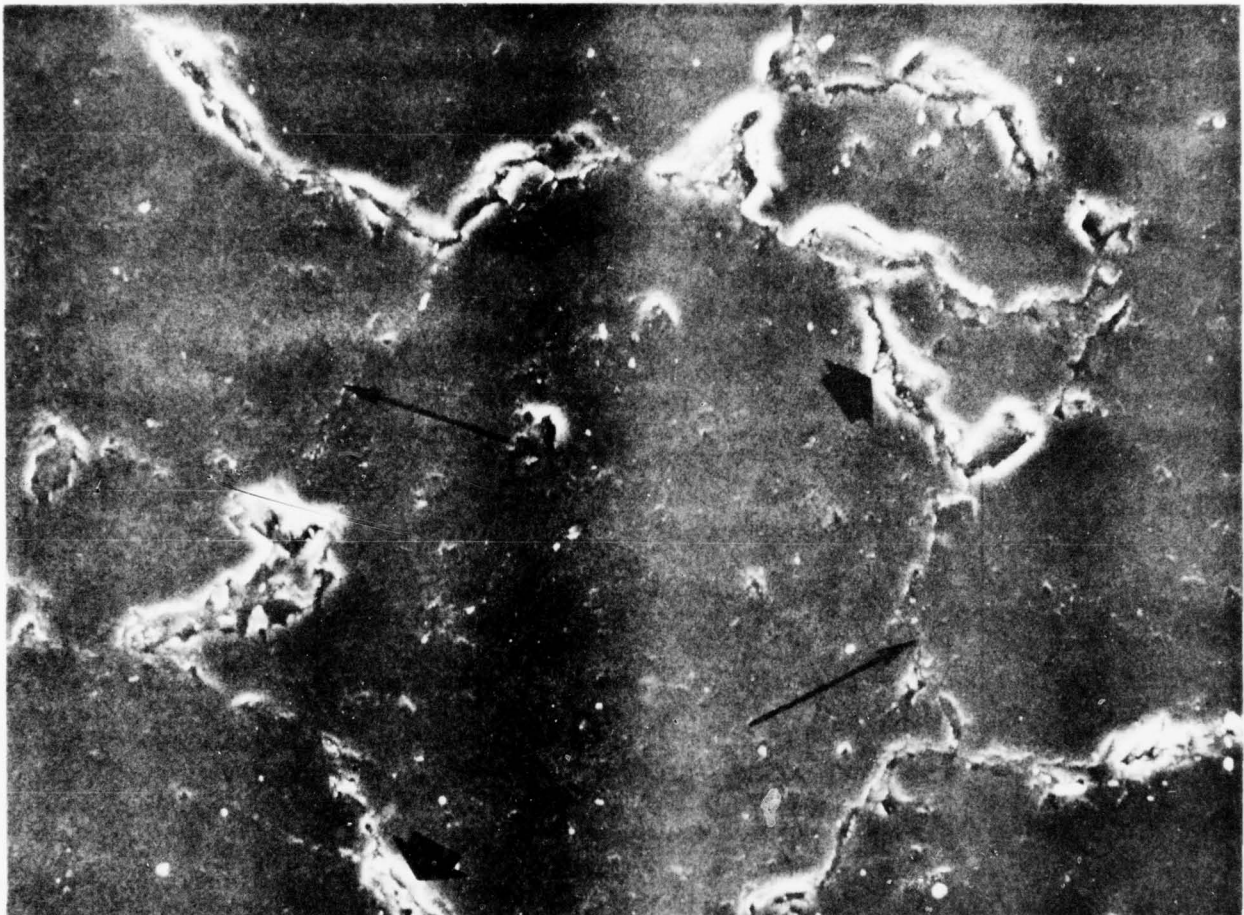
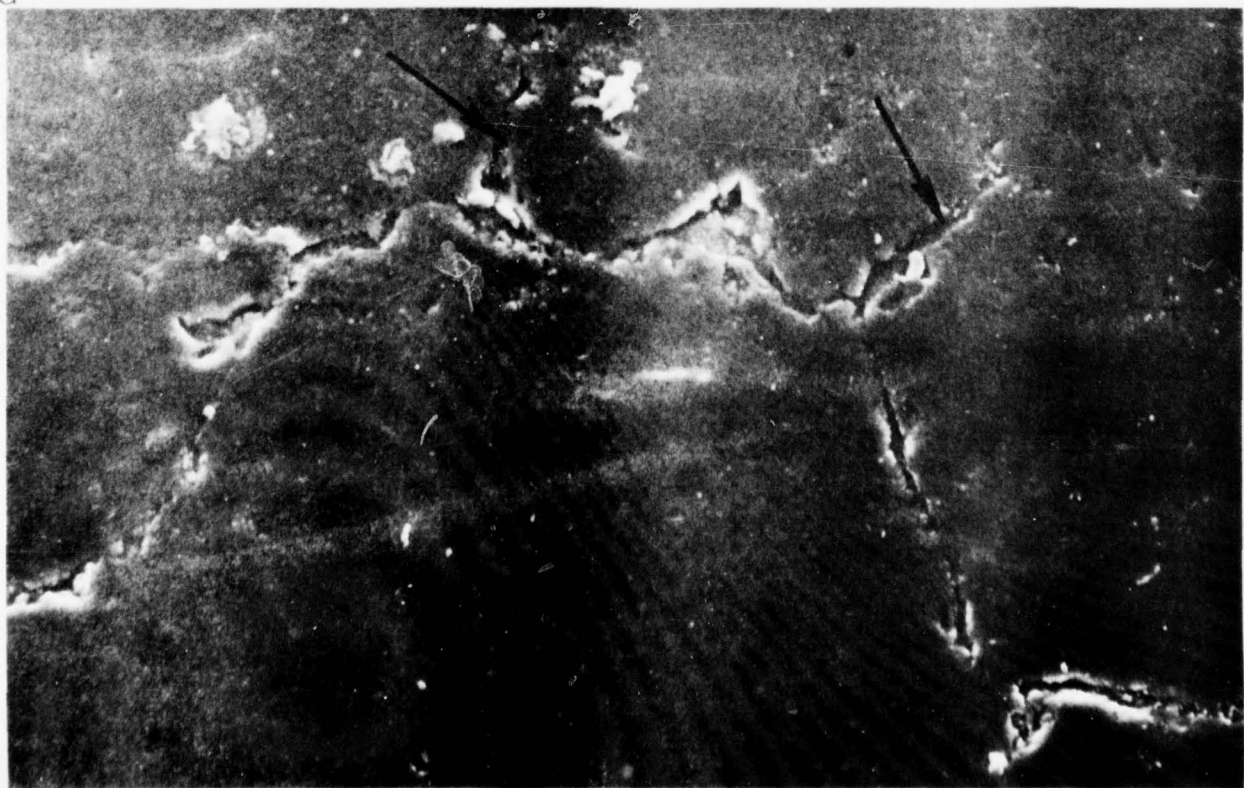


Figure 15. Scanning electron photomicrographs show development of grain-boundary partings in (a) thermally untreated starting material, and in (b, c, and d) specimens 8 ( $385^{\circ}\text{C}$ , maximum temperature), 10 ( $560^{\circ}\text{C}$ ), and 4 ( $685^{\circ}\text{C}$ ), respectively. The boundaries become more conspicuous and continuously developed with increasing maximum temperature. Scale line for all is 0.05 cm.

Figure 16. SEM photomicrographs show parted (bold arrows) and unparted boundaries (slim arrows) in (a) and intragranular microfractures (arrows) in (b), Sioux Quartzite specimen 8, 385°C, maximum temperature. Scale line is 0.004 cm.



A



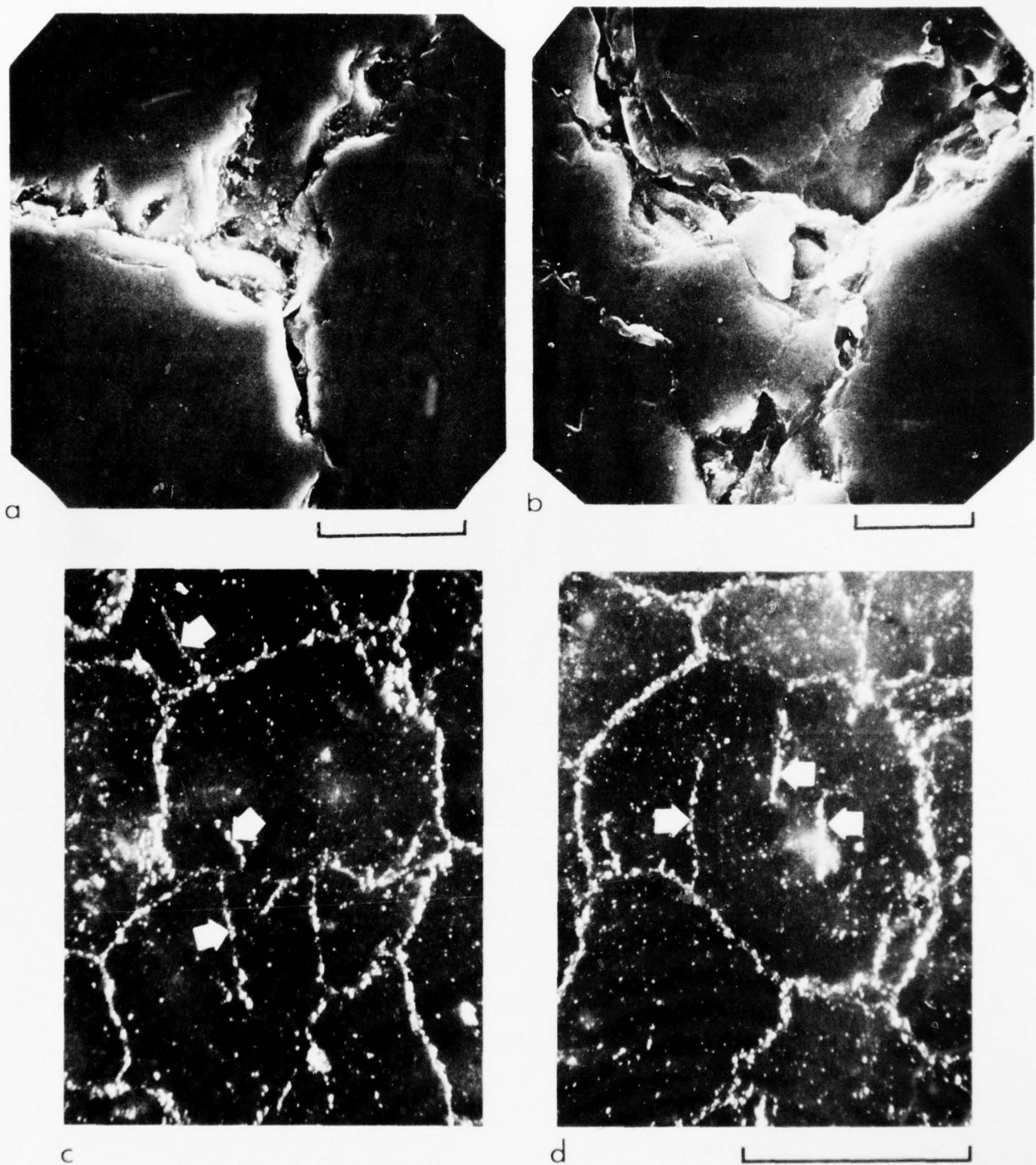


Figure 17. SEM photomicrographs show parted, triple-point, grain-boundary junction in starting material (a) and in specimen 4 (b) heated to 685°C. Side cracking and fragment production are somewhat greater in the thermally treated material (b). In (c and d) are reflected light photomicrographs taken through the gold-palladium coating that show intragranular microfractures (arrows) and completely parted grain boundaries in specimen 4. Scale line for (a) is 0.002 cm, that for (b) is 0.001 cm, and that for (c and d) is 0.05 cm.

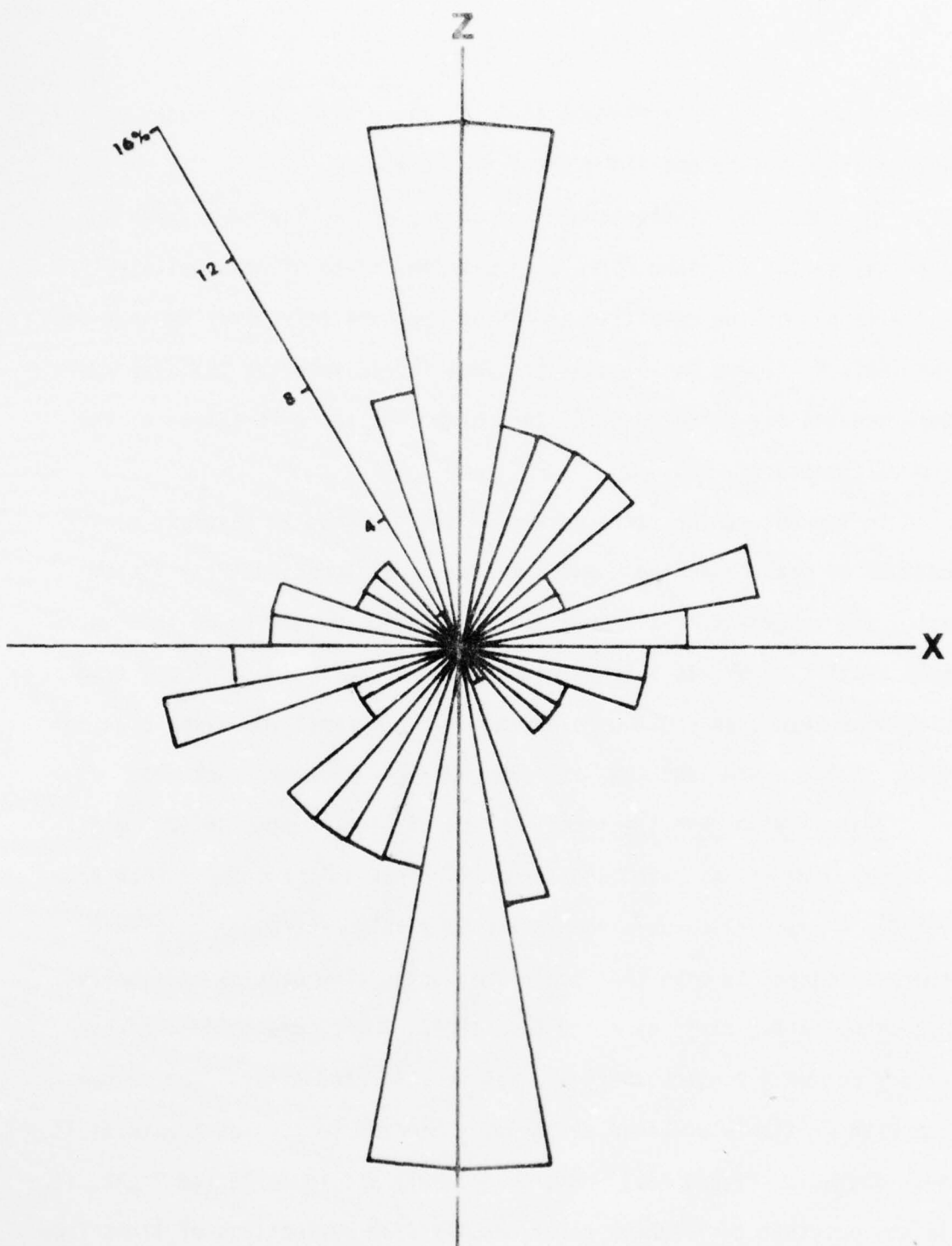


Figure 18. Frequency diagram shows orientation of the traces of 163 intragranular microfractures on the polished surface of specimen 4 (cycled to 685°C). The microfracture traces are oriented preferentially subparallel to the ZY plane.

appear independent of grain-boundaries. There also is no reason to suspect shear displacement along these fractures.

The preferential development of intragranular microfractures subparallel to the ZY plane correlates with the state of residual strain and with one of the resulting trends of fracture anisotropy in this rock (Appendix A, Figure 4a, b, and d). This fabric suggests that the residual strains may be influential in controlling the orientation of the thermal fractures.

In the future the surfaces also will be etched to disclose modifications of smaller scaled phenomena such as dislocation arrays (etch pits) and subgrains. Also specimens 4, 8, and 10 need to be studied in thin section to obtain a three dimensional appreciation of the intragranular microfractures and the relation between thermal and elastic anisotropy in the grains and the parted boundaries and microfractures.

Thermally-shocked specimens. Discs of Sioux Quartzite (20 mm diameter by 3 mm thick) have been thermally shocked (ice-water quench from 400°C) in order to compare thermal-crack development under transient thermal conditions with that occurring during slow heating and cooling. Macroscopically, discs quenched from 200°C, 300°C, and 400°C progressively become a lighter shade of pink in reflected light. The comparison with similarly prepared discs not subjected to thermal treatment is most dramatic (Figure 19a). Microscopically and in reflected light, it is obvious that the lighter color results from reflections of light from cracked grain boundaries (Figure 19b, c). In thin section (transmitted light) grain boundary partings and intragranular cracks oriented perpendicular to these boundaries are evident (Figure 20). Many of the latter

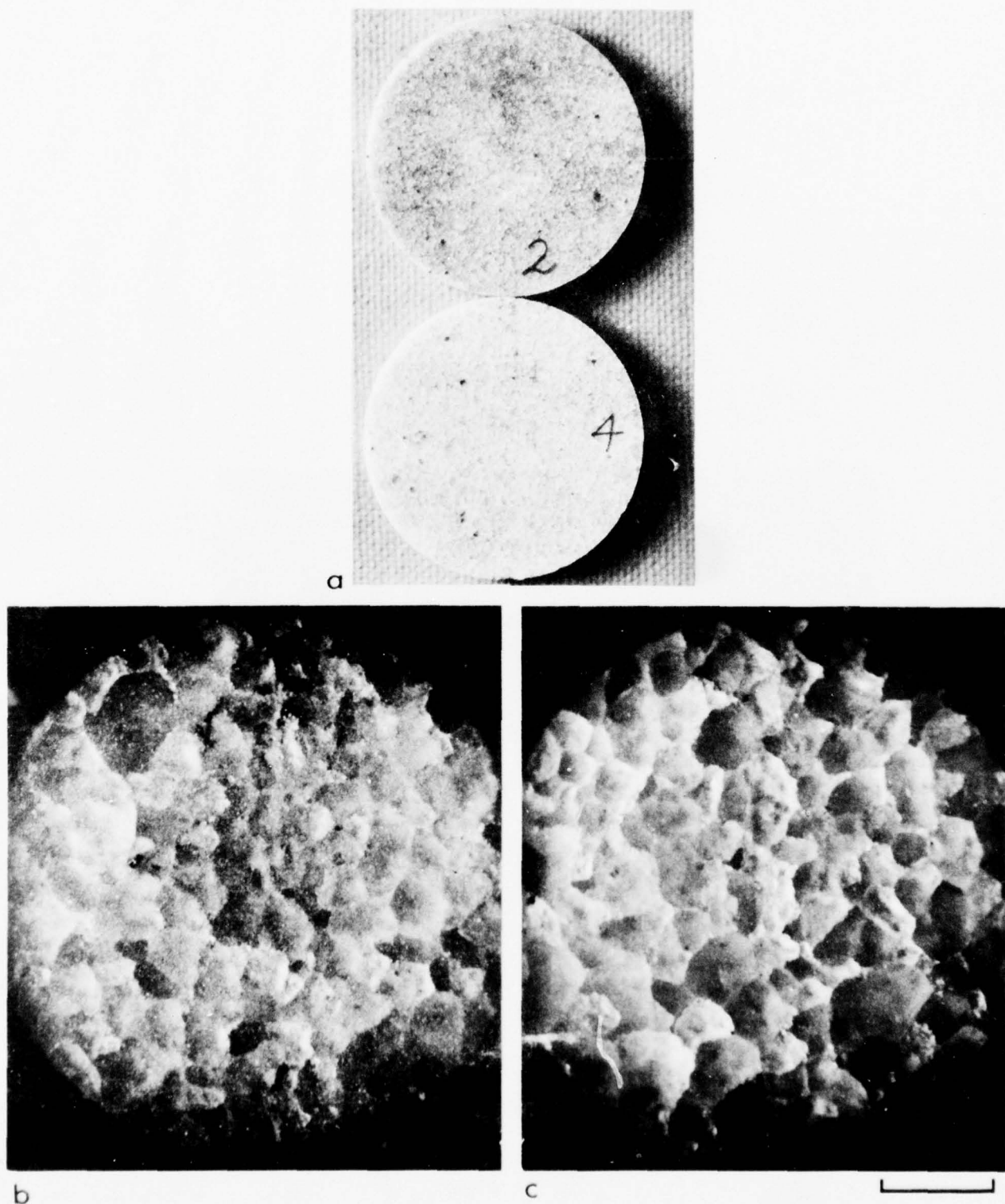


Figure 19. Photographs show in reflected light the influence of thermal treatment. (a) Disc 2 was not subjected to thermal treatment and disc 4 was quenched from 400°C. Note the more reflective surface of disc 4. Discs are 2.0 cm in diameter. (b and c) Enlarged views before (b) and after (c) thermal quenching from 400°C. Development of grain boundary partings is conspicuous in (c). Scale line is 0.1 cm.

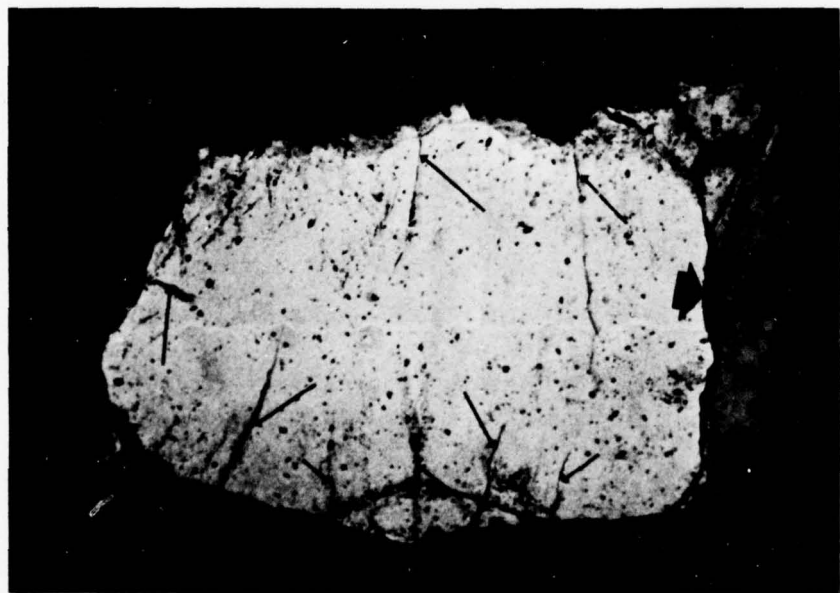


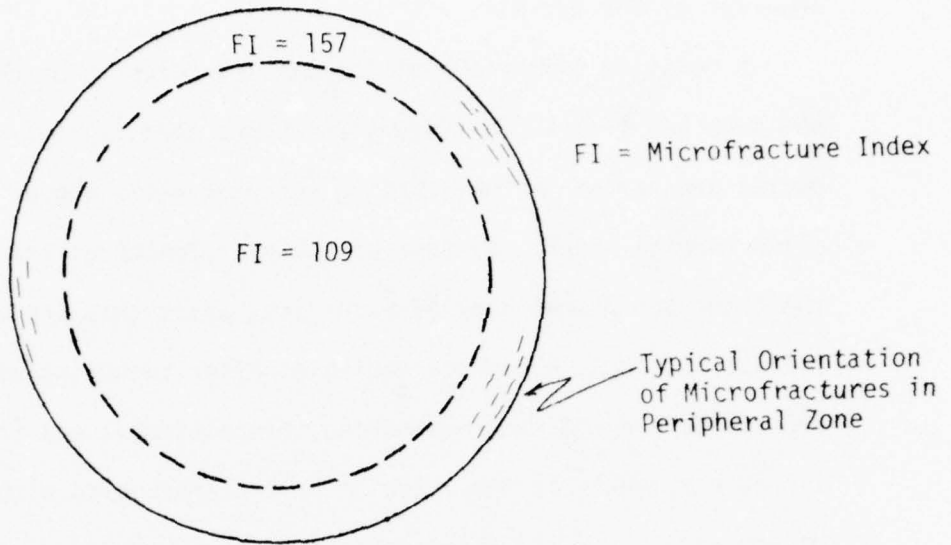
Figure 20. Photomicrograph shows thermally induced grain boundary parting (bold arrow) and intragranular cracks (fine arrows) in Sioux Quartzite quenched from 400°C. Fractures and boundary are stained. Cross polarized light. Scale line is 0.01 cm.

appear to have originated at the grain boundaries and to die out in the interior of the grains.

A detailed comparison of thermal fractures in an untreated disc and one quenched from 400°C (Figure 21) shows that (a) 34% of the grain boundaries are parted in the starting material while 83% of them are parted after thermal shock; (b) most of the microfractures are concentrated in the outer peripheral zone of each disc, where they are oriented tangentially; but their abundance increases after quenching with FI's of 157 and 236 before and after quenching, respectively; and (c) microfractures increase slightly in the interior part of each disc with an FI of 109 before and one of 123 after quenching.

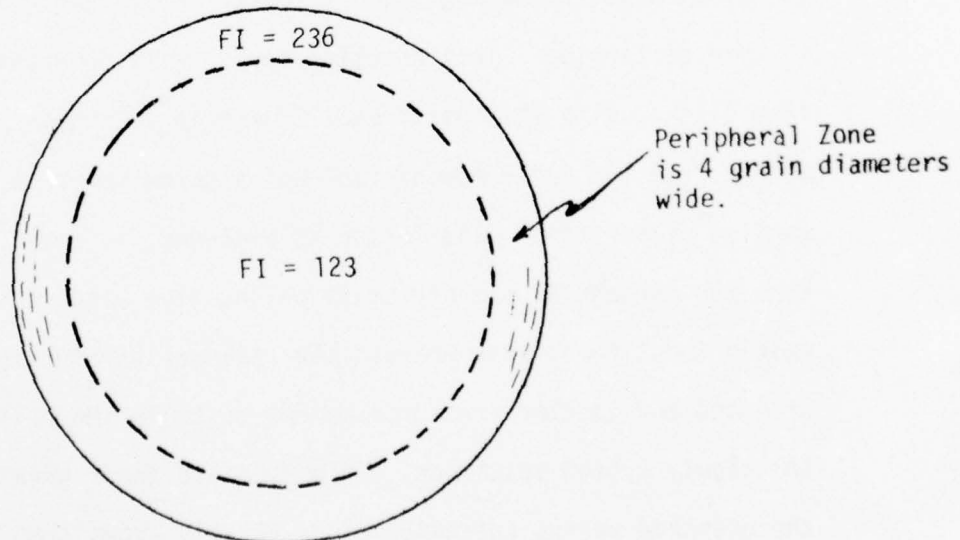
The concentration of most the microfractures in the peripheral zone (four grain diameters wide) both before and after quenching and their tangential orientation (Figure 21) suggest they are produced by more than just the thermal treatment. Many, but not all, are stained with the blue epoxy indicating that at least the stained ones existed prior to thin sectioning. This cracking could arise from the coring process, from discing with the cutoff saw, from thin sectioning (unstained ones), and/or from the influence of residual strains prior to or during thin section preparation. The latter is excluded, at least tentatively, in that the tangential microfracture orientation pattern is axially symmetric about the Y axis whereas the residual strains are not. Similarly oriented and located fractures do not occur in the polished discs of the slowly cycled specimens. This fact and their greater abundance in the quenched versus untreated discs clearly shows that the thermal effects are important, and possibly dominant, in their development.

No. 8: NO THERMAL TREATMENT



34% OF GRAIN BOUNDARIES ARE PARTED

No. 9: THERMALLY SHOCKED - 400° to 24°C



83% OF GRAIN BOUNDARIES ARE PARTED

Figure 21. Documentation of thermal cracking in Sioux Quartzite.

Study of the orientation of the most conspicuously parted grain boundaries in the 400°C-quenched specimen indicates they too are tangentially oriented (Figure 22). Their orientation pattern also is axially symmetric about Y and for the reasons expressed above probably they also are not related to the residual strains. The boundaries measured occur in the interior parts of the disc, are all stained with blue epoxy, and appear to be caused primarily by the thermal treatment.

A detailed study of the crystallographic orientation of grains on either side of conspicuously parted grain-boundaries was made to gain insight into factors that might control the grain-boundary deformation upon thermal shock. For example, one might expect anisotropic thermal expansion in neighboring grains to induce deformation at the boundary. Differential expansion or contraction parallel to the grain boundary would be greatest if the c-axes of the adjacent grains were oriented at 90° rather than 0° to each other. The frequency distribution of 100 angles between c-axes of grains on either side of 100 conspicuously parted boundaries in the specimen quenched from 400°C is random (Figure 23). Thus, this analysis does not reveal any "cause and effect" relation.

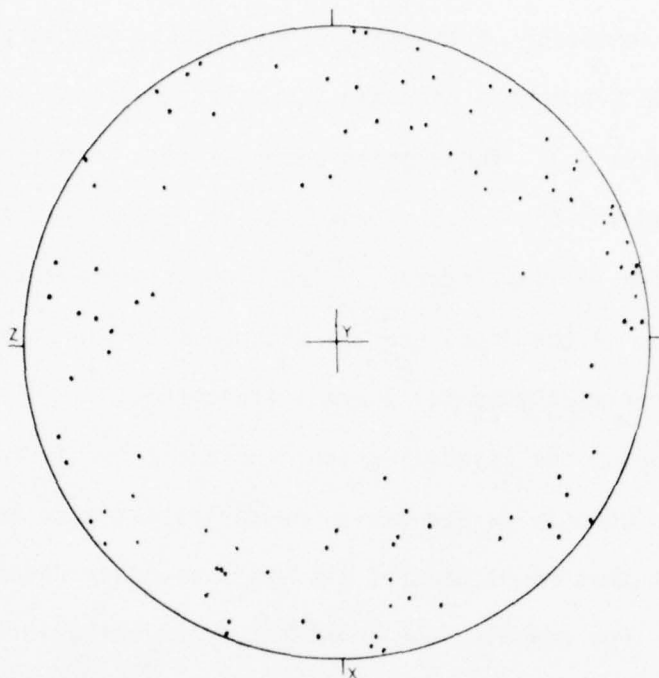


Figure 22. Diagram shows normals to 100 conspicuously parted grain boundaries in a disc of Sioux Quartzite quenched from 400°C. Plane of the diagram is parallel to the circular section of the disc with X, Y, and Z as indicated. Sedimentary bedding is parallel to XY. Data are plotted in lower hemisphere, equal-area projection.

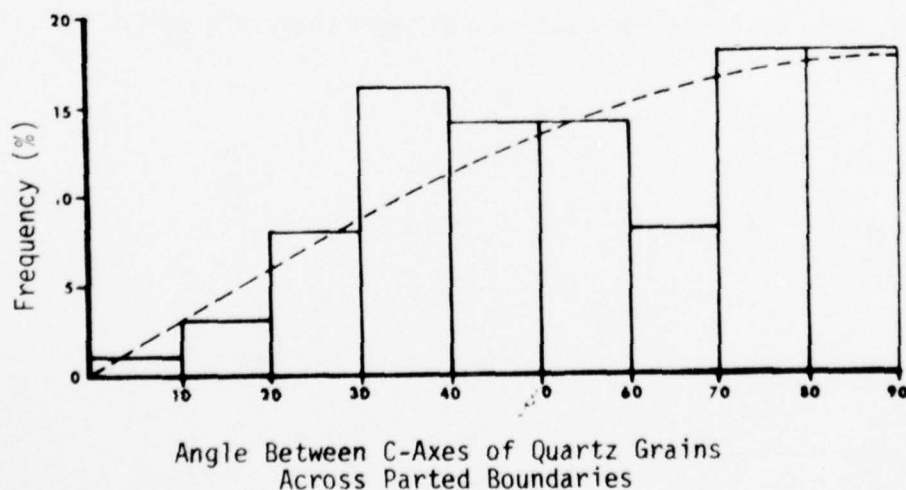


Figure 23. Histogram shows the frequency distribution of the angle between the c-axes of pairs of quartz grains across 100 conspicuously parted grain boundaries in a specimen of Sioux Quartzite thermally quenched from 400°C. Dashed line indicates the expected random distribution of such data (Bloss, 1957).

## DISCUSSION

Changes of longitudinal-wave velocity, porosity, and  $Q$  together with petrofabric observations demonstrate unequivocally that significant thermal cracking occurs during slow thermal cycling of Sioux Quartzite. This data alone, however, does not allow us to specify when during the thermal cycle the cracking occurs. Unfortunately, neither does the acoustic emission data, because of the lack of meaningful records during the entirety of the cooling phase. However, pronounced acoustic emission during heating together with its absence during the first one hundred degrees of cooling suggests cracking takes place primarily during the heating phase. Better evidence for the preponderance of thermal cracking during the heating phase is provided by a comparison between post-heating values of Young's modulus with values of Young's modulus determined at temperature.

Figure 24 compares values of Young's modulus of Sioux Quartzite measured at temperature by Wingquist (1969) (open triangles and associated error bar) with our room temperature values of Young's modulus of thermally-cycled samples (solid squares). Both sets of data are normalized with respect to the initial pre-heating value of Young's modulus as determined for room-dry samples. Aside from the initial pre-heating values, all values of Young's modulus for both sets of data are for fully dry samples. The comparison of the two sets of data in Figure 24, does not take into account that Wingquist's measurements at temperature reflect both the irreversible and reversible effects of temperature, whereas the post-cycling values reflect only the irreversible effects. For temperatures less than 500°C, both a Ruess-Voigt-Hill (RVH) averaging of single-crystal

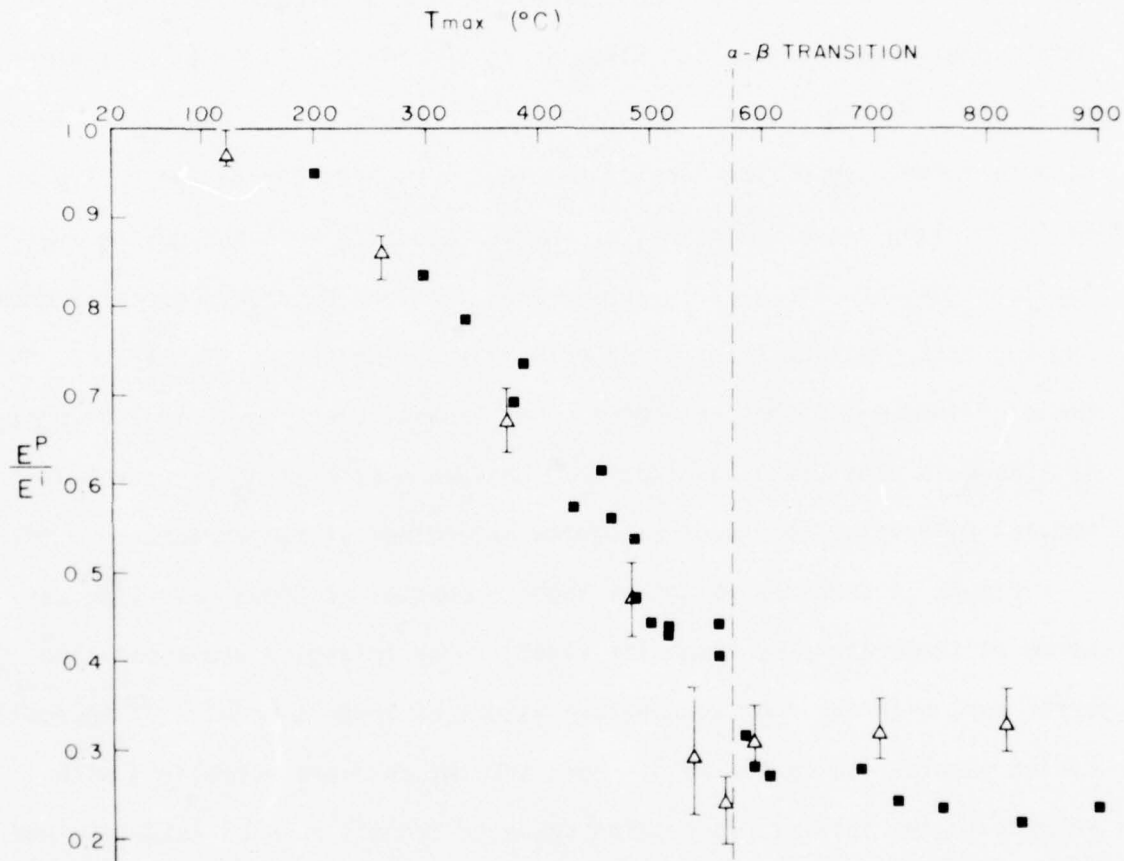


Figure 24. Young's modulus of Sioux Quartzite measured at temperature (open triangles) and after thermal cycling to temperature  $T_{\max}$  (solid squares). Young's modulus,  $E^P$ , at temperature or after thermal cycling is normalized with respect to the pre-heating value,  $E^i$ . Young's modulus at temperature reflects reversible and irreversible effects of temperature, whereas the post-cycling values reflect only the irreversible effects. Correction for the reversible effects of temperature are discussed in text. Young's modulus data at temperature is from Wingquist (1969).

data for quartz and measurements of Ide (1937) on a quartzose sandstone (80% quartz) indicate that Young's modulus decreases reversibly approximately 2% for every 100°C increase in temperature. Between 500°C and the  $\alpha$ - $\beta$  transition, the rate of decrease is significantly larger (see Figure 27). At the  $\alpha$ - $\beta$  transition, Young's modulus (RVH average) abruptly increases to a value approximately 4% greater than that at 20°C. Applying these corrections to our data brings the two sets of measurements into near coincidence. Such close coincidence is not to be expected if a significant component of thermal cracking occurs during the cooling phase.

There is, however, a potential weak point in the comparison of our post-cycling data with Wingquist's measurements at temperature. The initial pre-heating value of Young's modulus of the Sioux Quartzite samples used by Wingquist is approximately 20% greater than that for our Sioux Quartzite samples (78 GPa vs 62 GPa). The difference in Young's modulus indicates the two sets of samples have different initial microstructures. We do not know, however, in what manner the microstructures differ, but we assume, for the present, that the effects of differing microstructure does not greatly affect the relative degrees of thermal cracking developed in each set of samples. Unfortunately, we cannot be assured that this is the case, because our studies indicate that subtle microstructure differences do affect the degree of thermal cracking developed at a specific temperature, all other things being equal. This is demonstrated by the measurable differences in the threshold temperature and velocity changes of Group I and Group II samples in our study. Grain-size differences appear to be the primary reason for the differences in thermal cracking;

this is consistent with observations of other workers (Clarke, 1964; Davidge and Green, 1968a, b; Perami, 1971; Kuszyk and Bradt, 1973; Richter and Simmons, 1974). In general, the coarser the grain-size, the lower the threshold temperature and the greater the degree of thermal cracking that develops at a specific temperature.

Ide's (1937) measurements of the velocity of rock at elevated temperature during slow thermal cycling also indicate that cooling induces little if any additional structural damage. He observed that the velocity vs temperature curve was essentially the same upon re-heating as it was during the cooling phase of the previous thermal cycle. If significant thermal cracking had occurred it is expected the velocity would be lower upon re-heating. The velocity changes upon re-heating only if the temperature exceeds the maximum temperature attained during previous thermal cycles. Recent experiments (Todd and others, 1972) confirm that no velocity change occurs for samples thermally recycled to temperatures less than or equal to the previous maximum temperature. These observations hold true for the Sioux Quartzite. A sample cycled seven times to 515°C displays the same velocity decrease (within the uncertainty of the measurements) as a sample cycled only once to 515°C.

The intense thermal cracking of Sioux Quartzite upon slow heating is directly attributable to the marked thermal expansion anisotropy of quartz. At room temperature, for example, thermal expansion parallel to the c-axis is approximately half that along the a-axes ( $\lambda_c = 7.0 \times 10^{-6} \text{ }^{\circ}\text{C}^{-1}$  vs  $\lambda_a = 13.2 \times 10^{-6} \text{ }^{\circ}\text{C}^{-1}$ ). In the Sioux Quartzite, neighboring quartz grains typically have differing crystallographic orientations. Consequently, when the temperature of the rock changes there is a propensity

for differential displacements to arise at the boundary between adjoining grains. If holes are not to open in the structure, compatibility of displacements requires a system of self-equilibrating stresses develop within the grains to restrain these differential displacements. In general, the greater the crystallographic mismatch of neighboring grains the greater the intergranular stresses developed. If the intergranular stresses exceed the local strength of the rock, fracture occurs.

Exact calculation of thermally-induced intergranular stresses ( $\sigma$ ) is difficult, but analyses of several simplified cases (e.g., Boas and Honeycombe, 1946; Davidge and Green, 1968a; Devore, 1969) indicate that

$$\sigma \propto (\lambda_a - \lambda_c) \Delta T \frac{E_a E_c}{E_a + E_c} . \quad (4)$$

where  $\Delta T$  is the temperature increment and  $\lambda_a, c$  and  $E_a, c$  are, respectively, the thermal expansion coefficient and Young's modulus parallel to the a and c crystallographic axes. As shown in Figures 25 and 27, the thermal expansion coefficient and Young's modulus are a function of temperature. Of particular importance with respect to Eq. 4, the difference between the thermal expansion along the a and c axes ( $\lambda_a \Delta T - \lambda_c \Delta T$ ) increases with temperature (Figure 26). This differential thermal-expansion strain increases rapidly as temperatures near the  $\alpha$ - $\beta$  transition, with an abrupt increase at the transition point. Notably, at higher temperatures the differential strain continues to increase even though volumetrically, quartz contracts (Figure 25).  $E_a$  and  $E_c$  decrease progressively with increasing temperatures below the  $\alpha$ - $\beta$  transition, with a marked decrease just prior to the transformation point (Figure 27). The transformation

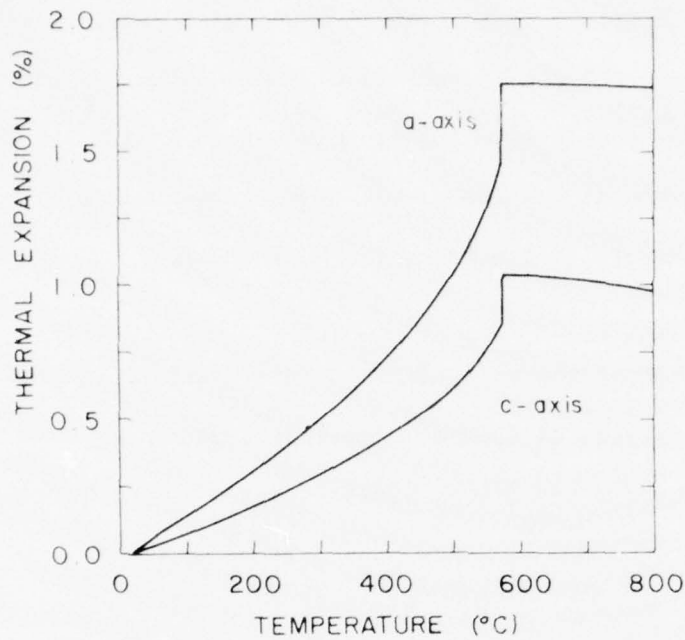


Figure 25. Thermal expansion of quartz parallel to the a and c crystallographic axes. Data from Skinner (1966, p.91).

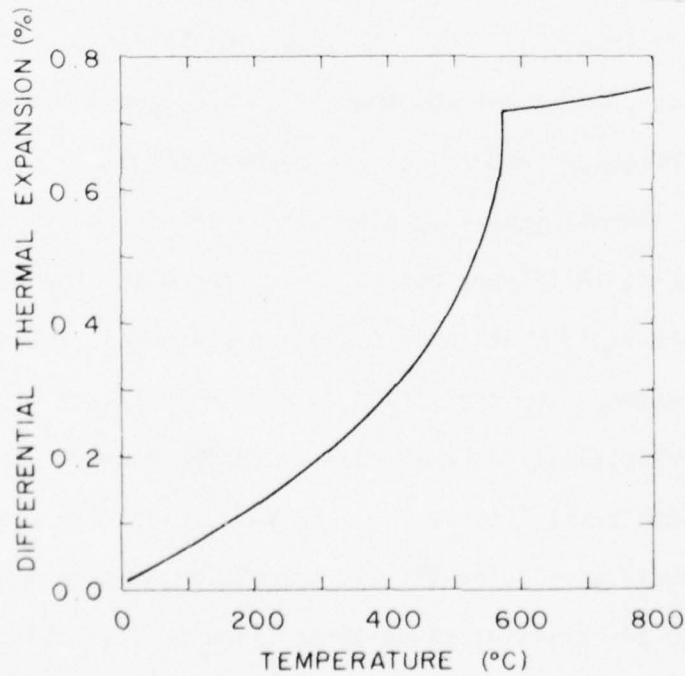


Figure 26. Variation of the differential thermal expansion of quartz parallel to the a and c crystallographic axes as a function of temperature. Data from Skinner (1966, p. 91).

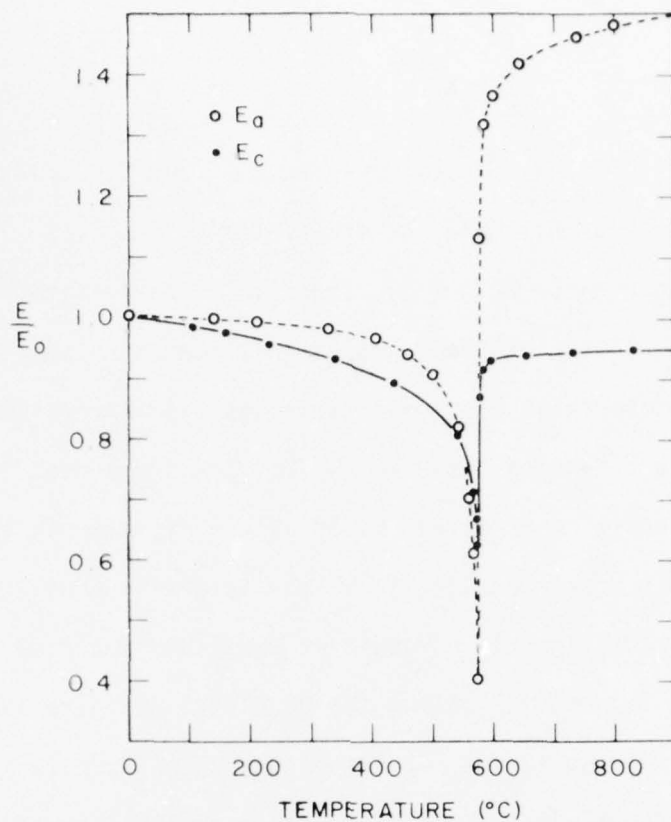


Figure 27. Temperature dependence of Young's modulus parallel to the  $a$  and  $c$  crystallographic axes of quartz. Values of Young's modulus are normalized with respect to room temperature values,  $E_a = 0.78$  GPa and  $E_c = 1.03$  GPa. Data from Perrier and de Mardiot (1922).

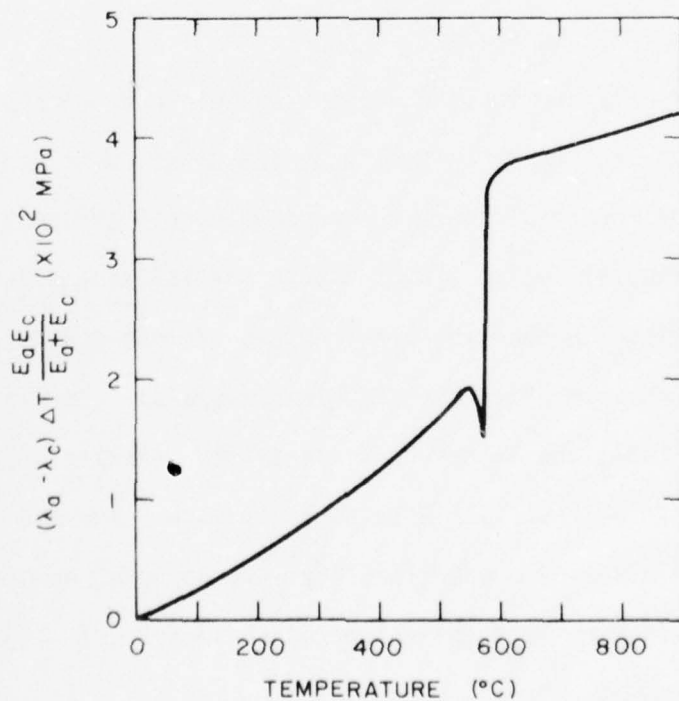


Figure 28. Predicted variation of intergranular thermal stresses with temperature in a polycrystalline aggregate of quartz.

is marked by a significant and abrupt increase in  $E_a$  and  $E_c$ , which continue to increase slowly with increasing temperature.

Using the data in Figures 26 and 27, Equation 4 is evaluated and plotted in Figure 28. This plot shows, as a first approximation, the functional form of the increase of thermal stresses with increasing temperature, assuming fracture does not occur. The plot shows most impressively why the  $\alpha$ - $\beta$  transition is marked by an abrupt increase in cracking. It also indicates why thermal cracking is likely to continue at temperatures above the  $\alpha$ - $\beta$  transition, as a result of continued increase of thermal stresses. It is unknown whether the predicted decrease in thermal stress immediately prior to the  $\alpha$ - $\beta$  transition actually occurs in the case of the Sioux Quartzite. Such a reduction in the thermal stresses is expected to be accompanied by a reduction or cessation of cracking; accordingly, acoustic emission should be minimal in this temperature interval. Sparsity of acoustic emission data in this interval, however, precludes checking this out at present.

Somewhat unexpectedly and for the present unexplained, we observe that the post-heating porosity of thermally-cycled Sioux Quartzite is proportional to the differential thermal-expansion strain of quartz occurring at  $T_{max}$  of the thermal cycle. This proportionality is indicated in Figure 29, which shows superposed log-linear plots of post-heating porosity versus  $T_{max}$  and maximum differential thermal-expansion strain of quartz versus temperature; the latter curve is shifted parallel to the ordinate axis to obtain a "best fit" with porosity data. For the present, we cannot explain the observed proportionality. We do note, however, that a similar proportionality between the volume of an individual

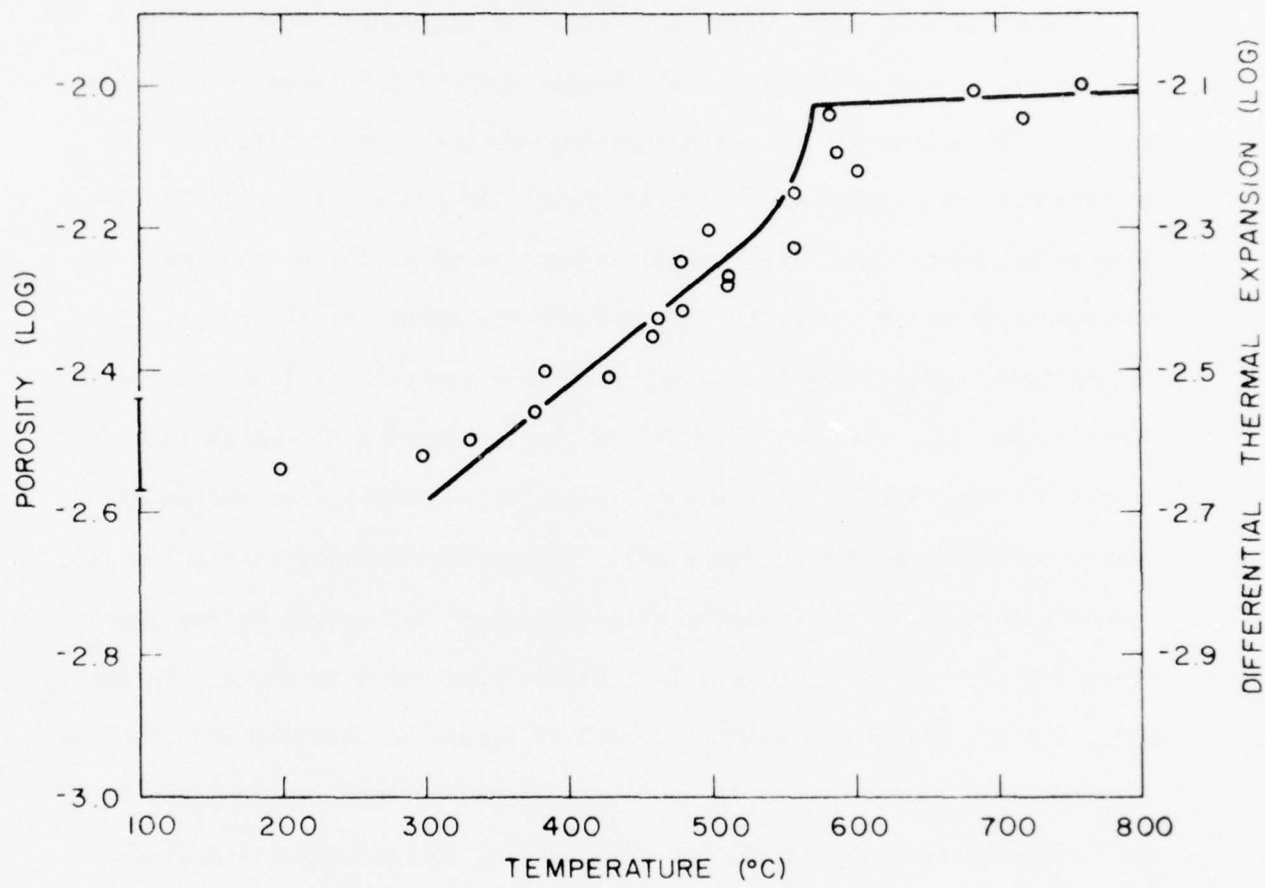


Figure 29. Superposed log-linear plots of post-heating porosity of Sioux Quartzite versus maximum thermal cycle temperature,  $T_{\max}$  (open circles) and of differential thermal expansion of quartz versus temperature (solid curve). The differential thermal expansion versus temperature curve is shifted parallel to the ordinate axis to achieve a "best fit" with the porosity data. The range of initial, pre-heating porosity is indicated by the vertical bar at 100°C.

thermal crack and the differential thermal strain of quartz is not to be unexpected.

A thermally-induced crack is a "hole" in the rock's structure that is a direct result of differential thermal expansion between neighboring grains. The volume of the crack thus depends upon the magnitude of the differential displacements occurring across the crack. Accordingly, the greater the mismatch of the thermal expansions of grains within the immediate vicinity of the crack, the greater the volume of the crack. Assuming this conceptual model is approximately correct, it is not unreasonable that at a specific temperature the volume of a thermally-induced crack is proportional to the maximum differential thermal expansion of quartz occurring at that temperature. The proportionality constant should depend upon the crystallographic orientations of the grains in the immediate vicinity of the crack and thus varies from crack to crack. Furthermore, using a weighed-averaging scheme it should be possible in principle to define for each temperature an "average" proportionality constant between total crack porosity and the differential thermal-expansion strain of quartz at that temperature. If total crack porosity is determined at room temperature, then the proportionality constant must be corrected for the recoverable volume changes occurring upon cooling. There is no immediately obvious reason, however, why the corrected "average" proportionality constant should be independent of temperature as indicated in Figure 29.

Our studies of acoustic emission during heating are restricted to detection of stress waves that have amplitudes greater than  $10^{-7}$  mm and frequency contents between 5 and 300 kHz. Thus we are measuring only a portion of the acoustic emission generated within the rock, but we assume

our sample is representative. Besides the uncertainties associated with detecting only a fraction of the acoustic emission activity, we have no assurance that all emissions detected result from fracture events. Another potential source of acoustic emission is from unstable sliding between surfaces of a brittle material (Hardy, 1971, p. 69). During thermal cycling, differential contractions or expansions may give rise to unstable sliding between touching, detached grains, or crack faces, or both. Since we are primarily interested in fracture events, it is highly desirable to differentiate acoustic emission generated by fracture events from that associated with unstable sliding. The feasibility of making such a distinction, however, has yet to be demonstrated. Ideally, the differing source mechanisms (i.e., fracture vs unstable sliding) may have identifiably different acoustic emission signatures. For the present, we assume that the preponderance of acoustic emission is associated with brittle fracture.

In our experiments, we do not record the actual waveforms of acoustic emission events, hence we do not know the amplitude distribution of the emissions. Consequently, it is not necessarily meaningful at this time to attempt to correlate either the cumulative emission or emission rate data with the velocity data. We do not know, for example, whether or not a high emission rate corresponds to a large increment of structural damage. To make such a correlation, we need the amplitude distribution data.

The acoustic emission data has allowed us to specify precisely the onset of thermal cracking. More importantly, however, we have been able to show that acoustic emission activity is very similar amongst samples subjected to the same thermal conditions. This consistence is essential

if the acoustic emission data is to be amenable to analysis. Clearly, more work is needed and warranted. In particular, the amplitude distribution and frequency spectra of the acoustic emissions must also be analyzed.

### Conclusions

- (1) Thermal cracking of the monomineralic Sioux Quartzite upon slow uniform heating is directly attributable to the marked thermal expansion anisotropy of quartz.
- (2) Thermal cracking occurs only after a critical threshold temperature is exceeded. For the Sioux Quartzite, the threshold temperature for an initial thermal cycle ranges between 200°C and 250°C, depending upon the specific microstructure of the sample.
- (3) Above the threshold temperature, thermal cracking increases progressively with increasing temperature. The majority of cracking occurs prior to the  $\alpha$ -quartz to  $\beta$ -quartz transformation (573°C). A significant component of thermal cracking occurs at the  $\alpha$ - $\beta$  transition and is reflected by an abrupt decrease in the (post-heating) longitudinal-wave velocity, a rapid porosity increase, and intense acoustic emission. Thermal cracking continues above the  $\alpha$ - $\beta$  transition but at a reduced rate.
- (4) The preponderance of thermal cracking occurs during the heating phase of a thermal cycle.
- (5) Thermally-induced cracks develop primarily along grain boundaries and secondarily as intragranular cracks. Typically, intragranular cracks intersect grain boundaries at high angles and tend to die out into the grains.
- (6) The pre-heating residual strain state influences the development of intragranular cracks.

(7) Subtle microstructure differences measurably affect the degree of thermal cracking developed during a thermal cycle. Grain size may be the dominant microstructure parameter.

(8) The observed relationship between longitudinal-wave velocity and porosity indicates that the bulk of the porosity developed below the  $\alpha$ - $\beta$  transition is associated with low aspect-ratio cracks, whereas above the  $\alpha$ - $\beta$  transition, increased porosity is associated primarily with high aspect-ratio cracks.

(9) Acoustic emission has proven to be a valuable source of information and is likely to play an important role in future attempts to understand the details of thermal cracking. Most significantly, the present study has shown that acoustic emission activity is very similar amongst Sioux Quartzite samples subjected to the same thermal conditions.

(10) The quality factor, Q, displays a marked sensitivity to the presence of water. Typically, Q displays a change after a thermal cycle, but when measured at fully-saturated and room-dry conditions it has not proven to be an especially sensitive indicator of microstructure changes. Nevertheless, Q of a fully-saturated rock displays a systematic decrease with increasing thermal cycling temperature and appears to be in accord with Biot's mechanism of attenuation in a fluid-saturated, porous elastic solid. Changes of Q for "room-dry" samples are less systematic, but significantly, Q increases for samples heated above 550°C.

(11) Confining pressure inhibits the development of thermal cracking.

## ACKNOWLEDGEMENTS

We are especially grateful to Dr. Anthony Gangi for his numerous consultations, suggestions, and constructive criticisms that have significantly influenced this research. In addition, Dr. Gangi designed and constructed the acoustic emission monitoring system and directed set-up of the velocity measuring system. For their help in various phases of this research, we wish to thank Stephen Bauer, Virginia Clark, Beatrice Johnston, and Tzuhua Yen.

## REFERENCES

Baldridge, W. S. and Simmons, G., 1971, Progress in microcrack decoration (Abstract): *Trans. Am. Geophys. Union*, v. 52, p. 342.

Bancroft, D., 1941, The velocity of longitudinal waves in cylindrical bars: *Phys. Rev.*, v. 59, p. 588-593.

Barbish, A. B. and Gardner, G. H. F., 1969, The effect of heat on some mechanical properties of igneous rocks, *Jour. Soc. Petroleum Engineers*, p. 395-402.

Biot, M. A., 1956, Theory of propagation of elastic waves in a fluid saturated porons solid. 1. low-frequency range. 2. higher frequency range: *J. of Acoust. Soc. Amer.*, v. 28, p. 168-191.

Bloss, D. F., 1957, Anisotropy of fracture in quartz: *Am. Jour. Sci.*, v. 255, p. 214-225.

Boas, W. and Honeycombe, R. W. K., 1946, Plastic deformation of non-cubic metals by heating and cooling: *Proc. Roy. Soc. London, Ser. A*, v. 186, p. 57-71.

Clarke, F. J. P., 1964, Residual strain and the fracture stress-grain size relationship in brittle solids: *Acta Metallurgica*, v. 12, p. 139-143.

Coppola, J. A. and Bradt, R. C., 1973, Thermal-shock damage in SiC: *Jour. Am. Ceramic Soc.*, v. 56, p. 214-218.

Davidge, R. W. and Tappin, G., 1968a, Internal strain energy and the strength of brittle materials: *J. Mater. Sci.*, v. 3, p. 297-301.

Davidge, R. W. and Tappin, G., 1968b, Strength of two-phase ceramic/glass material: *J. Mater. Sci.*, v. 3, p. 629-634.

Davis, W. R., 1968, Measurement of the elastic constants of ceramics by resonant frequency methods: *Brit. Ceram. Soc. Trans.*, v. 67, p. 515-541.

Devore, G. W., 1969, Differential thermal contractions and compressibilities as a cause for mineral fracturing and annealing: *Contributions to Geology, Univ. of Wyoming*, v. 8, no. 1, p. 21-36.

Friedman, M., 1963, Petrofabric analysis of experimentally deformed calcite-cemented sandstones: *J. Geol.*, v. 71, p. 12-37.

Friedman, M. and Bur, T. R., 1974, Investigation of the relations among residual strain, fabric, fracture, and ultrasonic attenuation and velocity in rocks: *Int. J. Rock Mech. Min. Sci. & Geomech. Abstr.*, v. 11, p. 221-234.

Friedman, M., Handin, J., and Alani, G., 1972, Fracture-surface energy of rocks: *Intern. Jour. Rock Mechanics and Mining Science*, v. 9, p. 757-766.

Gordon, R. B. and Davis, L. A., 1968, Velocity and attenuation of seismic waves in imperfectly elastic rocks, *Jour. Geophys. Res.*, v. 73, p. 3917-3935.

Hardy, H. R., Jr., 1971, Application of acoustic emission techniques to rock mechanics research: Sym. on Acoustic Emission, Bal Harbour, Florida, ASTM Spec. Tech. Pub. 505, p. 41-83.

Hasselman, D. P. H., 1969, Unified theory of thermal shock fracture initiation and crack propagation in brittle ceramics: Jour. Am. Ceramic Soc., v. 52, p. 600-604.

Ide, J. M., 1937, Velocity of sound in rocks and glasses as a function of temperature: Jour. Geology, v. 45, p. 689-716.

Kissel, F. N., 1972, Effect of temperature variation on internal friction in rock: Jour. Geophys. Res., v. 77, p. 1420-1423.

Krech, W. W., Henderson, F. A., and Hjelmstad, K. E., 1974, A standard rock suite for rapid excavation research: U.S. Bureau of Mines, RI 7865, 29 p.

Kuszyk, J. A. and Bradt, R. C., 1973, Influence of grain size on effects of thermal expansion anisotropy in  $MgTi_2O_5$ : J. Am. Ceram. Soc., v. 56, no. 8, p. 420-423.

Mar, H. Y. B. and Scott, W. D., 1970, Fracture induced in  $Al_2O_3$  bicrystals by anisotropic thermal expansion: J. Am. Ceram. Soc., v. 53, no. 10, p. 555-558.

Nur, A. and Simmons, G., 1969, The effect of saturation on velocity in low porosity rocks: Earth and Planet. Sci. Lett., v. 7, p. 183-193.

Nur, A. and Simmons, G., 1970, The origin of small cracks in igneous rocks: Int. J. Rock Mech. Min. Sci., v. 7, p. 307-314.

Perami, R., 1971, Formation des microfissures dans les roches sous l'effet de variations homogenes de temperature: Proc. Int. Symp. on Rock Fracture, Nancy, I-6.

Perrier, A. and de Mandrot, B., 1922, Comptes Rendu, v. 175, p. 622 and 1006.

Richter, D. and Simmons, G., 1974, Thermal expansion behavior of igneous rocks: Intern. Jour. Rock Mechanics and Mining Science, v. 11, p. 403-411.

Savanick, G. A. and Johnson, D. I., 1974, Measurements of the strength of grain boundaries in rock: Int. J. Rock Mech. Min. Sci., v. 11, p. 173-180.

Simmons, G. and Cooper, H. W. (in press), Thermal cycling cracks in three igneous rocks.

Simmons, G., Todd, T., and Baldridge, W. Scott, 1975, Toward a quantitative relationship between elastic properties and cracks in low porosity rocks: Am. Jour. Sci., v. 275, p. 318-345.

Skinner, B. J., 1966, Thermal expansion: in Handbook of Physical Constants: Geol. Soc. Am. Mem. 97, p. 75-96.

Somerton, W. H., Mehta, M. M., and Dean, G. W., 1965, Thermal alteration of sandstones: *J. Petroleum Technology*, v. 17, p. 589-593.

Spinner, S. and Tefft, W. E., 1961, A method for determining mechanical resonance frequencies and for calculating elastic moduli from these frequencies: *Proc. ASTM*, v. 61, p. 1221-1238.

Thill, R. E., Willard, R. J., and Bur, T. R., 1969, Correlation of longitudinal velocity variation with rock fabric: *J. Geophys. Res.*, v. 74, no. 20, p. 4897-4909.

Tittmann, B. R. and Honsley, R. M., 1973, High Q (low internal friction) observed in strongly outgassed terrestrial analog of lunar basalt: *Phys. Stat. Solidi (b)*, v. 56, p. k109-k111.

Todd, T., Wang, H., Baldridge, W. S., and Simmons, G., 1972, Elastic properties of Apollo 14 and 15 rocks: *Proc. 3rd Lunar Sci. Conf.*, v. 3, p. 2577-2586.

Tourenq, C., Fourmaintraux, D. and Denis, A., 1971 Propagation des ondes et discontinuities des roches: *Proc. Int. Sym. on Rock Fracture*, Nancy, I-1.

Walsh, J. B. (1966, Seismic wave attenuation in rock due to friction: *Jour. Geophys. Res.*, v. 71, p. 2591-2599.

Walsh, J. B., 1973, Theoretical bounds for thermal expansion, specific heat, and strain energy due to internal stress: *J. Geophys. Res.*, v. 78, no. 32, p. 7637-7646.

Wang, H., Todd, T., Weidner, D., and Simmons, G., 1971 Elastic properties of Apollo 12 rocks: *Proc. 2nd Lunar Sci. Conf.*, v. 3, p. 23-32.

Warren, N., 1973, Brief note on effects of thermal pulses on elastic moduli and Q of rock: *Earth Planet. Sci. Lett.*, v. 20, p. 280-285.

Warren, N., Trice, R., and Stephens, J., 1974, Ultrasonic attenuation: Q measurements on 70215, 29: *Proc. 5th Lunar Conf.*, Supplement 5, *Geochimica et Cosmochimica Acta*, v. 3, p. 2927-2938.

Wingquist, C. F., 1969, Elastic moduli of rock at elevated temperatures: *U.S. Bur. Mines, Report of Investigations*, 7269, 18 p.

## APPENDIX A

# Investigations of the Relations among Residual Strain, Fabric, Fracture and Ultrasonic Attenuation and Velocity in Rocks

M. FRIEDMAN\* and T. R. BUR†

Residual strain measured by X-ray diffractometry, fabric, and ultrasonic velocity and attenuation in blocks of dry Charcoal Granite, Sioux Quartzite, and Berea Sandstone are investigated to determine their causes and effects and the degree to which each can be used to predict fracture anisotropy. The statistical trends of tensile fractures, induced by point-loading oriented discs, are reliably predicted from ultrasonic data in all three rocks; the attenuation data reflect some not sensitive to velocity. In the granite the fractures are compatible geometrically and probably genetically with the orientations and magnitudes of the residual strains (i.e. prestress) and with microfractures and exsolution lamellae. Fractures in the quartzite and sandstone are primarily oriented parallel to bedding. Those not parallel to bedding in the quartzite are compatible with the residual strains. Ultrasonic data for the bedded rocks do not correlate with any of the microscopic fabric elements studied. The tendency for tensile fractures in the sandstone and quartzite to propagate along grain boundaries more so than for the granite suggests minute openings or flaws may exist at the boundaries and these may predominantly influence fracturing and acoustic properties.

## INTRODUCTION

Efficient rapid underground excavation requires the development of geological and geophysical techniques for determining the quality of the rock mass prior to excavation and during excavation by probing immediately ahead of the working face. Ideally the engineer primarily needs to know breaking strengths of the rocks, the abundance and orientation of macroscopic and microscopic defects, rock anisotropies, and the *in situ* state of stress in addition to lithology, ground and water conditions. Work on sonic investigation of rocks by the U.S. Bureau of Mines [1-3] shows that attenuation and velocity fields correlate with, and therefore, can be used to map, at least qualitatively, the rock fabric, fracture anisotropy and unconfined breaking strength in dry rocks. If the sonic method also correlates with the residual and *in situ* states of stress then the possibility exists that sonic probing of the rock mass may yield simultaneously much of the pertinent information required to engineer the rapid underground excavation.

Specifically the relations among the ultrasonic data, residual strains, and fabric are studied in three blocks of

dry rock: Charcoal Granite, Sioux Quartzite, and Berea Sandstone. These are being used because (a) the U.S. Bureau of Mines, Twin Cities Mining Research Center could supply the blocks ( $0.02 \text{ m}^3$ ) and the corresponding ultrasonic data measured in adjacent blocks, (b) the rocks contain quartz from which residual strains can be determined by X-ray diffractometry, and (c) the textures and compositions of these rocks cover much of the spectrum of 'hard' rocks commonly encountered in engineering practice. For each block the residual strains stored in the quartz are measured by X-ray diffractometry [4-7]; the relative tensile fracture strength and the existence of possible fracture anisotropies are determined by point loading of sets of mutually perpendicular discs [6]; and fabric elements that could possibly influence fracture anisotropy or ultrasonic measurements are studied in thin section with universal stage techniques. Directions and planes are defined relative to an *XYZ* coordinate system established parallel to the edges of each block.

## Previous work

Workers at the Twin Cities Laboratory have developed an ultrasonic method for mapping attenuation and velocity fields in rocks, and they have correlated these with rock fabric, fracture anisotropy, and unconfined

\* Center for Tectonophysics, Texas A & M University, College Station, TX 77843, U.S.A.

† Department of Mining, University of Missouri, Rolla, Mo. 65401, U.S.A.

breaking strength [1-3]. Workers at the Center for Tectonophysics have developed an X-ray method for measuring the three-dimensional state of residual strain from locked-in distortions of atomic planes and have demonstrated that the residual strains (prestresses) can influence the orientations of induced fractures and the breaking strengths of rocks under confining pressures to 1500 bars [4-7]. The concepts, techniques and procedures for the ultrasonic and fabric work are reasonably well known. A comprehensive review of residual elastic strain in rocks, particularly as measured by X-ray diffractometry, is given by Friedman [4, 5, 7]. Here it is sufficient to define residual strains (stresses) as potentially recoverable elastic distortions of constituent crystals or grains that satisfy internal equilibrium conditions and that exist in a given volume of rock with no external loads across its boundaries [8, 9].

*Residual and in situ stresses.* The *in situ* state of elastic strain (stress) in rocks consists of two components: the strains caused by currently *applied loads* and the *residual* strains [5 and 7]. If there are no external loads across the boundaries of a rock, as in the laboratory or in special field situations, the potentially recoverable *in situ* strains are the residual strains. These relate to the paleotectonic, paleotopographic, and thermal and chemical histories of the rock. If a rock free of residual strain is currently under loads caused by present topography, present tectonics, or the works of man, then the *in situ* strains are termed applied strains. In the general field or subsurface condition, applied strains and loads are superposed on residual strains and stresses. In this study the ultrasonic data are determined for spheres of rock at atmospheric pressure; hence it is only the residual strains that are important here.

*Residual strains and ultrasonic data.* At least a geometric if not a genetic correlation between residual strains, fabric, and ultrasonic data has been demonstrated for Barre Granite [7]. Ultrasonic velocity and attenuation data were published by Bur *et al.* [2] and the corresponding fabric data by Willard and McWilliams [3]. Residual strains were determined by means of X-ray method from two oriented discs from the same block of the granite as utilized by the above workers. The X-ray data indicate the residual strains are homogeneously distributed in the rock at least over the scale of the two discs (5 cm dia  $\times$  1 cm thick). The average magnitudes of the principal strains equate to a large differential stress ( $\sigma_1 - \sigma_3$ ) of about 340 bars. The orientations of the principal strain axes are each within 20° of the principal axes of the fields of relative amplitude and velocity determined by ultrasonic measurements. Moreover, the greatest, intermediate, and least principal elongations of the state of residual strain correlate with the low (*L*), and medium (*M*), and high (*H*) axes of the ultrasonic symmetry fields. In addition, the 'rift' of the rocks parallels the *H M* symmetry plane which corresponds to the plane containing the least and intermediate principal elongations of the state of residual strain; and the tensile breaking strength is minimal parallel to *L* and the greatest principal elongation [3]. The directions of the 'rift'

and minimum tensile strength agree with predictions from knowledge of the prestrain [6]. Excellent agreement thus exists between the X-ray, ultrasonic, and strength testing data for the Barre Granite.

## OBSERVATIONAL RESULTS

### Charcoal granite

*Composition.* The Charcoal Granite, St. Cloud, Minnesota (also known as the St. Cloud Gray Granodiorite), is a massive, dark brown to dark gray granodiorite consisting of 38% plagioclase feldspar, 26% orthoclase, 21% quartz, 12% hornblende, and 3% biotite. The feldspars are somewhat altered and contain abundant exsolution lamellae. Healed microfractures are conspicuous in the quartz and feldspar. Grain size range is from  $<0.1$  to 10 mm and averages about 1 mm. No conspicuous macrofractures occur at the surfaces of the block.

*Residual strain.* The two polished surfaces required for the X-ray study of the residual strains in the quartz of the rock were prepared from a 5-cm dia core taken from the *YZ* surface. The six sets of principal strain axes that result from the analysis [4] are tightly grouped in space (Fig. 1a) indicating the strains in the quartz are statistically homogeneous. The strains are small with the greatest principal elongation equal to  $20 \times 10^{-6}$  (extensions are positive), and the intermediate and least elongations equal to  $-35 \times 10^{-6}$  and  $-65 \times 10^{-6}$ , respectively.

*Fracture anisotropy.* Three mutually perpendicular sets of oriented discs (2.54 cm dia  $\times$  1.4 cm thick) were prepared for point-loading tests designed to detect fracture anisotropy and relative tensile strength anisotropy [6]. Each disc is loaded, unconfined, between opposed ball bearings until it fails by the development of one or more tensile fractures. The loads are applied at uncontrolled, but not widely varying, rates with a Blackhawk ram; the load at failure ( $\pm 5$  psi) is recorded on a Heise gauge equipped with stop valve. After each set of oriented discs is loaded to failure the azimuths of the induced tensile fractures are measured along the radius of each disc relative to the coordinate axes. The azimuth of diametral fractures is measured separately along each opposing radius, and if the azimuths differ by 5° or more two fractures are counted. A plot of fracture azimuths for each set of similarly oriented discs (Figs. 1b, c, and d) provides a measure of the fracture anisotropy. Data for the discs of Charcoal Granite are listed in Table 1. No significant strength anisotropy exists for the three directions of point-loading. The orientations of the induced tensile fractures (their azimuths relative to coordinates in the plane of each disc) are widely divergent in all three sets of discs, but there are statistically significant groupings of fractures in two sets of discs. Both indicate a strong tendency to fracture essentially parallel to the *XY* plane.

*Fabric.* Planar fabric elements are studied that might be considered mechanical defects in the rock, and therefore, capable of influencing fracture or the ultrasonic data [11]. These include long grain boundaries of felds-

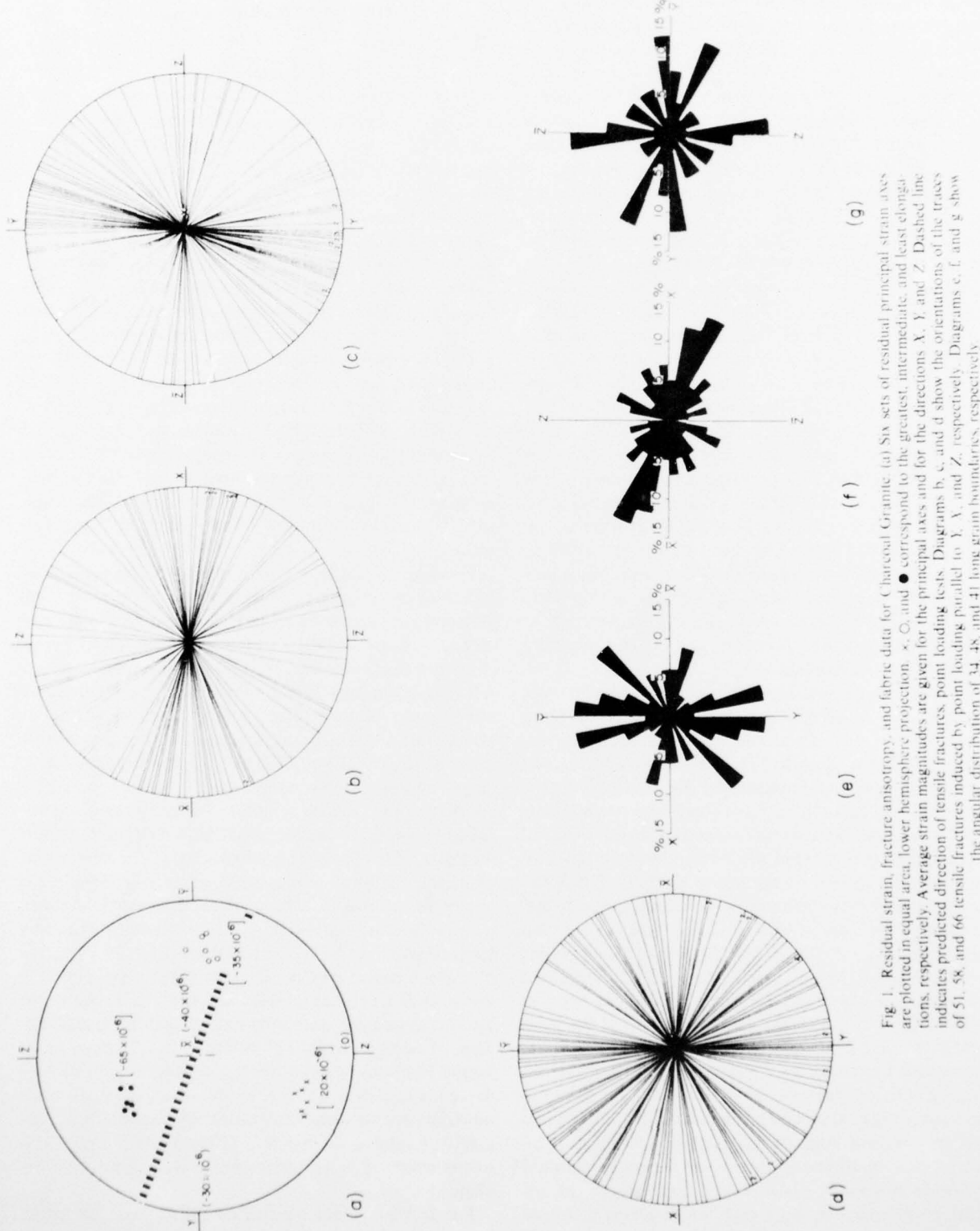


Fig. 1. Residual strain, fracture anisotropy, and fabric data for Charente Granite: (a) Six sets of residual principal strain axes are plotted in equal area, lower hemisphere projection.  $\times$ ,  $\circ$ , and  $\bullet$  correspond to the greatest, intermediate, and least elongations, respectively. Average strain magnitudes are given for the principal axes and for the directions  $X$ ,  $Y$ , and  $Z$ . Dashed line indicates predicted direction of tensile fractures, point load test data. Diagrams b, c, and d show the orientations of the traces of 51, 58, and 66 tensile fractures induced by point loading parallel to  $Y$ ,  $X$ , and  $Z$ , respectively. Diagrams e, f, and g show the angular distribution of 34, 48, and 41 long grain boundaries, respectively.

TABLE I. RESULTS OF POINT LOADING TESTS

Point load parallel to:	No. of discs	Total no. of induced tensile fractures	Mean breaking* strength (bars)	S.D. of breaking strengths (bars)	Preferred orientation of induced tensile fractures
Charcoal Granite					
X	28	58	295	36	yes† (   to XY plane) $\chi^2 = 51$
Y	25	51	275	34	yes (   to XY plane) $\chi^2 = 36$
Z	27	66	310	34	no (random) $\chi^2 = 12$
Sioux Quartzite					
X	30	66	455	47	yes (   to XY and XZ) $\chi^2 = 105$
Y	30	66	480	45	yes (   to XY and XZ) $\chi^2 = 69$
Z	30	80	500	28	yes‡ (sub    to YZ) $\chi^2 = 18$
Berea Sandstone					
X	30	40	53	7.6	yes (   to XY plane) $\chi^2 = 200$
Y	30	36	54	7.0	yes (   to XY plane) $\chi^2 = 175$
Z	30	66	79(82)§	8.3(9.4)	yes (   to XZ plane) $\chi^2 = 69$

\* Calculated using Reichmuth's formula (see McWilliams [10]).

† Based upon  $\chi^2$  'goodness of fit' test of the azimuths of induced tensile fractures as compared to a uniform distribution of azimuths, (e.g. see Fig. 1b, c, d).

‡ Fracture trace diagram (Fig. 4b) shows considerable scatter, but a significant grouping 20° to XY plane. Overall  $\chi^2$  value does not indicate this grouping is significant.

§ A second set of 30 discs were tested to check on reproducibility of tendency for fractures to form parallel to XZ plane.

parts, (0001) cleavages of biotite crystals, healed microfractures primarily in quartz and feldspar, exsolution lamellae and (010) cleavages in the feldspars, and albite and microcline twin lamellae.

The azimuths of the traces of long grain boundaries are somewhat preferentially oriented in each of the three mutually perpendicular thin sections cut from the block (Figs. 1e, f, and g). The orientation is strongest in the thin section parallel to the XZ plane (Fig. 1f) where the grain boundaries are subparallel to the XY plane. There is a fair degree of correlation between the orientations of the long grain boundaries and those of the induced tensile fractures (compare Fig. 1b and f, c and g, d and e).

Biotite cleavages are randomly oriented (Fig. 2a), as are the (010) cleavage planes of the feldspars, and the feldspar twin lamellae (Figs. 2b-d). Microfractures and exsolution lamellae, on the other hand, are preferentially concentrated subparallel to the XY plane (Figs. 2b and c). These elements are randomly oriented in the thin section parallel to the XY plane (Fig. 2d). Thus the orientation trends of the microfractures and exsolution lamellae follow those of the induced tensile fractures.

*Transgranular-intergranular fracture.* Twenty-two tensile fractures (13 cm long) formed in the point loading of 10 discs are studied in thin section to determine the path of the fracture through the rock. For each fracture the distance increments within grains (transgranular) and along grain boundaries (intergranular) are measured in a thin section cut perpendicular to the fracture

surface. Willard and McWilliams [11] found that the transgranular/intergranular ratio, (T/I), weighted for the abundance of the constituent minerals, is inversely proportional to loading rate Charcoal Granite. Unweighted T/I ratios for the 22 fractures studied here range from 1.7 to 24 and average 5.88. Thus fracturing within grains is almost six times more frequent than along grain boundaries. It follows that fabric elements internal to the grains rather than the grain boundaries are more apt to control fracture orientation in this rock.

*Ultrasonic data.* The average velocity and attenuation fields, determine from four to five spheres [2], are shown in Fig. 3. For the Charcoal Granite the velocity field (Fig. 3a) is nearly axially symmetric about the Z coordinate axis, the axis of minimum velocity (between 4.7 and 4.8 km/sec). Velocities parallel to the XY plane are nearly the same (5.05 to 5.10 km/sec) with a maximum subparallel to Y. The average velocity is well below that of a relatively unfractured granodiorite. Thus the rock can be expected to have abundant microfractures. The velocity pattern suggests a strong set of microfractures perpendicular to the Z axis with a possible weak system perpendicular to the X axis.

Attenuation symmetry is similar to the velocity symmetry. The former also suggests a strong set of microfractures nearly perpendicular to the Z axis. The good signal in the Y direction and poor signal in the X direction suggest a second set of microfractures (or similar defects) with poles in the X direction and planes parallel to the Y axis.

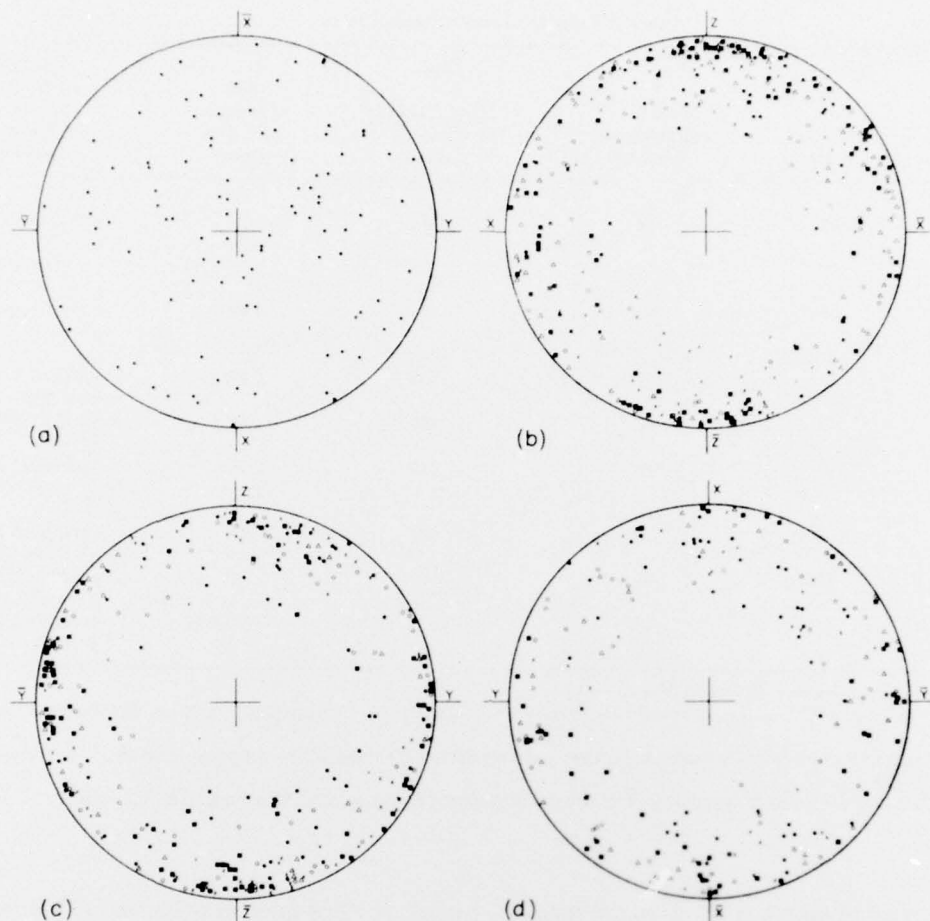


Fig. 2. Diagrams show orientation of planar fabric elements in Charcoal Granite. Data are plotted in lower hemisphere, equal area projection. (a) Composite diagram of normals to (0001) cleavages in 100 biotite crystals measured in three mutually perpendicular thin sections. Partial diagrams (b, c, and d) show the orientations of normals to microfractures ■, feldspar exsolution lamellae X, feldspar (010) cleavages Δ, feldspar albite twin lamellae ●, and microcline twin lamellae ○ as measured in thin section cut parallel to the XZ, YZ, and XY planes respectively. In (b) the number of data points are 98 ■, 82 X, 64 Δ, and 53 ●, and 36 ○. In (c) the corresponding numbers are 87, 65, 30, 66, and 55, and in (d) there are 50, 30, 29, 50, and 44 data points, respectively.

#### *Sioux Quartzite*

**Description.** The block of low porosity, pinkish Sioux Quartzite ( $26.3 \times 28.5 \times 23.0$  cm) exhibits conspicuous bedding oriented parallel to the XY surface (Fig. 1). The upper half of the block is cross-bedded, and two macrofractures occur parallel to bedding and about 5 cm apart in the lower half. The block has not lost cohesion across these fractures.

**Residual strain.** The X-ray measurements were made on specimens from a 5 cm core taken from the center of the XY surface. Principal axes calculated from the diffraction data are strongly grouped (Fig. 4a) suggesting the observed residual strains are reasonably homogeneous with the areas sampled. The observed state of residual strain is characterized by the greatest elongation (average of  $100 \times 10^{-6}$ ) oriented subparallel to X, the intermediate principal axis ( $5 \times 10^{-6}$ ) subparallel to Y, and the least elongation ( $-85 \times 10^{-6}$ , a compressive strain), subparallel to Z. Thus the principal axes of the residual strains as measured by X-rays are nearly coincident with X, Y, and Z.

**Fracture anisotropy.** Point-loading tests on three mutually perpendicular sets of quartzite discs indicate that the induced tensile fractures tend to form nearly parallel to the XY, XZ, and YZ planes (Figs. 4b, c, and d, and Table 1). In spite of this strong fracture anisotropy the differences in corresponding average tensile strengths are small and are not statistically significant (Table 1). The strongest anisotropy is parallel to XY, the bedding plane, next that subparallel XZ, and least that subparallel to YZ.

**Fabric.** The apparent long axes of elongated grains, long grain boundaries, crystallographic c-axes, and defects within the grains—namely microfractures and deformation lamellae were investigated.

In the Sioux Quartzite the apparent long axes of grains with apparent long to short axial ratios  $> 2.0$  are essentially parallel to the long grain boundaries. The orientation of these long axes, as viewed in thin section, are statistically parallel to bedding (Figs. 4e and f) and the ZY plane (Fig. 4g). The long axes and boundaries thus parallel two of the three directions of preferred tensile fracture (Figs. 4b, c, and d).

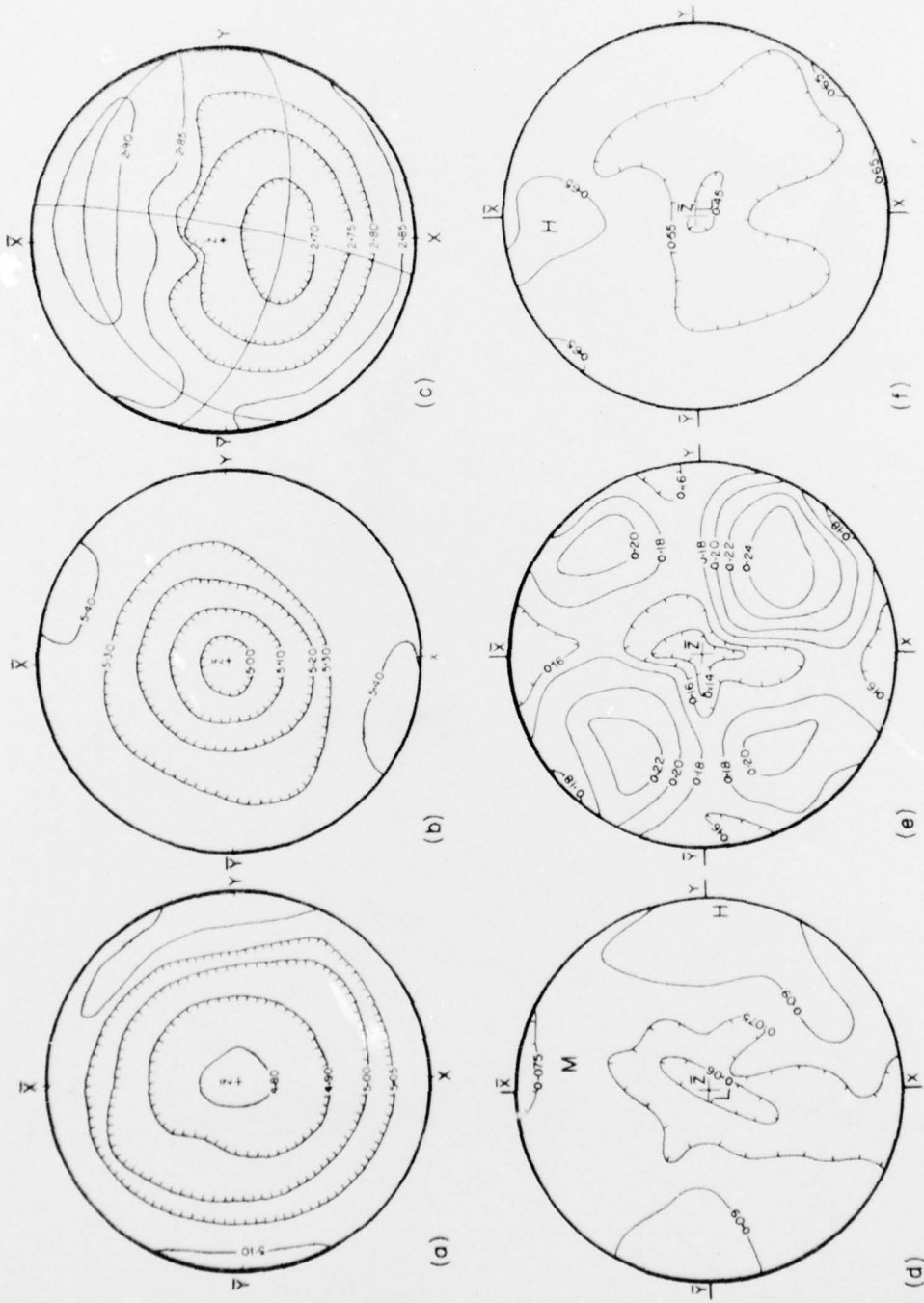


Fig. 3. Ultrasonic data for Charcoal Granite (a,d), Sioux Quartzite (b,e) and Berea Sandstone (c,f) supplied by staff of the U.S. Bureau of Mines, Twin Cities Mining Research Center. All data are plotted in equal area, lower hemisphere projection. Average velocities in km/sec are plotted in a-c; relative amplitudes, the inverse of attenuation, are plotted in d-f.

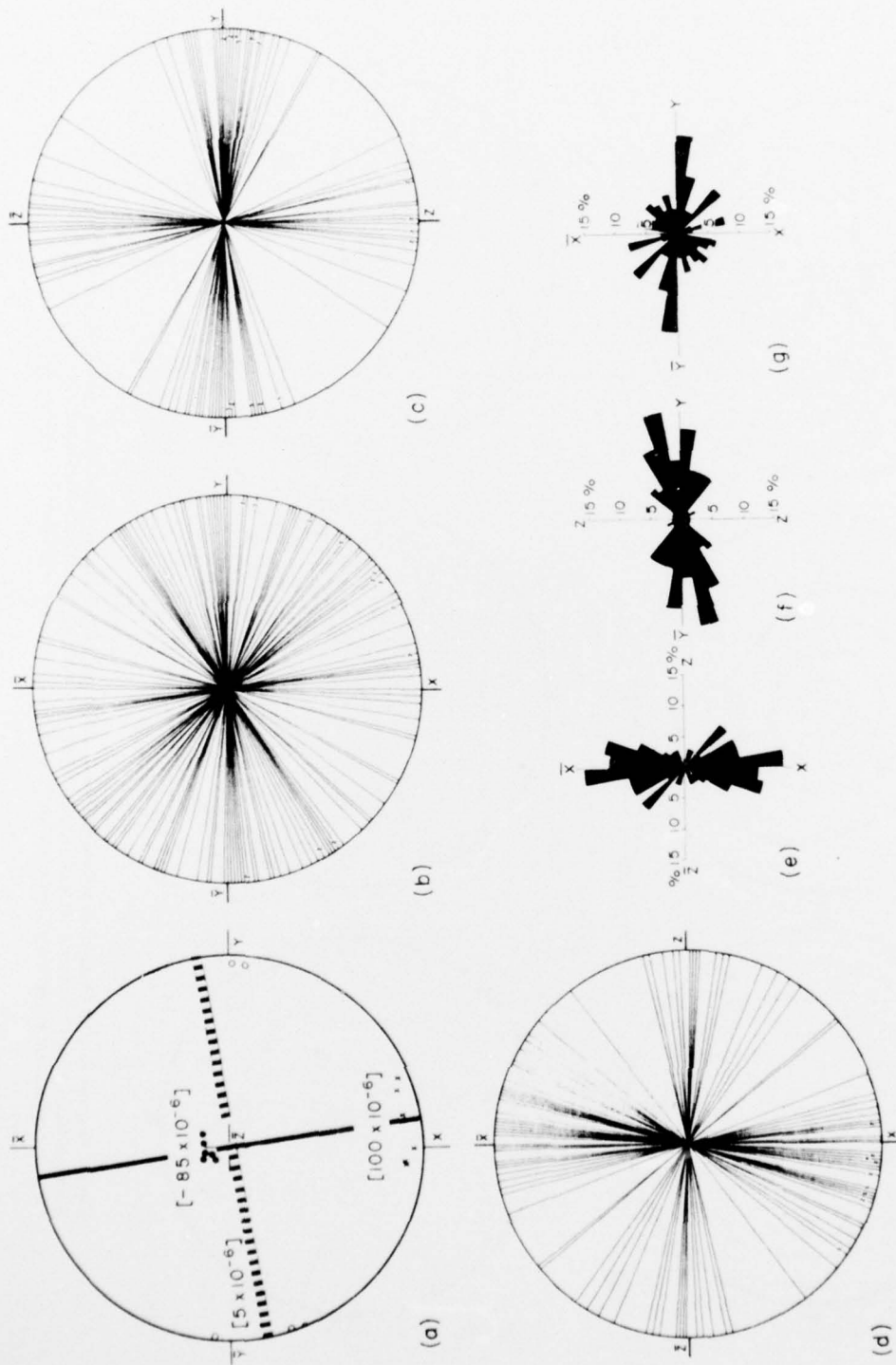


Fig. 4. Residual strain, fracture anisotropy, and fabric data for Sioux Quartzite. (a) Six sets of residual principal strain axes are plotted in equal area, lower hemisphere projection.  $\times$ ,  $\circ$ , and  $\bullet$  correspond to the greatest, intermediate, and least elongations, respectively. Average strain magnitudes are given for the principal axes. Dashed line indicates predicted trend of tensile fractures when discs are point loaded parallel to  $X$ . Solid line is the predicted trend when point loaded parallel to  $Z$ . Diagrams b, c, and d show the orientations of the traces of 80, 66, and 66 tensile fractures induced by point loading parallel to  $Z$ ,  $X$ , and  $Y$ , respectively. Diagrams e, f, and g each show the angular distribution of 75 apparent long grain axes induced by point loading parallel to  $Z$ .

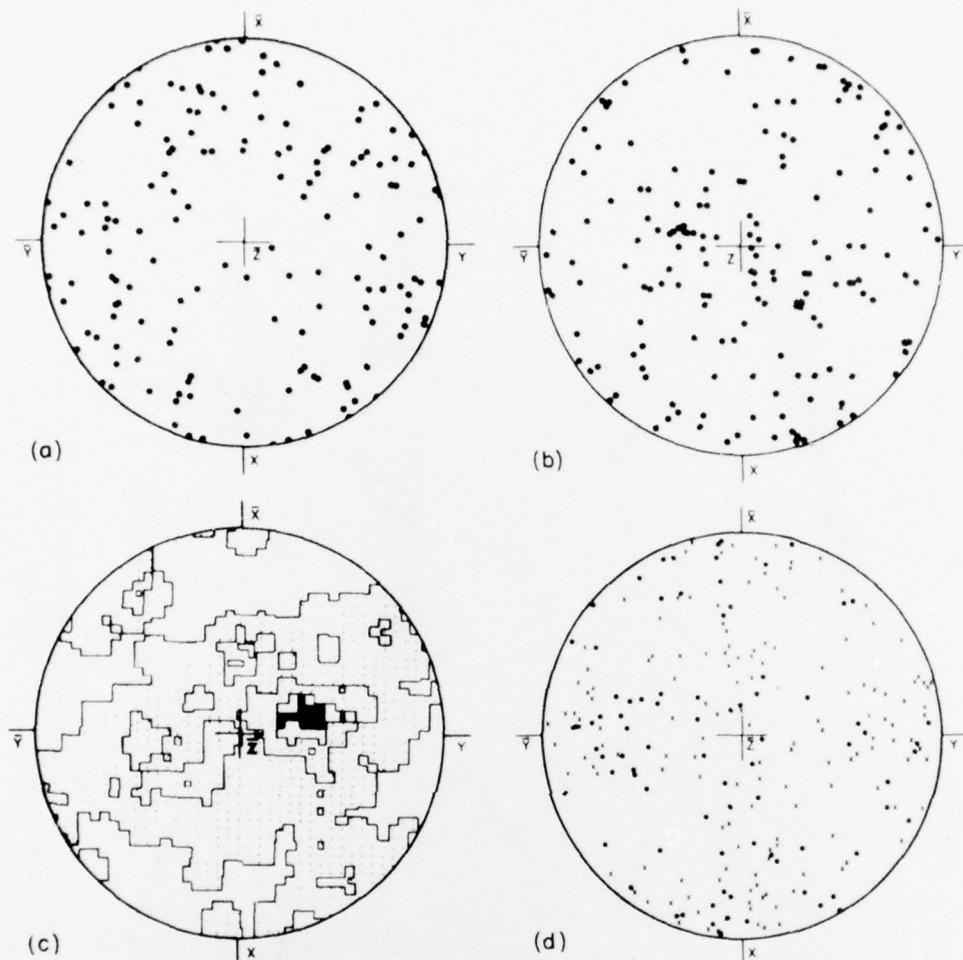


Fig. 5. Fabric data for Sioux Quartzite (a-c) and Berea Sandstone (d). All data are plotted in equal area, lower hemisphere projection. (a) 150 quartz c-axes. (b) Composite diagram of normals to 170 sets of healed microfractures. (c) Composite diagram of normals to 200 sets of quartz deformation lamellae. Contours are at 0.5, 2.5, 4.0, and 5.0 per 1% area, 6% maximum. (d) Orientation of normals to 150 sets of microfractures (X, 2 or more parallel microfractures per set) and 86 sets of quartz deformation lamellae (●).

The *c*-axes of the quartz grains are randomly oriented (Fig. 5a). Thus no anisotropic behavior of the rock can be attributed to a preferred crystallographic orientation of the quartz grains themselves. The grains contain planar defects, however, that could influence the physical behavior of the rock. These are healed microfractures and deformation lamellae. The former are fractures within individual grains along which impurities are concentrated and across which there has been chemical rebonding. No fresh, unhealed microfractures are observed. The microfractures however, are oriented diffusely and no statistically significant concentration of normals to microfractures occurs (Fig. 5b).

Quartz deformation lamellae, known to be planar concentrations of dislocations and impurities, are abundant. These features exhibit a preferred orientation such that they tend to lie at angles  $< 30^\circ$  to the bedding plane, *X*/*Y*, (Fig. 5c). Most of the grains containing deformation lamellae also exhibit undulatory extinction. It is not known to what extent deformation lamellae act as

potential mechanical defects in grains, but it is known that undulose grains are preferentially fractured in experimentally deformed quartz sand aggregates [12] (p. 175).

*Transgranular intergranular fracture.* The *T/I* ratios along eight tensile fractures induced in three quartzite discs by point loading were measured to determine if this ratio would vary with fracture orientation and/or loading direction. *T/I* ratios vary from 1.0 to 2.6 with a tendency for the lower ratios to occur along fractures oriented parallel to bedding (the *X*/*Y* plane). This observation along with the overall smaller ratios as compared with the Charcoal Granite suggest that grain boundaries play a larger role in the fracture of the quartzite than they do for the granite.

*Ultrasonic data.* The average ultrasonic velocity field for the Sioux Quartzite has orthorhombic symmetry with the minimum velocity (4.9–5.0 km/sec) parallel to *Z*, the intermediate velocity 20–30° clockwise from *Y* in the *X*/*Y* plane, and the axis of greatest velocity (>5.4

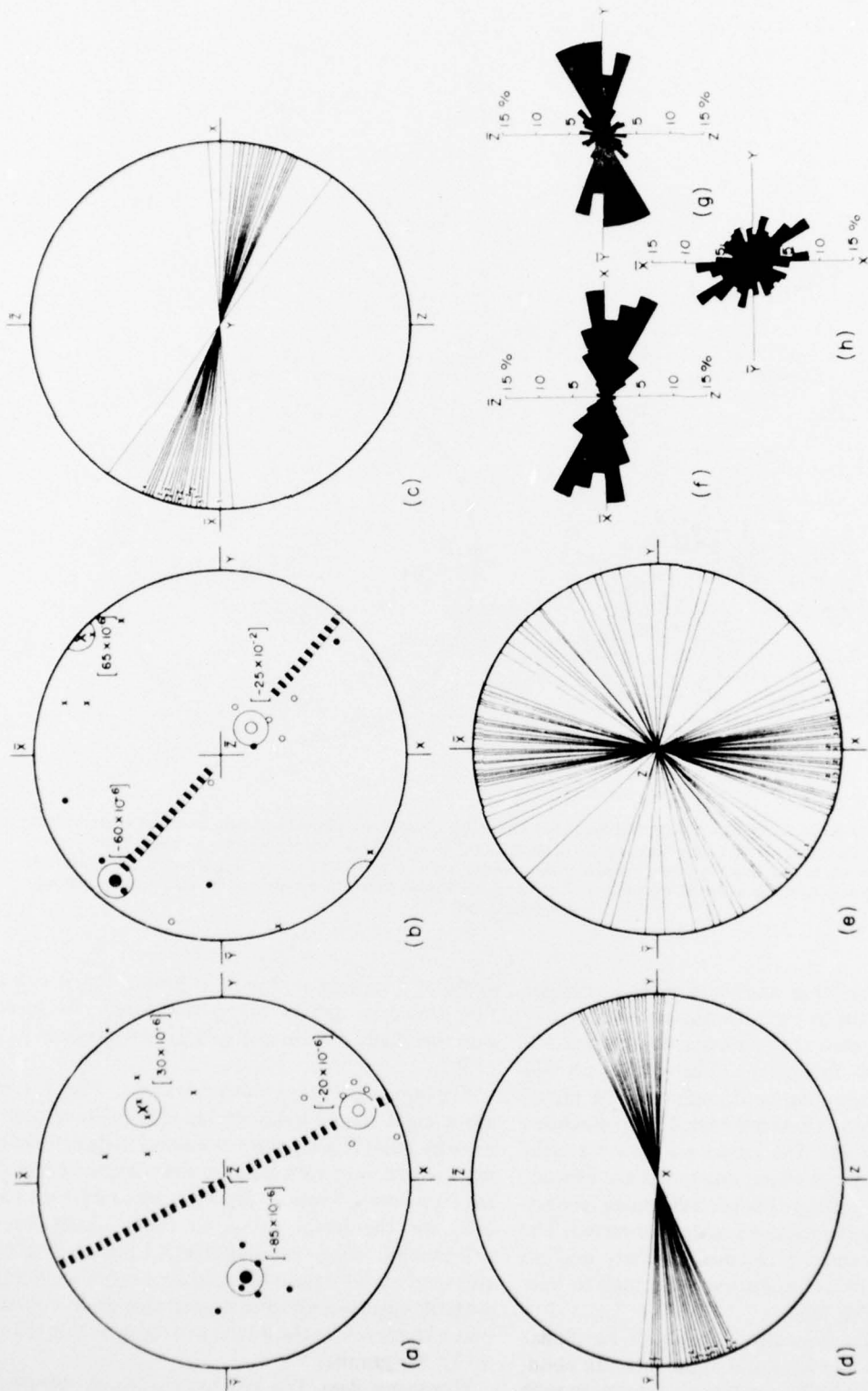


Fig. 6. Residual strain, fracture anisotropy, and fabric data for Berea Sandstone. Diagrams a and b each show orientations and average magnitudes of residual principal strain axes plotted in equal area, lower hemispherical projection. Data in (a) comes from the lower left corner of the XY surface and that in (b) from the center of the XY surface.  $\times$ ,  $\circ$  and  $\bullet$  correspond to the greatest, intermediate, and least elongations, respectively. Dashed lines indicate predicted trends of tensile fractures when discs are point loaded parallel to Z. Diagrams c, d, and e show the orientations of the traces of 36, 40, and 66 tensile fractures induced by point loading parallel to Y, X, and Z, respectively. Diagrams f, g, and h each show the angular distribution of 200 apparent long grain axes.

km sec) 20–30° clockwise from  $X$  (Fig. 3b). The average velocity is much lower than that expected for unfractured quartzite, which suggests the rock contains abundant microfractures. From the velocity pattern one would predict a strong set of microfractures or other planar anisotropy parallel to  $XY$  (i.e. the bedding plane) and perhaps a secondary set of microfractures inclined at 20–30° to the  $XZ$  plane.

The attenuation pattern is almost cubic in symmetry (Fig. 3e). The pattern, in terms of signal amplitude variations, suggests a major set of microfractures or the bedding plane oriented perpendicular to the  $Z$  axis. The pattern also suggests two other sets of microfractures, oriented parallel to the  $YZ$  and  $XZ$  planes. The best signals are transmitted along those directions for which the direction cosines from  $X$ ,  $Y$  and  $Z$  are equal. These directions are equivalent to the corners of a cube whose faces are parallel to the three sets of mutually perpendicular microfractures or some other form of mechanical anisotropy.

#### Berea Sandstone

**Description.** The block of Berea Sandstone measures 29.7 × 29.4 × 21.4 cm, contains no macroscopic fractures, and exhibits thin ( $\approx 1.0$  mm), distinct, bedding laminae parallel to the  $XY$  surface. The rock is a grey, fine-grained sandstone (median grain size about 0.2 mm), with 22 per cent porosity. Its framework grains consist of quartz (70 per cent), polycrystalline quartzose rock fragments (25 per cent), and feldspar (5 per cent). Interstitial areas contain clay and some calcite cement in a ratio of 7:1, respectively. Bedding is manifest by dimensional alignment of detrital grains (Figs. 6f, g), concentrations of fine detritus, and of heavy minerals. The rock is indurated primarily by pressure solution and overgrowths at quartz–quartz grain contacts. These vary from points to sutured, most are tangential. The detrital quartz grains contain some deformation lamellae and healed microfractures, but very few fresh unhealed microfractures are observed in thin section.

**Residual strain.** The residual strains were measured twice. The first set of data is from a 5 cm core taken from the lower left corner of the  $YZ$  surface (Fig. 6a) and the second set is from a 5 cm core taken from the middle of the  $XY$  surface. Similarities and differences between these two solutions are as follows: (1) the principal strain axes from the  $YZ$  core are more tightly grouped than are those from the  $XY$  core suggesting a somewhat higher degree of homogeneity for the former, (2) magnitudes of the average principal strains are in reasonably good agreement in light of the  $\pm 20 \times 10^{-6}$  accuracy of the technique, and (3) their average orientations are not coincident, but they do lie in similar quadrants. The greatest elongations ( $\times$ ) are 35° apart, and the intermediate ( $\circ$ ) and the last elongations ( $\bullet$ ) are each 55° apart.

Although the differences between the two sets of X-ray measurements are significant, the agreement that does exist suggests the residual strains in the block are not totally heterogeneous.

**Fracture anisotropy.** Point loading tests on three mutually perpendicular sets of oriented discs taken from the block indicate a strong tendency for the rock to fracture nearly parallel to bedding ( $XY$  plane), and to a lesser extent, parallel to the  $XZ$  plane (Figs. 6c, d, and e and Table 1). The former is associated with minimum tensile strength (Table 1).

**Fabric.** As for the quartzite, fabric elements that might influence the mechanical and physical properties of the Berea Sandstone were studied in detail. The most conspicuous and influential of these is the sedimentary bedding previously described. Other elements investigated include apparent long grain axes, quartz  $c$ -axes, and intragranular defects—microfractures and quartz deformation lamellae.

The apparent long axes of the detrital grains as seen in thin section reflect not only the orientations of the elongate grains but also the corresponding long grain boundaries and adjacent elongated interstitial areas. The bearings of these long axes for grains with apparent long to short axial ratio of  $\geq 2.0$  are strongly oriented parallel to bedding (Figs. 6f and g). Within the bedding plane they are somewhat oriented along the  $X + 45^\circ$  direction (Fig. 6h). It is significant that the tensile fractures induced by point loading normal to the  $XY$  plane are parallel to the  $XZ$  plane and appear to ignore the trend of the apparent long axis along the  $X + 45^\circ$  direction (Fig. 6c and h).

Crystalllographically the quartz grains are randomly oriented (not illustrated). About 44 per cent of the framework quartz and feldspar grains are undeformed, 41 per cent contain healed microfractures, another 7 per cent exhibit fresh microfractures, 4 per cent contain deformation lamellae, and 5 per cent exhibit twin lamellae. The microfractures and quartz deformation lamellae are randomly oriented (Fig. 5d).

**Transgranular–intergranular fracture.** The tensile fractures induced by point loading propagate intergranularly almost exclusively. This holds for fractures parallel or normal to bedding. Accordingly, the T/I ratio is zero, and factors that influence the fracture anisotropy must also be intergranular.

**Ultrasonic data.** The ultrasonic velocity and attenuation data for the Berea Sandstone exhibit nearly similar symmetry elements (Figs. 3e and f, respectively). The major difference is that the minimum velocity  $< 2.70$  km/sec is inclined at 20–30° to  $Z$  whereas the minimum amplitude signal coincides with  $Z$ . Otherwise the planes of highest and lowest velocity, highest and lowest amplitude, and the  $XZ$  plane are within 20° of being parallel. The intermediate velocity is inclined 10° to  $Y$ , but the overall trend of the relative amplitudes suggests the intermediate attenuation is inclined at 30° to  $Y$ , i.e. 40° to the intermediate velocity.

The minimum velocity and relative amplitude nearly parallel to  $Z$  reflects the mechanical anisotropy of the sedimentary bedding ( $XY$ -plane). The intermediate velocity and relative amplitude, both subparallel to  $Y$ , suggest a second but weaker set of defects oriented nearly parallel to the  $XZ$  plane. The largest velocities and best

signal would be along the intersection of the two sets of defects.

## DISCUSSION OF RESULTS

The residual strains, fracture anisotropy, fabric, and ultrasonic velocity and attenuation in blocks of Charcoal Granite, Sioux Quartzite, and Berea Sandstone have been studied to determine (a) the cause and effect relations among these attributes, and (b) to what degree a knowledge of the residual strains, fabric, or ultrasonic data can be used to predict fracture anisotropy or other aspects of the mechanical behavior of rocks. Toward these ends the data presented in the previous section can be synthesized by focussing attention on the factors that influence fracture anisotropy, and the prediction of that anisotropy.

### Charcoal Granite

Point loading tests indicate a tendency for this rock to fracture at 10° or so the  $XY$  plane (Figs. 1b, c, d; Table 1). Relative to the residual strains, the orientation of tensile fractures induced by point loading can be predicted (e.g. Fig. 1a, dashed line) on the assumptions that (1) the fractures will be controlled solely by the net stress field resulting from superposition of the point load on the state of residual stress (strain), and (2) the fractures will form perpendicular to the net least compressive stress,  $\sigma_3$  and parallel to the net  $\sigma_1\sigma_2$  plane [6]. The point load itself produces an axial compressive stress,  $\sigma_1$ , parallel to the direction of loading and a tensile stress uniform along all radii in the plane normal to the point load. Thus the net  $\sigma_1$  will always parallel the direction of loading and the net  $\sigma_3$  will lie in the plane of each disc parallel to the direction of the residual stress that is least compressive (or most tensile).

For the Charcoal Granite it is clear that the induced tensile fractures are inclined about 10° to the  $XY$  plane if the point load is applied parallel to either the  $X$  or  $Y$  axis. For both these orientations the average greatest residual elongation is nearly perpendicular to the average trend of the fractures (Fig. 1). Thus upon superposing the point load on the residual stresses the net greatest principal tension ( $\sigma_1$ ) coincides with the greatest residual elongation, and the intermediate principal stress will be  $X$  or  $Y$  as the case may be. Moreover, when the point loading is parallel to  $Z$  a nearly random pattern of tensile fractures occur, perhaps because the residual strains (stresses) in the  $XY$  plane are nearly equal.

Clearly the observed state of residual strain is fully compatible with the fracture anisotropy. That is, the trend of the fractures including their slight angle to the  $XY$  plane can be predicted from superposition of the point loads on the observed state of residual strain.

Fabric elements that might also control the fracture anisotropy are any kind of homogeneous, pervasive feature that could serve as a defect or plane of mechanical discontinuity. The measure of an elements' influence on the fracture anisotropy has to be judged on whether or

not its orientation pattern consistently occurs parallel to the trend of the induced fractures.

Consider first the traces of long grain boundaries as observed in three mutually perpendicular thin sections. These are not only potential planar flaws, but they serve to define the orientations of the feldspar crystals which form most of the long boundaries and the load bearing framework of the rock. The trend of the tensile fractures when point loading is parallel to  $Y$  (Fig. 1b) is parallel to the long boundaries in the  $XZ$  plane (Fig. 1f). Similarly the fracture trend for loading parallel to  $X$  (Fig. 1c) is accompanied by a strong orientation of long axes (Fig. 1g).

However, the tensile fractures are statistically random when loading parallel  $Z$ , (Fig. 1d, Table 1). The corresponding long boundaries are scattered although some are clustered at small angles to the  $YZ$  plane. Thus for two of the three loading directions the fractures do follow the traces of the long grain boundaries, and when the grain boundaries are scattered so are the induced tensile fractures. Accordingly, the long grain boundaries cannot be excluded from exercising control on the fracture anisotropy even through the high transgranular-to intergranular ratios suggest that fabric elements internal to the grains rather than grain boundaries are more apt to control fracture orientation in this rock.

*Internal to the grains.* the microfractures and exsolution lamellae are the only types of planar defect that exhibit preferred orientation (Figs. 2b, c, and d). They are strongly oriented parallel to the  $XY$  plane and somewhat less so parallel  $XZ$  and  $YZ$  planes. Accordingly these planar elements also could contribute to the strong fracture anisotropy parallel to  $XY$ .

In summary, the fracture anisotropy in the Charcoal Granite could be caused by one or more of three factors: the residual strains, the oriented framework of feldspar crystals as measured through long grain boundaries, or by intragranular defects.

### Sioux Quartzite

Tensile fractures in this rock form preferentially parallel to the original bedding  $XY$  and nearly parallel to the  $XZ$  and  $YZ$  planes (Figs. 4b, c, and d). Again possible causitive factors are sought in the residual strains, and the rock fabric.

The residual strains and predicted fracture trends are shown in Fig. 4a. Point loading parallel to  $Z$  will result in the net  $\sigma_3$  oriented parallel to the  $X$  axis such that the induced fractures would parallel the  $YZ$  plane (Fig. 4a, dashed line). Point loading parallel to  $X$  would promote tensile fractures parallel to the bedding ( $XY$  plane) because of the strong influence of this plane of mechanical discontinuity. In addition, however, fractures would also parallel the  $XZ$  plane (Fig. 4a, solid line), because for loading parallel to  $X$ , the net  $\sigma_3$  would lie parallel to  $Y$ . Similarly point loading parallel to  $Y$  should result in fractures parallel to the  $YZ$  plane because then the net  $\sigma_3$  would lie parallel to  $X$ . These predictions are correct for each loading direction (Figs. 4b, c, and d). Thus again, the observed state of residual strain as determined from

X-rays is fully in agreement with the fracture anisotropy and could be the controlling factor if it acts as a pervasive prestress.

With regard to the fabric, consider first the apparent long grain axes (equivalent to long grain boundaries). These may be particularly important in controlling the fracture anisotropy in as much as the tensile fractures propagate along grain boundaries 50–30 per cent of their length, i.e.  $T/I$  ratios vary from 1.7 to 2.6. The long grain axes define the bedding plane  $XY$  (Figs. 4e and f) and coincide with the trace of the  $YZ$  plane (Fig. 4g). Indeed tensile fractures do occur along these planes, but the fractures also occur along the  $XZ$  plane when loading is parallel to  $X$  and along the  $YZ$  plane when loading is parallel to  $Y$  (Figs. 4c and d). Corresponding long axes to control these tensile fractures do not occur (Figs. 4e and f). Thus the long axes and associated grain boundaries do not by themselves control the orientation of the tensile fractures.

The orientation patterns of intragranular fabric elements also would seem to eliminate them as exerting controls on the fracture anisotropy. Quartz  $c$ -axes, a partial measure of any crystallographic orientation of the grains in the rock, are randomly oriented (Fig. 5a). Also nearly random are healed microfractures within the quartz (Fig. 5b). Only the quartz deformation lamellae are non-random, these planar elements tend to lie at about 30–40° to the  $XY$  plane (Fig. 5c), but this orientation pattern does not coincide with the orthogonal fracture anisotropy. The quartzite does not contain any other fabric elements that possibly might influence its fracture anisotropy.

In summary, the fracture anisotropy in the Sioux Quartzite is fully consistent with the observed state of residual strain as measured by  $X$ -ray diffractometry. Long grain axes (boundaries) define bedding and one other plane of preferred fracture, but they can not account for the third direction of fracture. Intragranular fabric elements are either randomly or inappropriately oriented to influence the fracture anisotropy.

#### Berea Sandstone

Fracture anisotropy in this rock is strongly controlled by sedimentary bedding (Figs. 6c and d). In addition there is a tendency for the rock to fracture parallel to the  $XZ$  plane when point loaded parallel to  $Z$  (Fig. 6e). Two sets of 30 discs each were point loaded parallel to  $Z$  to double check this fracture trend. The data are essentially identical, and only data from the first set are reported (Fig. 6d, Table 1). Fracture controlled by bedding is commonplace, and further explanation is not needed. The tendency to fracture parallel to  $XZ$  when loaded normal to bedding, i.e. anisotropy of bedding is neutralized, does need to be accounted for.

The residual strains determined by  $X$ -ray diffractometry are not compatible with the fracture anisotropy. The predicted trends for the induced tensile fractures (Figs. 6a, b, dashed lines) do not coincide with the  $XZ$  plane.

With regard to the fabric, the apparent long grain axes adequately define bedding (Figs. 6f and g). Within the bedding plane they trend nearly parallel to the anticipated fracture trends from the  $X$ -ray residual strain data (cf. Figs. 6a, b, and h), but they do not coincide statistically with  $XZ$  plane. Accordingly their influence on this aspect of the fracture anisotropy is doubtful.

Internal to the grains, the  $c$ -axes are random (not illustrated) as are the healed microfractures and quartz deformation lamellae (Fig. 5d). Fresh, unhealed microfractures are rare, and other fabric elements of possible mechanical significance do not occur.

In summary, the fracture anisotropy parallel to bedding in the sandstone was expected. That parallel to the  $XZ$  plane can not be explained by the residual strains or by the fabric elements studied. The results for this rock stand in marked contrast to those for the granite and quartzite for which the residual strain data and some fabric data did agree with the fracture anisotropy.

#### Prediction of the fracture anisotropy

In applied rock mechanics projects such as rapid underground excavation a reliable and practical method is needed for detecting fractures or for predicting mechanical anisotropy of the rock mass. Above it is shown that a knowledge of residual strains and of certain aspects of the fabric could have been used to predict the fracture anisotropy to some degree. However residual strain analyses and fabric work beyond the mapping of macroscopic planes of mechanical discontinuity both require the collection and laboratory analysis of specimens, and as a result neither method is attractive from a pragmatic viewpoint even if the results were totally reliable. Sonic interrogation of the rock mass, on the other hand, is attractive, provided the sonic data can be used to predict the mechanical properties. Hence it is important to evaluate the degree to which the ultrasonic velocity and attenuation data correlate with the information on residual strain and fabric, and in turn, can be used to predict the fracture anisotropy in the three rocks.

Velocity data (Fig. 3a) for the Charcoal Granite suggest microfractures are oriented at small angles to the  $XY$  plane. Moreover, the low mean velocity suggests the microfractures are abundant. These predictions or interpretations are accurate (Figs. 2b, c, and d), although other intragranular planar defects such as cleavages, and exsolution lamellae may also influence the velocities. The velocity field also correlates with the residual strains determined by  $X$ -rays (Fig. 1a). The minimum velocity, parallel to  $Z$ , is within 30° of the average greatest principal elongation. In that velocity increases with increasing normal stress [13], one should expect the maximum and minimum velocities to coincide with the least and greatest elongations, respectively, provided the residual strains (stresses) act like stresses across the boundaries of rocks. Further, the velocities parallel to the  $XY$  plane are nearly equal as are the residual strains parallel to  $X$  and  $Y$  (Fig. 3a). Thus the velocity data are in good agreement with the residual strains and the intragranular defects.

The attenuation (relative amplitude) field for the granite also indicates microfractures are oriented nearly perpendicular to  $Z$  (Fig. 3d). In addition the good signal in the  $Y$  direction and the poor one parallel to  $X$  suggests another somewhat weaker, set of planar mechanical discontinuities parallel to the  $YZ$  plane. There is a small concentration of microfractures parallel to  $YZ$  (Figs. 2b and d) and there is a concentration of tensile fractures developed parallel to  $YZ$  when the discs are loaded parallel to  $Z$ , i.e. when the strong anisotropy parallel to  $XY$  is neutralized (Fig. 1d).

Thus for the granite the ultrasonic velocity and attenuation data correlate exactly with the residual strain and fabric data, and as consequence can be used to accurately predict the major and minor fracture anisotropies.

For the Sioux Quartzite, the velocities define the bedding plane  $XY$  and possibly a secondary plane of mechanical anisotropy inclined 20–30° to the  $XZ$  plane. The comparatively low average velocities suggest that the rock contains abundant microfractures (Fig. 3b). The attenuation data clearly indicate that the  $XY$ ,  $YZ$ , and  $XZ$  are potential planes of mechanical discontinuity (Fig. 3e). These interpretations are correct in the sense that they accurately forecast the three mutually perpendicular planes of fracture anisotropy (Figs. 4b, c, and d). However, the inference that the ultrasonic data are controlled solely by microfractures is inconsistent with the thin section observations which show essentially no fresh microfractures, only randomly oriented healed microfractures, and a preferred orientation of quartz deformation lamellae within 30° of the bedding ( $XY$ ) plane (Figs. 5b and c).

Although the X-ray residual strain data are compatible with the fracture anisotropy it does not agree totally with the ultrasonic data. The symmetry planes of the ultrasonic data, particularly the attenuations, are parallel to those of the observed residual strains (cf. Figs. 3b, e, and 4a); however the average principal least elongation (a compressive strain) coincides with the least velocity and the greatest elongation makes a small angle with the largest compression. These are exactly opposite to the correlations found in the Charcoal Granite and Barre Granite [7].

In summary, the ultrasonic data for the Sioux Quartzite do accurately distinguish the bedding and the two other planes of fracture anisotropy. On the other hand, the velocities and relative amplitudes do not correspond to the residual strain data or to any of the fabric elements studied. This is puzzling because the acoustic properties and the fracture anisotropy must have a cause within the rock. It is possible that very small openings (i.e. flaws) exist along grain boundaries, and influence the acoustic data and fracture anisotropy. This speculation is supported by the low T/I ratios which suggest weakened grain boundaries.

For the Berea Sandstone, the ultrasonic data again accurately define the bedding plane which is the main plane of mechanical anisotropy in the rock (Figs. 3c, f). Likewise the velocity and the attenuation data suggest

the existence of the secondary fracture anisotropy parallel to the  $XZ$  plane. As for the quartzite the microfractures in the sandstone are randomly oriented and the other fabric elements investigated do not seem to be oriented such as to influence the ultrasonic data. Similarly the residual strains are not compatible with the ultrasonic data.

In all three rocks, therefore, the ultrasonic data accurately define all planes of preferential fracture with the attenuation data reflecting some not sensitive to velocity. These predictions are based on the interpretation that microfractures or other partially open discontinuities influence the velocities and relative amplitudes and cause the fracture anisotropy. Thin section observations support this reasoning for the granite, but the study failed to detect a cause in the fabric for all the fracture trends or acoustic properties in the quartzite and sandstone. Minute openings along grain boundaries may dominate the fracture and acoustic properties of these rocks.

This work represents a necessary first step in the development of a rock interrogation system suitable to aid in predicting rock quality for rapid underground excavation projects. The results are encouraging, but they were obtained in dry rock at atmospheric pressure. The acoustical method probably will tend to lose some of its resolving power in rock masses at depth containing fluid filled mechanical discontinuities. It will still be one of the best methods available however, provided the effects of moisture and *in situ* stress are adequately considered.

## CONCLUSIONS

Major conclusions from study of ultrasonic velocity and attenuation, residual strain, fabric, and fracture anisotropy in blocks of Charcoal Granite, Sioux Quartzite, and Berea Sandstone are as follows:

(1) The ultrasonic data accurately define all planes of preferential tensile fracture in all three rocks.

(2) In massive rocks such as the granite, there are good geometric and probably genetic correlations between the ultrasonic data, intragranular planar defects such as microfractures, grain boundaries, the residual strains determined by X-ray diffractometry, and the observed fracture anisotropy.

(3) For the quartzite and sandstone, rocks with strong planar anisotropy (i.e. bedding), the ultrasonic velocities and relative amplitudes can not be explained by the orientations of microfractures determined from thin section studies. The acoustical properties may be controlled by minute flaws along grain boundaries in these rocks. The overriding influence of bedding also probably interferes with the correlation between the ultrasonic and X-ray residual strain data such that only partial correlations exist, at best.

(4) Fracture anisotropy in the quartzite not controlled by bedding is fully consistent with the residual strains measured by X-ray diffraction; however, that in the sandstone is apparently independent of the residual strains.

**Acknowledgements**—The rocks to be studied (Charcoal Granite, Sioux Quartzite, and Berea Sandstone) and the matching ultrasonic data are supplied by the U.S. Bureau of Mines, Twin Cities Mining Research Center. Measurements of residual elastic strains by X-ray diffractometry, the fabric analyses, and the detection of fracture anisotropies through point loading tests were done in the laboratories of the Center for Tectonophysics, College of Geosciences, Texas A & M University. For their help in obtaining these data thanks go to T. L. Blanton III, R. E. Conrad, J. C. Coyne, L. D. Dyke, and J. N. Magourik. This research was supported by the Advanced Research Projects Agency of the Department of Defense and was monitored by the Bureau of Mines, Contract No. H0220062.

Received 22 October 1973

## REFERENCES

- Bur T. R., Thill R. E., and Hjelmstad K. E. An ultrasonic method for determining the elastic symmetry of materials. U.S. Bureau of Mines, R.I. 7333, 23 p. (1969).
- Bur T. R., Hjelmstad K. E., and Thill R. E. An ultrasonic method for determining the attenuation symmetry of materials. U.S. Bureau of Mines, R.I. 7335, 8 p. (1969).
- Willard R. J. and McWilliams J. R. Microstructural techniques in the study of physical properties of rock. *Int. J. Rock Mech. Min. Sci.* **6**, 1-12 (1969).
- Friedman M. Measurement of the state of residual elastic strain in rocks by X-ray diffractometry. *Norelco Reporter* **14**, 7-9 (1967).
- Friedman M. X-ray analysis of residual elastic strains in quartzose rocks. Proc. Tenth Symposium on Rock Mechanics, Austin, Texas, p. 573-595, K. E. Gray, Ed., Soc. Min. Eng. AIME, New York (1972).
- Friedman M. and Logan J. M. The influence of residual elastic strain on the orientation of experimental fractures in three quartzose sandstones. *J. Geophys. Res.* **75**, 387-405 (1970).
- Friedman M. Residual elastic strains in rocks. *Tectonophysics* **15**, 297-330 (1972).
- McClintock F. A. and Argon A. S. *Mechanical Behavior of Materials*. Addison-Wesley, 770 p. (1966).
- Vonicht Barry. Restspannungen im Gestein. *Proc. 1st Congr. Int. Soc. of Rock Mechanics* **2**, 45-50 (1966).
- McWilliams J. R. The role of microstructure in the physical properties of rock. *Testing Techniques for Rock Mechanics*, STP 402, p. 175-189, Amer. Soc. for Testing and Materials, Philadelphia (1966).
- Willard R. J. and McWilliams J. R. Effect of loading rate on transgranular-intergranular fracture in Charcoal Gray Granite. *Int. J. Rock. Mech. Min. Sci.* **6**, 415-421 (1969).
- Borg L., Friedman M., Handin J., and Higgs D. V. Experimental deformation of St. Peter Sand—A study of cataclastic flow. *Rock Deformation*, D. Griggs and J. Handin, Eds., *Geol. Soc. Amer. Mem.* **79**, 133-191 (1960).
- Nur A. and Simmons G. Stress-induced velocity anisotropy in rock: An experimental study. *J. Geophys. Res.* **74**, 6667-6674 (1969).